

Geometric integrators for nonadiabatic molecular quantum dynamics induced by the interaction with the electromagnetic field

THÈSE N° 8145 (2017)

PRÉSENTÉE LE 1ER DÉCEMBRE 2017
À LA FACULTÉ DES SCIENCES DE BASE
LABORATOIRE DE CHIMIE PHYSIQUE THÉORIQUE
PROGRAMME DOCTORAL EN CHIMIE ET GÉNIE CHIMIQUE

ÉCOLE POLYTECHNIQUE FÉDÉRALE DE LAUSANNE

POUR L'OBTENTION DU GRADE DE DOCTEUR ÈS SCIENCES

PAR

Aurélien Kevin Fabrice PATOZ

acceptée sur proposition du jury:

Prof. A. Osterwalder, président du jury
Prof. J. Vanicek, directeur de thèse
Prof. M. Quack, rapporteur
Dr T. Zimmermann, rapporteur
Dr S. Bonella, rapporteuse



ÉCOLE POLYTECHNIQUE
FÉDÉRALE DE LAUSANNE

Suisse
2017

La science cherche le mouvement perpétuel.

Elle l'a trouvé : c'est elle-même.

— *Victor Hugo* —



Acknowledgements

This thesis became a reality with the help and kind support of many people. I would like to express my deep sense of gratitude to all of them.

Foremost, I am grateful to my advisor, Jiří, for all the scientific discussions and the generous guidance, all along the past four years. It was a pleasure working with you, in the LCPT group, and on this very interesting topic.

I am hugely indebted to Miroslav and Sergey for sharing their scientific knowledge and technical know-how.

I would like to express my gratitude to Marius and Marco for the intense discussions during coffee breaks or when we were grabbing beers.

Many thanks and appreciations to Tomáš, Alberto, Eduardo, Konstantin, Tomislav, Choi, and Julien for being excellent colleagues.

A special mention to our secretary Sylvie who dealt with all the tedious administration.

Finally, to my family and friends, thanks for all the good moments we had together.

Lausanne, October 26, 2017

A. P.



Abstract

Understanding the elementary steps involved in a chemical reaction forms the cornerstone of physical chemistry research. One way to deepen this understanding is by studying chemical and physical processes using linear and nonlinear spectroscopic techniques. However, the outcomes of such experiments can be difficult to decipher due to the interweaving of several effects. Therefore, in order to help experimentalists to disentangle such spectra, the role of theorists is to develop efficient tools that are able to accurately describe molecular systems.

The starting point of such tools is solving the time-dependent Schrödinger equation. In this thesis, after implementing geometric integrators, which are based on a combination of the split-operator algorithm and Magnus expansion, for the exact nonadiabatic quantum dynamics of a molecule interacting with a time-dependent electromagnetic field, we derive and implement these geometric integrators for the time-dependent perturbation theory, the Condon, rotating-wave, and ultrashort-pulse approximations, as well as every possible combination thereof. As verified in several model systems, these integrators exactly preserve the geometric invariants, and achieve an arbitrary prescribed order of accuracy in the time step and an exponential convergence in the grid spacing.

We also explore in more detail the ultrashort-pulse approximation and derive an analytical expression for the combination with the time-dependent perturbation theory; this expression significantly accelerates numerical calculations. We show that in the limit of the zero pulse width, the δ -pulse approximation is recovered. We illustrate the performance of the introduced approximations, using a three-dimensional model of pyrazine, in which it is essential to go beyond the δ -pulse limit in order to describe the dynamics correctly.

The high-order algorithms are also applied to the photodissociation dynamics of iodomethane (CH_3I), following its excitation to the A band. We implement a general split-operator with both discrete-variable and finite-basis representations that can treat one non-Cartesian, such as angular coordinate. To test the effect of various degrees of freedom and of the nonadiabatic dynamics, we apply these algorithms to one-, two-, and three-dimensional models of iodomethane, both in the presence and in the absence of nonadiabatic couplings.

Abstract

A full quantum calculation is, however, limited to problems with low dimensionality (approximately ten degrees of freedom). Beyond this, one must seek an affordable balance between computational efficiency and physical accuracy and can employ, for example, semiclassical methods that are based on classical trajectories.

A simple semiclassical approximation that can treat larger systems and requires only local knowledge of the potential is the on-the-fly ab initio thawed Gaussian approximation. We implement a generalization of the method that goes beyond the Franck-Condon approximation and treats Herzberg-Teller active molecules. Our method is used to compute absorption spectra of phenyl radical and of benzene, for which the Herzberg-Teller contribution is essential.

Keywords: time-dependent Schrödinger equation, split-operator, Magnus expansion, time-dependent perturbation theory, Condon approximation, rotating-wave approximation, ultrashort-pulse approximation, δ -pulse approximation, on-the-fly ab initio thawed Gaussian approximation, Herzberg-Teller, pyrazine, iodomethane, phenyl radical, benzene



Résumé

La compréhension des étapes élémentaires impliquées dans une réaction chimique constitue la pierre angulaire de la recherche en chimie-physique. Une façon d'approfondir cette compréhension est d'étudier les processus chimiques et physiques à l'aide de techniques spectroscopiques linéaires et non-linéaires. Cependant, les résultats obtenus peuvent être compliqués à déchiffrer en raison de l'entrelacement de nombreux effets. Par conséquent, le rôle des théoriciens est de développer des outils efficaces afin d'aider les expérimentalistes à démêler leurs résultats.

Le point de départ de ces outils consiste à résoudre l'équation de Schrödinger dépendante du temps. Dans cette thèse, après l'implémentation d'intégrateurs géométriques, qui reposent sur une combinaison de l'algorithme split-operator et de l'expansion de Magnus, pour la dynamique quantique non-adiabatique exacte d'une molécule interagissant avec un champ électromagnétique dépendant du temps, nous dérivons et implémentons ces intégrateurs pour la théorie des perturbations dépendante du temps et les approximations de Condon, de l'onde rotative et des impulsions ultra courtes, ainsi que pour toutes les combinaisons possibles. Comme vérifié dans plusieurs systèmes modèles, ces intégrateurs conservent exactement les invariants géométriques et atteignent un ordre de précision arbitraire par rapport au pas de temps et une convergence exponentielle par rapport à l'espacement de la grille.

Nous explorons également plus en détail l'approximation des impulsions ultra courtes et dérivons une expression analytique pour la combinaison avec la théorie des perturbations, ce qui permet d'accélérer les calculs numériques. Nous montrons que, dans la limite où la longueur de l'impulsion tend vers zéro, l'approximation δ -pulse est retrouvée. La performance de ces approximations est illustrée en utilisant un modèle tridimensionnel de la pyrazine pour lequel il est essentiel d'aller au-delà de la limite δ -pulse.

Les algorithmes sont également appliqués à la dynamique de photodissociation de l'iodométhane (CH_3I) suite à son excitation au niveau de la bande A. Nous implémentons l'algorithme split-operator en utilisant deux représentations : variable discrète et base finie, ce qui permet de traiter une coordonnée non-Cartésienne, telle qu'une coordonnée angulaire.

Résumé

Afin de tester l'effet de différents degrés de liberté et de la dynamique non-adiabatique, nous appliquons ces algorithmes à différents modèles décrivant l'iodométhane.

Un calcul quantique complet est cependant limité à des problèmes de petite taille (tout au plus dix degrés de liberté). Au-delà, il est nécessaire de trouver un compromis entre efficacité computationnelle et précision physique. Par exemple, des méthodes semi-classiques basées sur des trajectoires classiques peuvent être employées.

L'approximation de "thawed Gaussian" ab initio à la volée peut traiter des systèmes plus imposants et nécessite une connaissance uniquement locale du potentiel. Nous implémentons une généralisation de cette méthode qui va au-delà de l'approximation de Franck-Condon et qui traite les molécules Herzberg-Teller actives. Nous l'utilisons pour calculer les spectres d'absorption du radical phényle et du benzène, pour lesquels la contribution Herzberg-Teller est essentielle.

Mots-clés : équation de Schrödinger dépendante du temps, split-operator, expansion de Magnus, théorie des perturbations dépendante du temps, approximation de Condon, approximation des ondes rotatives, approximation des impulsions ultra courtes, approximation δ -pulse, approximation de "thawed Gaussian" ab initio à la volée, Herzberg-Teller, pyrazine, iodométhane, radical phényle, benzène



Contents

Acknowledgements	i
Abstract	iii
Résumé	v
List of Figures	xi
List of Tables	xvii
List of Acronyms	xix
1 Introduction	1
1.1 Overview	1
1.2 Interaction of a Molecule with an Electromagnetic Field	6
1.2.1 Molecular Hamiltonian	6
1.2.2 Interaction with an Electromagnetic Field	8
1.2.3 Exact Solution of the Time-Dependent Schrödinger Equation	9
1.2.4 Description of the Electric Field	10
1.3 Split-Operator Method	10
1.4 Time-Dependent Picture of Linear Spectroscopy	11
1.4.1 Electric-Dipole Spectrum	11
1.4.2 Linear Electric-Dipole Spectrum	12
1.4.3 Linear Electric-Dipole Spectrum and Orientational Averaging	14
2 Approximations for the Molecule-Field Interaction	17
2.1 Basic Approximations	17
2.1.1 Condon Approximation	18
2.1.2 Time-Dependent Perturbation Theory	19
2.1.3 Rotating-Wave Approximation	20
2.1.4 Ultrashort-Pulse Approximation	23
2.2 Combinations of the Basic Approximations	24

2.2.1	Combinations with Condon Approximation	24
2.2.2	Time-Dependent Perturbation Theory and Rotating-Wave Approximation	24
2.2.3	Time-Dependent Perturbation Theory and Ultrashort-Pulse Approximation	25
2.2.4	Rotating-Wave and Ultrashort-Pulse Approximations	26
2.2.5	Time-Dependent Perturbation Theory, Rotating-Wave, and Ultrashort-Pulse Approximations	26
2.3	Numerical Examples	27
2.3.1	A Two-State Harmonic System with Linear Transition-Dipole Couplings	27
2.3.2	A Three-State Harmonic System with Linear Vibronic and Transition-Dipole Couplings	30
2.3.3	A Pump-Probe Experiment in Pyrazine	35
3	Split-Operator and Magnus Integrators of Arbitrary Order	39
3.1	General Definition of Split-Operator Method and Magnus Expansion	39
3.1.1	Split-Operator Method	39
3.1.2	Magnus Expansion	41
3.1.3	Combination of Split-Operator Method with Magnus Expansion	43
3.2	Numerical Implementation of the Exact Propagation	43
3.2.1	Exact Propagation in the Absence of Laser Field	43
3.2.2	Exact Propagation in the Presence of Time-Dependent Laser Field	43
3.3	Numerical Implementation of the Basic Approximations	44
3.3.1	Condon Approximation	44
3.3.2	Time-Dependent Perturbation Theory	44
3.3.3	Rotating-Wave Approximation	45
3.3.4	Ultrashort-Pulse Approximation	45
3.4	Numerical Implementation of the Combinations of the Basic Approximations	45
3.4.1	Combinations with Condon Approximation	46
3.4.2	Time-Dependent Perturbation Theory and Rotating-Wave Approximation	46
3.4.3	Time-Dependent Perturbation Theory and Ultrashort-Pulse Approximation	46
3.4.4	Rotating-Wave and Ultrashort-Pulse Approximations	47
3.4.5	Time-Dependent Perturbation Theory, Rotating-Wave, and Ultrashort-Pulse Approximations	47
3.5	Numerical Tests	47
3.5.1	Verification of the Geometric Properties of the Implemented Integrators	47
3.5.2	Speedup Achieved with the High-Order Geometric Integrators	55
4	Ultrashort- and δ-Pulse Approximations	59
4.1	Theory	59
4.1.1	Analytical Expression for the Combination of Time-Dependent Perturbation Theory and Ultrashort-Pulse Approximation	59

4.1.2	δ -Pulse Approximation	61
4.2	Results and Discussion	61
4.2.1	Comparison Between Analytical and Numerical Results for the Combination of Time-Dependent Perturbation Theory and Ultrashort-Pulse Approximation	62
4.2.2	Population Dynamics	63
4.2.3	Error Analysis	66
5	Photodissociation of Iodomethane Following the Pump-Pulse Excitation to the A Band: Nonadiabatic Quantum Dynamical Study	69
5.1	Theoretical Model	69
5.1.1	Reduced Dimensionality Models	69
5.1.2	Kinetic Energy Operator	70
5.1.3	Potential Energy Surfaces and Initial State	71
5.1.4	Analysis: Radial Distribution Function and Expectation Value	71
5.2	Numerical Implementation	72
5.2.1	Exact Propagation Applied to Iodomethane	72
5.2.2	Numerical Evaluation of the Ground Vibrational State	73
5.3	Results and Discussion	74
5.3.1	Computational Details	74
5.3.2	Population Dynamics	75
5.3.3	Radial Distribution Function of Several Jacobi Coordinates	76
5.3.4	Expectation Value of Several Jacobi Coordinates	76
6	On-the-fly Ab Initio Semiclassical Evaluation of Absorption Spectra of Polyatomic Molecules beyond the Condon Approximation	79
6.1	Theory	80
6.1.1	Generalized Thawed Gaussian Approximation	80
6.1.2	On-the-fly Ab Initio Thawed Gaussian Approximation within Herzberg-Teller Approximation	82
6.1.3	Global Harmonic Approximation	83
6.2	Computational Details	84
6.3	Results and Discussion	84
6.3.1	Absorption Spectrum of Phenyl Radical	85
6.3.2	Absorption Spectrum of Benzene	87
7	Conclusion and Outlook	91
A	Derivation of the Interaction Potential within the Electric-Dipole Approximation	95
B	Systematic Analysis of the Basic Approximations	97
B.1	A Two-State Undisplaced Harmonic System with Linear Transition-Dipole Couplings	97

Contents

B.2	A Two-State Displaced Harmonic System with Linear Transition-Dipole Couplings	100
B.3	A Two-State Displaced Harmonic System with Different Force Constants and Linear Transition-Dipole Couplings	103
B.4	A Three-State Harmonic System with Linear Vibronic and Transition-Dipole Couplings	106
C	Procedure to Determine the CPU Cost and Speedup	109
D	Further Analysis of the Pump-Probe Experiment in Pyrazine	113
D.1	Rigorous Choices of Grid Density, Algorithms, and Time Steps	113
D.2	Error Analysis of Several Propagation Methods	115
E	Convergence of the Second-Order Split-Operator Algorithm	117
F	Further Analysis of the Ultrashort- and δ-Pulse Approximations	119
F.1	Rigorous Choice of Grid Density	119
F.2	Rigorous Choices of the Split-Operator Algorithm and the Nuclear and Electronic Time Steps	120
G	Optimized Geometries and Vibrational Frequencies for Ground and Excited States of Phenyl Radical and Benzene	121
G.1	Phenyl Radical	121
G.2	Benzene	124
	Bibliography	135
	Curriculum Vitae	137

List of Figures

1.1	Meaning of several components of the molecular potential \hat{V}_0 in a one-dimensional two-state harmonic system assuming that $(V_0)_{11}(Q_0) = 0$	8
2.1	Approximations involved in molecular quantum dynamics induced by the interaction with the electromagnetic field. Different approximations are distinguished by different line types: dotted lines = CA, dashed lines = TDPT, double dashed lines = RWA, and solid lines = USP approximation. The exact method is represented in green, approximations in blue, and the most approximate method in red.	18
2.2	Several examples of population dynamics for the four basic approximations (c)-(f) together with the laser pulse shapes (b) applied to a one-dimensional two-state undisplaced harmonic system (a). The left panels show the agreement between approximate and exact quantum calculations. A single parameter has been changed in each of the right panels which causes the breakdown of the corresponding approximation with respect to its exact counterpart. .	29
2.3	Several examples of fidelity of the four basic approximations applied to a one-dimensional two-state undisplaced harmonic model. Same set of parameters as in Fig. 2.2 for left and right panels.	31
2.4	Several examples of population dynamics following the excitation of a one-dimensional three-state displaced harmonic system with different force constants. See Fig. 2.2 for more details.	32
2.5	Several examples of fidelity of the four basic approximations applied to a one-dimensional three-state displaced harmonic system with different force constants. Same set of parameters as in Fig. 2.4 for left and right panels. .	33
2.6	Laser pulse shape and population dynamics obtained with the exact quantum calculation and with several combinations of the basic approximations applied to a one-dimensional three-state displaced harmonic system with different force constants.	34

List of Figures

2.7	Laser pulse shape and population dynamics obtained with the exact quantum calculation and with several level of approximations during the interaction with pump and probe laser pulses applied to a three-dimensional three-state vibronic coupling model of pyrazine.	36
3.1	Laser pulse shape and population dynamics obtained with the exact quantum calculation and with several level of approximations applied to a one-dimensional two-state displaced harmonic system. Time-dependent perturbation theory and its combinations are not able to reproduce the exact calculation.	48
3.2	(a) loglog scale and (b) semilog scale of the convergence with respect to grid density for the exact quantum calculation applied to a one-dimensional two-state displaced harmonic system.	49
3.3	Convergence with respect to grid density for the exact quantum calculation and all possible approximations applied to a one-dimensional two-state displaced harmonic system.	49
3.4	Error of various approximations as a function of the time step Δt using second-, fourth-, sixth-, and eighth-order split-operator algorithms.	50
3.5	Error of various combinations of the basic approximations as a function of the time step Δt using second- and fourth-order split-operator algorithms.	50
3.6	Error of various approximations as a function of the time step Δt using second-order Magnus expansion and fourth- and sixth-order commutator-free Magnus expansions.	52
3.7	Error of the integral in time-dependent perturbation theory as a function of the time step Δt using first-, second-, fourth-, and sixth-order numerical integration schemes.	53
3.8	Error of the integral in the combination of time-dependent perturbation theory and ultrashort-pulse approximation and its combinations with the Condon and rotating-wave approximations as a function of the time step Δt using first-, second-, fourth-, and sixth-order numerical integration schemes.	53
3.9	Verification of the unitarity of several algorithms using a fourth-order split-operator method. (a): an electronic time step is used for the exact quantum calculation and the Condon approximation and a nuclear time step is used for the rotating-wave and ultrashort-pulse approximations, (b): only the electronic time step is used, and (c): only the nuclear time step is used.	54
3.10	Verification of the symplecticity of several algorithms using a fourth-order split-operator method: (a) symplectic methods, (b) non-symplectic ones.	55
3.11	(a) Computational cost and (b) speedup for the exact quantum calculation as a function of the error using second-, fourth- and sixth-order split-operator algorithms. Note that we discarded filled markers to do the linear fit.	56

3.12	(a) Computational cost and (b) speedup for the ultrashort-pulse approximation as a function of the error using second-order Magnus expansion and fourth- and sixth-order commutator-free Magnus expansions. Note that we discarded filled markers to do the linear fit.	56
4.1	Error between the analytical and numerical evaluations of the time-dependent perturbation theory and ultrashort-pulse approximation. (a): without vibronic couplings, (b): with vibronic couplings.	62
4.2	Equivalence of the ultrashort-pulse approximation and the combination of the time-dependent perturbation theory and ultrashort-pulse approximation. (a): without vibronic couplings and (b): with vibronic couplings.	63
4.3	Laser pulse shapes (a) and population dynamics obtained with the exact quantum calculation and with several level of approximations during the vertical photoexcitation with ultrashort laser pulses without vibronic couplings (b) and with vibronic couplings (c).	64
4.4	Population dynamics on the second excited state obtained with the exact quantum calculation and with several level of approximations after the vertical photoexcitation with ultrashort laser pulses without vibronic couplings (a) and with vibronic couplings (b).	65
4.5	Errors of various ultrashort-pulse approximations as a function of time. (a): without vibronic couplings, (b): with vibronic couplings.	67
4.6	Errors of various ultrashort-pulse approximations as a function of the pulse length. (a): without vibronic couplings, (b): with vibronic couplings.	67
5.1	Jacobi coordinates used in the three-dimensional model of iodomethane. . .	70
5.2	Populations dynamics of iodomethane following the excitation by a pump pulse for the one-, two-, and three-dimensional systems with and without nonadiabatic couplings.	75
5.3	Radial distribution of (a) the dissociative bond length R and (b) the stretching r coordinates at several times of the dynamics for the three-dimensional system in presence of nonadiabatic couplings.	77
5.4	(a) Dissociative bond length R , (b) stretching coordinate r , and (c) Jacobi angle θ in the ground (1A_1) and two excited ($^3Q_{0+}$ and 1Q_1) states as a function of time for the one-, two-, and three-dimensional systems with and without nonadiabatic couplings.	78
6.1	Comparison between the experimental, Franck-Condon (FC), and Franck-Condon Herzberg-Teller (FCHT) spectra calculated by (a) on-the-fly ab initio thawed Gaussian approximation (OTF-AI-TGA), (b) adiabatic harmonic (AH) approximation, and (c) vertical harmonic (VH) approximation.	86
6.2	Comparison between the experimental, “Franck-Condon” (“FC”), and Franck-Condon Herzberg-Teller (FCHT) spectra calculated by (a) on-the-fly ab initio thawed Gaussian approximation (OTF-AI-TGA), (b) adiabatic harmonic (AH) approximation, and (c) vertical harmonic (VH) approximation.	89

List of Figures

6.3	Time-dependence of the frequency of the mode ν_{20} in the excited electronic state for the on-the-fly ab initio thawed Gaussian approximation (OTF-AI-TGA), and the adiabatic (AH) and vertical (VH) global harmonic approximations.	89
6.4	Comparison between the experimental, Franck-Condon (FC), and Franck-Condon Herzberg-Teller (FCHT) spectra calculated by (a) on-the-fly ab initio thawed Gaussian approximation (OTF-AI-TGA), (b) adiabatic harmonic (AH) approximation, and (c) vertical harmonic (VH) approximation.	90
B.1	Convergence with respect to grid density for the exact quantum calculation applied to a one-dimensional two-state undisplaced harmonic system.	97
B.2	Several examples of population dynamics for the four basic approximations (c)-(f) together with the laser pulse shapes (b) applied to a one-dimensional two-state undisplaced harmonic system (a). All the right panels have the same exact result and show the discrepancy between approximate and exact quantum calculations. A single parameter has been changed in each of the left panels which causes the agreement of the corresponding approximation with respect to its exact counterpart.	99
B.3	Convergence with respect to grid density for the exact quantum calculation applied to a one-dimensional two-state displaced harmonic system.	100
B.4	Several examples of population dynamics for the four basic approximations (c)-(f) together with the laser pulse shapes (b) applied to a one-dimensional two-state displaced harmonic system (a). The left panels show the agreement between approximate and exact quantum calculations. A single parameter has been changed in each of the right panels which causes the breakdown of the corresponding approximation with respect to its exact counterpart.	101
B.5	Several examples of population dynamics following the excitation of a one-dimensional two-state displaced harmonic system for the case where all the basic approximations break down. See Fig. B.2 for more details.	102
B.6	Convergence with respect to grid density for the exact quantum calculation applied to a one-dimensional two-state displaced harmonic system with different force constants.	103
B.7	Several examples of population dynamics following the excitation of a one-dimensional two-state displaced harmonic system with different force constants for the case where all the basic approximations work. See Fig. B.4 for more details.	104
B.8	Several examples of population dynamics following the excitation of a one-dimensional two-state displaced harmonic system with different force constants for the case where all the basic approximations break down. See Fig. B.2 for more details.	105
B.9	Convergence with respect to grid density for the exact quantum calculation applied to a one-dimensional three-state displaced harmonic system with different force constants.	106

B.10	Several examples of population dynamics following the excitation of a one-dimensional three-state displaced harmonic system with different force constants for the case where all the basic approximations break down. See Fig. B.2 for more details.	108
C.1	Error of various approximations compared to the fully converged exact quantum calculation as a function of the time step Δt using a fourth-order split-operator algorithm.	109
C.2	Error of various approximations as a function of the time step Δt using a fourth-order split-operator algorithm.	110
C.3	Error of various approximations as a function of the time step Δt using either a sixth-order commutator-free Magnus expansion algorithm or a sixth-order numerical integration scheme.	110
D.1	Convergence with respect to grid density for the exact quantum calculation applied to a three-dimensional three-state vibronic coupling model of pyrazine.	113
D.2	Error of various approximations as a function of the time step Δt using second- and fourth-order split-operator algorithms.	114
D.3	Error of various approximations as a function of the time step Δt using second-order Magnus expansion and fourth- and sixth-order commutator-free Magnus expansions.	115
D.4	Error of various approximations compared to (a) the exact quantum calculation and (b) the ultrashort-pulse approximation as a function of time.	116
E.1	Error of the exact quantum calculation as a function of the time step Δt using a second-order split-operator method and different time-evaluation of the time-dependent interaction potential.	117
F.1	Convergence with respect to grid density for the exact quantum calculation applied to a three-dimensional three-state vibronic coupling model of pyrazine without vibronic couplings (a) and with vibronic couplings (b).	119
F.2	Error of various approximations as a function of the time step Δt using first-, second-, and fourth-order split-operator algorithms.	120

List of Tables

2.1	Abbreviations of the basic approximations used in the formulas.	18
2.2	Dimensionless parameters in natural units.	27
2.3	Dimensionless parameters (in natural units) for the one-dimensional two-state undisplaced harmonic system such that each basic approximation either works or breaks down.	28
2.4	Dimensionless parameters (in natural units) for the one-dimensional three-state displaced harmonic system with different force constants such that each basic approximation either works or breaks down.	31
2.5	CPU time and speedup with respect to the exact propagation for several approximate methods averaged over 10 simulations using a single core of a Six-Core AMD Opteron 2427 processor chip. Δt_{ME} and Δt_{NI} refer to the time step needed to perform Magnus expansion and numerical integration, respectively.	35
2.6	Pump and probe laser pulse parameters in atomic units.	36
2.7	CPU time and speedup with respect to the exact propagation for several approximate methods using a single core of a Six-Core AMD Opteron 2427 processor chip.	37
5.1	Coordinate grids used to compute the ground vibrational state for one-, two-, and three-dimensional systems, together with computed zero point energies (ZPEs).	74
5.2	Time and grid parameters used to perform the exact quantum dynamics of the one-, two-, and three-dimensional systems.	75
5.3	Parameters of the laser pulse.	75
B.1	Dimensionless parameters (in natural units) for the one-dimensional two-state undisplaced harmonic system such that each of the basic approximations either breaks down or works.	98
B.2	Dimensionless parameters (in natural units) for the one-dimensional two-state displaced harmonic system such that each of the basic approximations either works or breaks down.	100

List of Tables

B.3	Dimensionless parameters (in natural units) for the one-dimensional two-state displaced harmonic system such that each of the basic approximations either breaks down or works.	103
B.4	Dimensionless parameters (in natural units) for the one-dimensional two-state displaced harmonic system with different force constants such that each of the basic approximations either works or breaks down.	106
B.5	Dimensionless parameters (in natural units) for the one-dimensional two-state displaced harmonic system with different force constants such that each of the basic approximations either breaks down or works.	106
B.6	Dimensionless parameters (in natural units) for the one-dimensional three-state displaced harmonic system with different force constants such that each of the basic approximations either breaks down or work.	107
C.1	Requested and achieved errors for several approximate methods.	111
G.1	Optimized cartesian geometries (in Å) of ground \tilde{X}^2A_1 and excited \tilde{A}^2B_1 states of phenyl radical.	122
G.2	Symmetry of phenyl radical normal modes together with the corresponding ground \tilde{X}^2A_1 and first excited \tilde{A}^2B_1 states frequencies in cm^{-1} [using adiabatic harmonic (AH) and vertical harmonic (VH) models], displacements δ in a.u., and dimensionless relative displacements $\Delta = A_0^{1/2} \cdot \delta$	123
G.3	Optimized bond lengths (in Å) of ground 1^1A_{1g} and excited 1^1B_{2u} states of benzene.	124
G.4	Symmetry of benzene normal modes together with the corresponding ground 1^1A_{1g} and first excited 1^1B_{2u} states frequencies in cm^{-1} [using adiabatic harmonic (AH) and vertical harmonic (VH) models], displacements δ in a.u., and dimensionless relative displacements Δ	125



List of Acronyms

AH	adiabatic harmonic
AI	ab initio
a.u.	atomic units
CA	Condon approximation
CFME	commutator-free Magnus expansion
CSO	concatenated split-operator
CSO/ME	concatenated split-operator Magnus expansion
ESO	elementary split-operator
FC	Franck-Condon
FCHT	Franck-Condon Herzberg-Teller
FWHM	full-width at half-maximum
HT	Herzberg-Teller
ME	Magnus expansion
n.u.	natural units
OTF	on-the-fly
OTF-AI-TGA	on-the-fly ab initio thawed Gaussian approximation
RWA	rotating-wave approximation
SO	split-operator
SO/ME	split-operator/Magnus expansion
TGA	thawed Gaussian approximation
TDPT	time-dependent perturbation theory
USP	ultrashort pulse
VH	vertical harmonic

1 Introduction

1.1 Overview

In the context of nonadiabatic molecular quantum dynamics, solving the time-dependent Schrödinger equation enables us to predict the motion of nuclei on electronic potential energy surfaces. To describe many photochemical and photobiological processes, several potential energy surfaces are often needed and are frequently coupled to each other, which means that nuclei can jump from one surface to another [1]. This is called the nonadiabatic effect [2, 3] and is one of the main processes in physical, chemical, and biological reactions [4, 5].

Such processes cover a wide range of time scales and with the advent of femtosecond laser technology, the study has moved towards the kinetics of the fastest molecular processes. For an illustration of the “femtochemistry field” [6] that enables real-time spectroscopy on a femtosecond time scale, it is worth citing the pioneer work by Zewail [7, 8]. His pump-probe experiment is the benchmark in light-matter interaction studies: First, a short pump laser pulse excites coherently a sample of molecules. Then, after a certain time delay, a probe pulse hits the sample. By monitoring the probe signal as a function of the time delay, information on the time evolution of the system can be obtained. Variants of this pump-probe technique enable us to follow, in real time, molecular rearrangements [9–11] and many other processes, such as photodissociation dynamics of diatomic molecules in the gas phase [12] or excited state dynamics of dye molecules in solution [13].

Theoretical models help experimentalists to disentangle such dynamical processes. For example, theories for femtosecond pump-probe experiments on solvated polyatomic molecules [14] and for large polyatomic molecules in condensed phases [15] have been developed, as well as for femtosecond time-resolved ionization spectroscopy of ultrafast internal conversion dynamics in polyatomic molecules [16]. Another example is the development of a density matrix theory that enables to obtain third-order time- and frequency-resolved optical signals such as the four-wave-mixing, n-wave-mixing, and photon-echo signals [17–19]. Recent theoretical developments [20] suggest a new time-domain spectroscopic technique based on strong pump and probe pulses. It enables the real-time investigation of molecular

processes that cannot be resolved temporally by the usual weak pump and probe pulses.

For low-dimensional systems, the starting point of these theories is solving the time-dependent Schrödinger equation, which is the most accurate and straightforward approach. In principle, the description of the interaction of the system with electromagnetic field requires the application of quantum field theory. However, in most situations, it has been shown that it is sufficient to use classical electromagnetism to describe the light-matter interaction as a classical field interacting with quantum matter [21]. Under given assumptions, the expressions for certain observables will be the same as if derived using quantum field theory. For all cases discussed in this thesis, a classical description of the field, together with a quantum treatment of matter is considered sufficiently accurate.

However, applying numerical algorithms that treat exactly the interaction between quantum matter and a classical electromagnetic field can be still time consuming. Therefore, it is worth using approximations to accelerate calculations.

The δ -function pulse, or “infinitely short” pulse approximation seems natural for the description of time-resolved spectroscopy [15, 22–29]. However, such pulses are not experimentally feasible [30]. Furthermore, they are not desired because they would simultaneously excite all dipole-allowed electronic states of the system. As a result, it is useful to consider the impulsive limit [31] that defines a new kind of pulse known also as an ultrashort pulse; the duration of the pulse is longer than electronic time scale and shorter than nuclear one [24, 25]. However, for the specific diabatically coupled systems studied in Refs. [24, 25], it is shown that such pulses are not sufficiently short to guarantee the validity of the impulsive limit [28, 31]. Therefore, besides the fact that the pulse must be shorter than the time scale of vibrational dynamics, it should also be short compared to the time scale on which the nonadiabatic dynamics occurs.

Another common approximation is the so-called rotating-wave approximation [32, 33], quite often used in the fields of quantum optics and magnetic resonance. It was developed in order to obtain an analytical solution of a quantum mechanical two-level system driven by a constant sinusoidal external potential. Indeed, if the laser field is nearly resonant with the electronic transition and if the field intensity is “low” (the latter condition being less stringent than the former, as will be shown later), it is possible to neglect highly oscillatory terms in the interaction potential of the Hamiltonian [34, 35]. Indeed, these terms will average to zero in a reasonable time scale. In systems with more than two levels, a generalization of the rotating-wave approximation is also called the quasi-resonant condition [36–40].

Another very useful approximation is the Condon approximation [41–44]. It assumes that the time scale of an electronic transition is short, compared to nuclear motion. Therefore, the transition probability can be calculated at a fixed nuclear position. In other words, the transition dipole moment is considered to be independent of the coordinates of the nuclei.

In the case when interaction between a molecular system and electromagnetic field is

weak, i.e., the molecular properties are not significantly altered by the field, the interaction potential can be considered as a perturbation. The solution of the time-dependent Schrödinger equation can be obtained using the first-order time-dependent perturbation theory [24, 45, 46].

The above-mentioned ultrashort-pulse, rotating-wave, and Condon approximations, together with the time-dependent perturbation theory, are four of the most common approximations for treating the light-matter interaction. It is not uncommon for one, or even a combination of these approximations, to be employed without previous knowledge of its validity. In order to avoid such problems, in this thesis, the validity of these four basic approximations and their combinations is predicted by defining corresponding dimensionless parameters.

The main goal of this thesis is to study these approximations for the molecule-field interaction by using geometric integrators of arbitrary order of accuracy in the time step. To do so, the time-dependent Schrödinger equation has to be converted, independently of the number of approximations included, into a numerically tractable problem by the discretization of time and space [47, 48]. This, in general, is done in two steps: First, the wavefunction and corresponding operators are either represented by an expansion in a set of basis functions or discretized on a spatial grid; second, a numerical algorithm is used to propagate the initial wavefunction in time.

Many numerical propagation schemes have been developed and the summary of various approaches can be found in specialized reviews [47–53]. Most of the algorithms were originally designed to solve the time-dependent Schrödinger equation with time-independent Hamiltonian and some of them were extended to treat systems where the potential depends explicitly on time.

Amongst these algorithms, the Chebyshev propagator [54] is based on an expansion of the time-evolution operator in terms of complex Chebyshev polynomials and enables the use of a large time step [55, 56]. There is also the second-order differencing scheme [57–59] that expands the evolution operator in a Taylor series. Runge Kutta schemes [60, 61] are also widespread due to their variable time step that eliminates the need to determine the time step by a trial-and-error procedure. All these methods obviously have their advantages and disadvantages, and their performance depends on the particular problem under study. In this thesis, we focus on geometric integrators. They are defined as a numerical integration of a differential equation that preserves geometric properties of the quantum dynamics such as time-reversal symmetry, unitarity, and symplectic structure [62, 63]. The general split-operator/Magnus integrator algorithm is such an integrator and is therefore the one we use, together with a grid representation of the wavefunction and operators. The split-operator method exploits the ease of treating operators in their diagonal representations. While it was originally based on a symmetric second-order factorization of the time-evolution operator [64, 65], it was later generalized to an arbitrary order of accuracy [66–70]. The Magnus integrator, in turns, invokes the fact that the evolution operator for a time-dependent Hamiltonian can also be written as a Magnus

expansion [71–77]. Symplectic numerical algorithms are, as of this writing, still considered an important area of research. For example, a fourth-order gradient symplectic integrator has been proposed for solving the time-dependent Schrödinger equation [70, 78] and proves to accelerate the quantum calculation, while symplectic algorithms for nonseparable Hamiltonians have been developed for solving the dynamics of charged particles in a magnetic field [79, 80].

Implementing symplectic algorithms is usually straightforward when dealing with Cartesian coordinates. On one hand, when studying a more realistic example such as polyatomic photodissociation dynamics, internal coordinates are often more appropriate as they enable to lower the dimensionality. On the other hand, they result in a more involved kinetic energy term. Another focus in this thesis, motivated by the experiments in H.-J. Wörner’s group at ETH Zürich, is the study of the effects of various degrees of freedom and of the nonadiabatic couplings on the photodissociation of iodomethane induced by a femtosecond pump pulse.

Photodissociation dynamics of iodomethane following the excitation to the A band has been studied since the discovery of the first laser that relies on photodissociation [81]. More recently, Wörner and coworkers explored it with time-resolved high-harmonic spectroscopy [82]. These methods were originally applied only to the electronic ground state of molecules [83, 84], yet, ultrafast dynamics occurs predominantly in excited electronic states, hence Wörner et al. extended the methodology to excited states [82, 85–89]. In these experiments, first, two synchronized pump pulses are used to generate an intensity grating that induces a spatial modulation of the excited state’s population. Then, using an intense femtosecond probe pulse, an electron wave packet can be extracted from one of the valence orbitals and driven back to interfere with the remaining bound electronic state. If the electron recombines, extreme ultraviolet radiation is emitted. This phenomenon, known as high-harmonic generation, makes it possible to create an image of a molecular orbital [90], probe vibrational dynamics [91, 92], or observe a chemical reaction in real time [93].

The observed high-harmonic signal in the iodomethane experiment depends crucially on population dynamics. To understand it better, we perform exact nonadiabatic quantum dynamics simulations of the photodissociation process induced by the pump pulse. To support high-harmonic generation experiments performed in H.-J. Wörner’s group, we modify the methodology to non-Cartesian coordinates. In order to treat one problematic angular coordinate, we implement, in particular, a general split-operator with both discrete-variable and finite-basis representations.

However, neither the high-order split-operator/Magnus integrator algorithms, nor any of the physical approximations, can overcome the exponential scaling of the computational cost with dimensionality, i.e., full quantum calculations are limited to approximately ten degrees of freedom. Indeed, the nonadiabatic dynamics is inherently quantum mechanical, and sensitive to the amount of quantum mechanics involved to treat the problem, which inhibits the application to large systems. However, for typical molecular problems, the

promising development of the multi-configuration time-dependent Hartree method [94, 95] enables to deal with up to about 30 degrees of freedom quantum mechanically. Other examples allowing to treat larger systems are the methods employing Gaussian bases, such as the Gaussian multi-configuration time-dependent Hartree method [96, 97], multiple spawning [98, 99], and ab initio multiple spawning [100], for which the incompleteness of the basis is, in principle, the only contribution to the inexactness of the result. Beyond this limit, an affordable balance between computational efficiency and physical accuracy is required. For example, an attempt to treat large systems has been proposed using only few specific quantum modes and a classical “bath” [101, 102]. Alternatively, semiclassical methods based on classical trajectories can be used. For these methods, an ensemble of classical trajectories, accompanied by a complex phase factor, is employed and enables them to capture interference effects. Therefore, various quantum effects can be described in contrast to standard classical molecular dynamics. But, in these semiclassical methods, the number of classical trajectories required for convergence usually grows rapidly with dimensionality, hence they are also limited to rather small molecular systems, i.e., few atoms.

To go beyond this and still partially include some quantum effects, more severe semiclassical approximations can be invoked, such as the phase averaging/dephasing representation [103–110], a highly efficient multi-trajectory semiclassical method, or the thawed Gaussian approximation [111–113], a single trajectory based method. The convergence of the former is independent of the dimensionality, however, the accuracy depends strongly on the system under study. As for the latter, it is suited only for short-time dynamics but, due to the ultrafast character of the dynamics, this is of less importance. Moreover, the implementation of the thawed Gaussian approximation is also performed using geometric integrators. Indeed, the norm is preserved exactly and the numerical integration of classical equations of motion is carried out using a symplectic algorithm. In addition, it goes beyond the global harmonic approximation and captures, at least partially, the anharmonicity of the studied system.

The key ingredient, for each method, is the definition of the potential energy surfaces. Traditionally they are computed beforehand, which leads to the bottleneck of exact quantum dynamics for large systems. However, trajectory-based methods require only local knowledge of the potential. Therefore, potential energy surfaces can be computed on the fly (i.e., only where needed) by using ab initio electronic structure packages, which avoids exponential scaling with dimensions.

The calculations of Franck-Condon absorption or emission spectra of large and/or floppy molecules [114, 115] have proven to be successful within the on-the-fly ab initio thawed Gaussian approximation. In classical mechanics, this means that an electronic transition is most likely to occur without changes in the positions of the nuclei in the molecular entity; in other words, the transition dipole moment is independent of nuclear coordinates, which leads to a vertical transition. In quantum mechanics, the intensity of a vibronic transition is proportional to the square of the overlap integral between the vibrational

wavefunctions that belong to the two different electronic states involved in the transition. However, it is possible that for the system under study, the absorption of a photon is electronically forbidden but vibronically allowed. Therefore, it is necessary to go beyond the Franck-Condon approximation. In the last part of this thesis, we focus on the computation of absorption cross sections within the Herzberg-Teller approximation, which goes beyond the Condon approximation by allowing a linear dependence of the transition dipole moment on nuclear coordinates. To do so, we implement a generalization of the on-the-fly ab initio thawed Gaussian approximation and test it by calculating the $\tilde{A}^2B_1 \leftarrow \tilde{X}^2A_1$ absorption spectrum of phenyl radical and $1^1B_{2u} \leftarrow 1^1A_{1g}$ absorption spectrum of benzene, for which the Franck-Condon approximation fails completely. The new approach improves older absorption cross sections computed within the Franck-Condon approximation and also gives much better results than those obtained via global harmonic approximations.

The remainder of this thesis is organized as follows: the theoretical background needed to understand the full manuscript is presented in Chapter 1. In Chapter 2, we define and derive the approximations to the interaction with the electromagnetic field and present numerical examples that show how several approximations can work and break down. The symplectic numerical algorithms for the exact and approximate propagation schemes are presented in Chapter 3. In addition, we demonstrate, on several examples, the conservation of geometric properties. Chapter 4 focuses on the ultrashort-pulse approximation and its relation to the well-known δ -pulse approximation. We show the necessity to go beyond the δ -pulse limit in the case of the three-dimensional three-state vibronic coupling model of pyrazine. Next, in Chapter 5, we study the effects of various degrees of freedom and of the nonadiabatic couplings on the photodissociation of iodomethane induced by a femtosecond pump-pulse. Then, in Chapter 6, we show how the on-the-fly ab initio thawed Gaussian approximation can be used in order to compute absorption cross sections beyond the Franck-Condon approximation for higher-dimensional systems such as phenyl radical and benzene. Finally, Chapter 7 summarizes the main results and concludes this thesis.

1.2 Interaction of a Molecule with an Electromagnetic Field

1.2.1 Molecular Hamiltonian

Considering only S lowest-lying electronic states, we write a general time-dependent state of a molecule as the superposition

$$|\psi(t)\rangle = \sum_{n=1}^S |\psi_n(t)\rangle |n\rangle = \begin{pmatrix} |\psi_1(t)\rangle \\ \vdots \\ |\psi_S(t)\rangle \end{pmatrix}, \quad (1.1)$$

where $|\psi_n(t)\rangle$ is a time-dependent nuclear wavepacket on the n th potential energy surface, and $|n\rangle$ is the corresponding time-independent—typically adiabatic or diabatic—electronic state. In the absence of electromagnetic field, evolution of $|\psi(t)\rangle$ is given by the time-

dependent Schrödinger equation

$$i\hbar \frac{d}{dt} |\psi(t)\rangle = \hat{\mathbf{H}}_0 |\psi(t)\rangle, \quad (1.2)$$

with the time-independent molecular Hamiltonian

$$\hat{\mathbf{H}}_0 := \hat{\mathbf{T}} + \hat{\mathbf{V}}_0. \quad (1.3)$$

Throughout this thesis, the **bold** face denotes electronic operators, i.e., S -dimensional vectors and $S \times S$ matrices acting on the Hilbert space \mathbb{C}^S spanned by S discrete electronic states, and the hat $\hat{\cdot}$ denotes nuclear operators acting on the Hilbert space $\mathcal{L}^2(\mathbb{R}^D)$ of square integrable functions of D continuous nuclear degrees of freedom.

The first component of the molecular Hamiltonian (1.3) is the nuclear kinetic energy operator

$$\hat{\mathbf{T}} := \hat{T} \mathbf{1}, \quad (1.4)$$

$$\hat{T} := \frac{1}{2} \hat{P}^T \cdot M^{-1} \cdot \hat{P}, \quad (1.5)$$

where $M = \text{diag}(M_1, M_2, \dots, M_D)$ denotes the diagonal nuclear mass matrix and \cdot denotes the matrix product in the nuclear configuration space \mathbb{R}^D . The second component of $\hat{\mathbf{H}}_0$ is the molecular potential energy operator

$$\hat{\mathbf{V}}_0 \equiv \hat{\mathbf{V}}_e + \hat{\mathbf{V}}_n + \hat{\mathbf{V}}_{\text{ne}}, \quad (1.6)$$

consisting of the electronic part

$$\hat{\mathbf{V}}_e := \hat{\mathbf{V}}_e, \quad (1.7)$$

$$\mathbf{V}_e := \mathbf{V}_e(Q_0),$$

nuclear part

$$\hat{\mathbf{V}}_n := \hat{V}_n \mathbf{1}, \quad (1.8)$$

$$\hat{V}_n := (\hat{V}_0)_{11} - (V_0)_{11}(Q_0),$$

and the vibronic coupling $\hat{\mathbf{V}}_{\text{ne}}$. Above, Q_0 denotes the coordinates of a reference nuclear configuration, which typically corresponds either to the minimum of the ground potential energy surface $(V_0)_{11}$ (this is what we use) or to a conical intersection. From here on, we will use the convention that the potential energy is zero at the reference configuration Q_0 on the ground electronic potential energy surface, i.e.,

$$(V_0)_{11}(Q_0) = 0 \quad (\text{convention}).$$

As we assume that the electronic basis is diabatic, the electronic potential energy \mathbf{V}_e is a

Introduction

diagonal¹ $S \times S$ matrix and $\hat{\mathbf{V}}_0$ is independent of nuclear momenta but contains offdiagonal elements—the so-called diabatic electronic couplings. Note that the vibronic coupling $\hat{\mathbf{V}}_{\text{ne}}$ contains not only the offdiagonal elements (which, in diabatic basis, must be at least of linear order in Q , and are sometimes defined to be *the* vibronic coupling) but also diagonal elements if the nuclear dependence of the diabatic potential energy surfaces is different for different surfaces, e.g., due to displacement of the minima of the different potential energy surfaces. A simple two-state one-dimensional harmonic system represented in Fig. 1.1 should clarify some of the previous definitions.

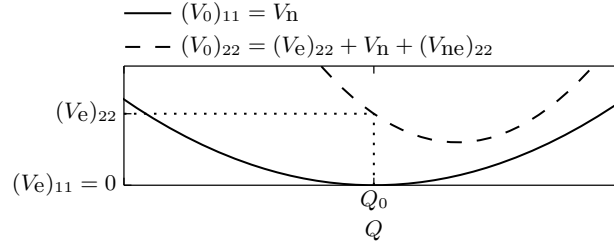


Figure 1.1 – Meaning of several components of the molecular potential $\hat{\mathbf{V}}_0$ in a one-dimensional two-state harmonic system assuming that $(V_0)_{11}(Q_0) = 0$.

Finally, note that it is sometimes useful to separate the molecular Hamiltonian differently, as $\hat{\mathbf{H}}_0 \equiv \hat{\mathbf{H}}_{\text{n+ne}} + \hat{\mathbf{V}}_{\text{e}}$, where

$$\hat{\mathbf{H}}_{\text{n+ne}} := \hat{T}\mathbf{1} + \hat{\mathbf{V}}_{\text{n+ne}} \quad (1.9)$$

denotes the Hamiltonian of nuclei together with the vibronic coupling, and

$$\hat{\mathbf{V}}_{\text{n+ne}} := \hat{V}_{\text{n}}\mathbf{1} + \hat{\mathbf{V}}_{\text{ne}} \quad (1.10)$$

contains the nuclear $\hat{V}_{\text{n}}\mathbf{1}$ and vibronic $\hat{\mathbf{V}}_{\text{ne}}$ parts of the molecular potential.

1.2.2 Interaction with an Electromagnetic Field

The interaction of the molecule with a time-dependent laser field is described by a time-dependent Schrödinger equation

$$i\hbar \frac{d}{dt} |\psi(t)\rangle = \hat{\mathbf{H}}(t) |\psi(t)\rangle \quad (1.11)$$

with the Hamiltonian

$$\hat{\mathbf{H}}(t) := \hat{\mathbf{H}}_0 + \hat{\mathbf{V}}_{\text{int}}(t) = \hat{\mathbf{T}} + \hat{\mathbf{V}}(t) \quad (1.12)$$

consisting of the molecular Hamiltonian $\hat{\mathbf{H}}_0$ and the time-dependent interaction potential $\hat{\mathbf{V}}_{\text{int}}(t)$. Within the long-wavelength and electric dipole approximations [116], the

¹Definition (1.7) suggests that \mathbf{V}_{e} could contain offdiagonal elements. However, the orthogonal transformation that diagonalizes \mathbf{V}_{e} does not depend on nuclear coordinates, and therefore will not introduce nonadiabatic momentum couplings if applied to the matrix $\hat{\mathbf{V}}_0$. Therefore there is a single basis in which the offdiagonal elements of $\mathbf{V}_0(Q)$ do not contain constant terms (the leading terms are at least linear in Q); this is precisely the diabatic basis (more precisely, this special version of diabatic basis, which always exists, is referred to as the crude adiabatic basis).

interaction potential is given by

$$\hat{\mathbf{V}}_{\text{int}}(t) = -\hat{\boldsymbol{\mu}} \cdot \vec{E}(t), \quad (1.13)$$

where $\hat{\boldsymbol{\mu}}$ is the molecular electric-dipole operator and $\vec{E}(t)$ is the electric field. See Appendix A for the derivation. In the preceding expression, the arrow refers to three-dimensional vectors.

Finally, as suggested in Eq. (1.12), sometimes it is useful to combine the molecular potential with the interaction potential into the total time-dependent potential

$$\hat{\mathbf{V}}(t) := \hat{\mathbf{V}}_0 + \hat{\mathbf{V}}_{\text{int}}(t). \quad (1.14)$$

1.2.3 Exact Solution of the Time-Dependent Schrödinger Equation

In the absence of an electromagnetic field, the molecular state evolves as

$$|\psi(t)\rangle = \hat{\mathbf{U}}_0(t - t_0)|\psi(t_0)\rangle, \quad t_0, t \leq t_i \text{ or } t_f \leq t_0, t, \quad (1.15)$$

where

$$\hat{\mathbf{U}}_0(t) := \hat{\mathbf{U}}_{\hat{\mathbf{H}}_0}(t) \quad (1.16)$$

is the molecular evolution operator and, for later convenience, we introduce notation for a unitary operator

$$\hat{\mathbf{U}}_{\hat{\mathbf{A}}}(t) := e^{-it\hat{\mathbf{A}}/\hbar} \quad (1.17)$$

generated by a time-independent Hermitian operator $\hat{\mathbf{A}}$. When the electromagnetic field is present, the *exact* evolution of the molecular state is given by

$$|\psi(t)\rangle = \hat{\mathbf{U}}(t, t_0)|\psi(t_0)\rangle, \quad t_0, t \in (t_i, t_f), \quad (1.18)$$

where

$$\hat{\mathbf{U}}(t, t_0) := \hat{\mathbf{U}}_{\hat{\mathbf{H}}(t')}(t, t_0) \quad (1.19)$$

is the exact evolution operator and where we introduce the notation for a unitary operator

$$\hat{\mathbf{U}}_{\hat{\mathbf{A}}(t')}(t, t_0) := \mathcal{T} \exp \left[-\frac{i}{\hbar} \int_{t_0}^t \hat{\mathbf{A}}(t') dt' \right] \quad (1.20)$$

generated by a time-dependent Hermitian operator $\hat{\mathbf{A}}(t)$. In Eq. (1.20), \mathcal{T} denotes the time-ordering operator [117].

1.2.4 Description of the Electric Field

Although our analytical results are general, in all our numerical calculations, the following form of the electric field is used

$$\begin{aligned}\vec{E}(t) &:= \vec{\epsilon} E(t), \\ E(t) &:= E_0 \mathcal{E}(t) \cos(\omega_{\text{pulse}} t + \varphi_{\text{pulse}}),\end{aligned}\tag{1.21}$$

where $\vec{\epsilon}$, E_0 , ω_{pulse} , φ_{pulse} , and $\mathcal{E}(t)$ denote polarization ($\|\vec{\epsilon}\| = 1$), amplitude, carrier frequency, phase, and slowly varying envelope, respectively. In order to simplify notation, we rewrite the interaction potential as

$$\hat{\mathbf{V}}_{\text{int}}(t) = -\hat{\boldsymbol{\mu}} E(t),\tag{1.22}$$

where $\hat{\boldsymbol{\mu}} := \hat{\boldsymbol{\mu}} \cdot \vec{\epsilon}$.

A Gaussian shape is assumed for the envelope of the pulse, i.e.,

$$\mathcal{E}(t) := \mathcal{N} e^{-(t-t_m)^2/2\Delta t_{\text{pulse}}^2},\tag{1.23}$$

where its normalization factor \mathcal{N} is chosen to be $\sqrt{\frac{2}{\pi}} \frac{1}{\Delta t_{\text{pulse}}}$ and its width is controlled by Δt_{pulse} that is related to the full-width at half-maximum (FWHM) by

$$\text{FWHM} := 2\sqrt{2 \ln 2} \Delta t_{\text{pulse}}.\tag{1.24}$$

Finally, the pulse is assumed to be fully contained in the time interval $(t_i, t_f) := (t_m - 4\Delta t_{\text{pulse}}, t_m + 4\Delta t_{\text{pulse}})$. The interaction potential is, hence, negligible before initial time t_i and after final time t_f .

1.3 Split-Operator Method

Our method of choice to implement the two formal solutions of the evolved molecular state, Eqs. (1.15) and (1.20), is the split-operator algorithm. Usually, it is split into two parts, one of which depends only on the momenta, and the other only on the coordinates. The basic idea is to first decompose the full evolution into a number of small time steps Δt . Then, for each of these steps, the evolution of the molecular state can be approximated to second-order as [65]

$$\exp(-i\hat{\mathbf{H}}_0\Delta t/\hbar) = \exp(-i\hat{\mathbf{T}}\Delta t/2\hbar) \exp(-i\hat{\mathbf{V}}_0\Delta t/\hbar) \exp(-i\hat{\mathbf{T}}\Delta t/2\hbar) + \mathcal{O}(\Delta t^3)\tag{1.25}$$

in the absence of the electromagnetic field, and as [70]

$$\exp\left[-\frac{i}{\hbar} \int_t^{t+\Delta t} \hat{\mathbf{H}}(t') dt'\right] = e^{-\frac{i}{2\hbar} \hat{\mathbf{T}}\Delta t} e^{-\frac{i}{\hbar} \hat{\mathbf{V}}(t+\frac{\Delta t}{2})\Delta t} e^{-\frac{i}{2\hbar} \hat{\mathbf{T}}\Delta t} + \mathcal{O}(\Delta t^3),\tag{1.26}$$

when the field is present. Similarly, we can also have

$$\exp(-i\hat{\mathbf{H}}_0\Delta t/\hbar) = \exp(-i\hat{\mathbf{V}}_0\Delta t/2\hbar) \exp(-i\hat{\mathbf{T}}\Delta t/\hbar) \exp(-i\hat{\mathbf{V}}_0\Delta t/2\hbar) + \mathcal{O}(\Delta t^3) \quad (1.27)$$

and

$$\exp\left[-\frac{i}{\hbar}\int_t^{t+\Delta t}\hat{\mathbf{H}}(t')dt'\right] = e^{-\frac{i}{2\hbar}\hat{\mathbf{V}}(t+\Delta t)\Delta t}e^{-\frac{i}{\hbar}\hat{\mathbf{T}}\Delta t}e^{-\frac{i}{2\hbar}\hat{\mathbf{V}}(t)\Delta t} + \mathcal{O}(\Delta t^3). \quad (1.28)$$

Note that in Eq. (1.26), the full potential energy $\hat{\mathbf{V}}(t)$ is evaluated at the midpoint, whereas in Eq. (1.28) it is evaluated on the edges of the time interval. The expressions (1.25)–(1.28) suggest that the quantum state can be easily evolved alternately, either with the kinetic energy $\hat{\mathbf{T}}$ in the momentum representation, where $\exp(-i\hat{\mathbf{T}}\Delta t/\hbar)$ is diagonal, or with the potential energy $\hat{\mathbf{V}}(t)$ in the coordinate representation. Note that due to the vibronic and transition dipole moment couplings, as the propagation is diagonal in either coordinate or momentum representation, we must perform an exponential of an $S \times S$ matrix $\mathbf{V}(Q, t)$ at each nuclear coordinate Q , in order to account for the transitions between electronic states. Curiously, the most expensive part of the propagation turns out to be the switching between the coordinate and momentum representation that uses Fourier method [49] that is implemented via the powerful fast Fourier transform algorithm [58, 118, 119].

The action of the Fourier transform can also be thought of in another way. Indeed, when applied to the wavefunction in coordinate representation, it can be seen as a transformation to a basis representation (composed of linear momentum basis functions) of the wavefunction where each obtained element corresponds to the weight of the given basis function.

For simplicity, we restrict the presentation of the evolution of the molecular operator Eqs. (1.25)–(1.28) to the standard second-order algorithms. But, we implement these integrators with an arbitrary order of accuracy in the time step for cartesian coordinates, which will be discussed in detail in Chapter 3.

1.4 Time-Dependent Picture of Linear Spectroscopy

1.4.1 Electric-Dipole Spectrum

The rate of change of the molecule's energy, the power $\mathcal{P}(t)$, can be evaluated as the time derivative of the expectation value of the total Hamiltonian [46, 120]

$$\mathcal{P}(t) = \frac{d}{dt}\langle\psi(t)|\hat{\mathbf{H}}(t)|\psi(t)\rangle = -P(t)\dot{E}(t), \quad (1.29)$$

where the polarization $P(t)$ has been introduced and reads

$$P(t) = \langle\psi(t)|\hat{\boldsymbol{\mu}}|\psi(t)\rangle. \quad (1.30)$$

Introduction

Time integration of Eq. (1.29) enables us to obtain the total energy absorbed per unit frequency $H(\omega)$ as

$$\Delta E_{\text{mol}} = \int_{\mathbb{R}} \mathcal{P}(t) dt = \int_{\mathbb{R}} H(\omega) d\omega, \quad (1.31)$$

$$H(\omega) = -2\pi\omega \text{Im} \left[\tilde{P}^*(\omega) \tilde{E}(\omega) \right], \quad (1.32)$$

where we use the definition of Fourier transform

$$\tilde{f}(\omega) = \frac{1}{2\pi} \int_{\mathbb{R}} f(t) e^{i\omega t} dt, \quad (1.33)$$

the fact that $P(t)$ is an observable, the Plancherel theorem, and the Fourier-derivative relation, i.e.,

$$\begin{aligned} P(t) &= P^*(t), \\ \int_{\mathbb{R}} f^*(t) g(t) dt &= 2\pi \int_{\mathbb{R}} f^*(\omega) g(\omega) d\omega, \text{ and} \\ \dot{\tilde{f}}(\omega) &= -i\omega \tilde{f}(\omega). \end{aligned}$$

The spectrum or, more specifically, the frequency-dependent cross section for the energy transfer from the field to the molecule, is then given by

$$\sigma(\omega) = \frac{H(\omega)}{I(\omega)} = -\frac{4\pi\omega}{c} \frac{\text{Im} \left[\tilde{P}^*(\omega) \tilde{E}(\omega) \right]}{|\tilde{E}(\omega)|^2}, \quad (1.34)$$

where $I(\omega) = c |\tilde{E}(\omega)|^2 / 2$ denotes the total incident energy per unit area and unit frequency (obtained via the definition of the Poynting vector in frequency domain) and c is the speed of light in vacuum.

Eq. (1.34) defines the nonperturbative expression of the electric-dipole spectrum, hence, it is valid independently of the electric field strength. In addition, it applies to linear, as well as nonlinear, phenomena.

1.4.2 Linear Electric-Dipole Spectrum

Most of the experiments require relatively weak electric fields. Therefore, time-dependent perturbation theory can be used to compute the time-dependent polarization. The linear electric-dipole spectrum is then obtained by substituting the polarization by its linearized version [103] in the general nonperturbative expression Eq. (1.34).

In more detail, when the molecular state is expanded in a power series as

$$|\psi(t)\rangle = \sum_n \lambda^n |\psi^{(n)}(t)\rangle, \quad (1.35)$$

where λ is a dimensionless parameter that can take values ranging from 0 (no perturba-

tion) to 1 (full perturbation), the time-dependent perturbation theory expansion of the polarization reads (using $\lambda = 1$)

$$\begin{aligned} P(t) &= P^{(0)}(t) + P^{(1)}(t) + \dots \\ &= \langle \psi^{(0)}(t) | \hat{\mu} | \psi^{(0)}(t) \rangle + \langle \psi^{(0)}(t) | \hat{\mu} | \psi^{(1)}(t) \rangle + \langle \psi^{(1)}(t) | \hat{\mu} | \psi^{(0)}(t) \rangle + \dots \end{aligned} \quad (1.36)$$

In isotropic media, when averaging over the orientation of the molecule, the even-order terms [here $P^{(0)}(t)$] vanish, hence the importance of the first-order term.

To demonstrate its evaluation, we assume absorption in a two-level system with the Hamiltonian

$$\begin{aligned} \hat{\mathbf{H}} &= \hat{\mathbf{H}}_0 + \hat{\mathbf{V}}_{\text{int}} \\ &= \begin{pmatrix} \hat{H}_g & 0 \\ 0 & \hat{H}_e \end{pmatrix} + \begin{pmatrix} 0 & -\hat{\mu}_{ge}E(t) \\ -\hat{\mu}_{eg}E(t) & 0 \end{pmatrix} \end{aligned} \quad (1.37)$$

and the initial wavefunction ($t_0 = 0$) being the ground vibrational state of the electronic ground state, i.e.,

$$|\psi(0)\rangle = \begin{pmatrix} |g, 0\rangle \\ 0 \end{pmatrix} \quad (1.38)$$

with zero point energy $\hbar\omega_{g,0}$. Note that no nonadiabatic couplings are considered, i.e., the levels are exclusively coupled via the electric field and $\hat{\mu}_{eg} = \hat{\mu}_{ge}$ is the Hermitian transition dipole moment operator between ground and excited electronic states projected along a certain unit polarization vector $\vec{\epsilon}$, i.e., $\hat{\mu}_{eg} := \hat{\mu}_{eg} \cdot \vec{\epsilon}$.

At time t , we have

$$|\psi^{(0)}(t)\rangle = \begin{pmatrix} e^{-i\hat{H}_g t/\hbar} |g, 0\rangle \\ 0 \end{pmatrix} = \begin{pmatrix} e^{-i\omega_{g,0}t} |g, 0\rangle \\ 0 \end{pmatrix}, \quad (1.39)$$

$$|\psi^{(1)}(t)\rangle = \begin{pmatrix} 0 \\ \frac{i}{\hbar} \int_0^t e^{-i\hat{H}_e(t-t')/\hbar} \hat{\mu}_{eg} E(t') e^{-i\omega_{g,0}t'} |g, 0\rangle dt' \end{pmatrix}. \quad (1.40)$$

Therefore, the first-order polarization can be rewritten as

$$P^{(1)}(t) = \frac{i}{\hbar} \int_0^t C_{\mu\mu}(t-t') E(t') dt' + \text{c.c.} \quad (1.41)$$

where the dipole-dipole time autocorrelation function $C_{\mu\mu}(t)$ has been introduced and reads

$$C_{\mu\mu}(t) = \langle g, 0 | \hat{U}_g(-t) \hat{\mu}_{ge} \hat{U}_e(t) \hat{\mu}_{eg} | g, 0 \rangle \quad (1.42)$$

$$= \langle g, 0 | \hat{\mu}_{ge} \hat{U}_e(t) \hat{\mu}_{eg} | g, 0 \rangle e^{i\omega_{g,0}t}. \quad (1.43)$$

Note that $\hat{U}_n(t) = e^{-i\hat{H}_n t/\hbar}$ is the time evolution operator on the n th electronic state.

In order to obtain the absorption cross section, the first-order polarization needs to be

expressed in frequency domain. To do so, first, we define

$$S_{\mu\mu}(t) = \begin{cases} C_{\mu\mu}(t) & t \geq 0 \\ 0 & t < 0 \end{cases} \quad (1.44)$$

and perform a change of variables in the expression for the first-order polarization such that it becomes

$$P^{(1)}(t) = \frac{i}{\hbar} (S * E)(t) + \text{c.c.}, \quad (1.45)$$

where $*$ denotes a convolution, i.e., $(f * g)(t) = \int_{\mathbb{R}} d\tau f(\tau)g(t - \tau)$. Then, using the Fourier convolution theorem

$$\widetilde{f * g}(\omega) = 2\pi \tilde{f}(\omega)\tilde{g}(\omega)$$

on the right-hand side of Eq. (1.45), the spectral representation of the first-order polarization is given by

$$\tilde{P}^{(1)}(\omega) = \frac{2\pi i}{\hbar} \tilde{S}(\omega)\tilde{E}(\omega) + \text{c.c.} \quad (1.46)$$

Finally, insertion of the first-order polarization Eq. (1.46) into Eq. (1.34) leads to the linear electric-dipole absorption spectrum

$$\sigma(\omega) = \frac{8\pi^2\omega}{\hbar c} \text{Re} [\tilde{S}(\omega)] + \text{c.c.} \quad (1.47)$$

The main contribution to the $e \leftarrow g$ absorption process is given by the first term of Eq. (1.47), thus, the absorption cross section reduces to

$$\sigma(\omega) = \frac{4\pi\omega}{\hbar c} \text{Re} \left[\int_0^\infty C_{\mu\mu}(t)e^{i\omega t} dt \right] = \frac{2\pi\omega}{\hbar c} \int_{\mathbb{R}} C_{\mu\mu}(t)e^{i\omega t} dt. \quad (1.48)$$

We focus here on the vibrational ground state, but the absorption cross section computed as Fourier transform of dipole-dipole autocorrelation function is also valid for any other vibrational eigenstate or for Boltzmann distribution. Moreover, Eq.(1.48) can be used for continuous wave, as well as pulsed laser experiments as there is no explicit dependence on the electric field.

1.4.3 Linear Electric-Dipole Spectrum and Orientational Averaging

Up to this point, we have assumed a given relative orientation of the electric field. However, in an experiment, the molecules are isotropically distributed in the sample and, when computing an observable, we must average over all different orientations. Another way to solve the problem is to assume, instead, that all molecules are aligned and that the field is isotropic. Using a unit polarization vector of the form

$$\vec{\epsilon} = \begin{pmatrix} \sin \theta \cos \phi \\ \sin \theta \sin \phi \\ \cos \theta \end{pmatrix}, \quad (1.49)$$

1.4. Time-Dependent Picture of Linear Spectroscopy

and rewriting the dipole-dipole autocorrelation function as

$$C_{\mu\mu}(t) = \vec{\epsilon}^T \cdot C_{\vec{\mu}\vec{\mu}}(t) \cdot \vec{\epsilon}, \quad (1.50)$$

where $C_{\vec{\mu}\vec{\mu}}(t) := \langle g, 0 | \hat{\vec{\mu}}_{ge} \hat{U}_e(t) \hat{\vec{\mu}}_{eg} | g, 0 \rangle e^{i\omega_{g,0}t}$ is the three-dimensional dipole-dipole autocorrelation tensor, the orientational average gives

$$\begin{aligned} \langle C_{\mu\mu}(t) \rangle_{\text{or. av.}} &= \frac{1}{4\pi} \int_{S^2} d\Omega C_{\mu\mu}(t, \theta, \phi) = \frac{1}{4\pi} \int_0^\pi \sin \theta d\theta \int_0^{2\pi} d\phi C_{\mu\mu}(t, \theta, \phi) \\ &= \frac{1}{3} \text{Tr} [C_{\vec{\mu}\vec{\mu}}(t)]. \end{aligned} \quad (1.51)$$

The absorption cross section is therefore

$$\sigma_{\text{or. av.}}(\omega) = \frac{2\pi\omega}{3\hbar c} \int_{\mathbb{R}} \text{Tr}[C_{\vec{\mu}\vec{\mu}}(t)] e^{i\omega t} dt. \quad (1.52)$$

It has to be noticed that we do not need an infinite number of polarizations of the field; three are sufficient. Indeed, the transition dipole moment has to be projected on three orthogonal polarizations of the electric field for a given orientation of the molecule. If, instead, we assume a fixed polarization of the field, the molecule must be oriented along three arbitrary orthogonal axes in order to take into account the isotropic distribution of the sample.

If, on top of that, we make the Condon approximation, the transition dipole moment is no longer a function of the nuclear position and Eq. (1.43) simplifies further to

$$C_{\mu\mu}(t) \approx C_{\mu\mu,c}(t) = \mu_{eg}^2 C(t) e^{i\omega_{g,0}t}, \quad (1.53)$$

where $C(t) := \langle g, 0 | \hat{U}_e(t) | g, 0 \rangle$ is the wavepacket autocorrelation function. In this case, the orientational averaging is trivial and given by

$$\begin{aligned} \langle C_{\mu\mu,c}(t) \rangle_{\text{or. av.}} &= \langle |\vec{\mu}_{eg} \cdot \vec{\epsilon}|^2 \rangle_{\text{or. av.}} C(t) e^{i\omega_{g,0}t}, \\ \langle |\vec{\mu}_{eg} \cdot \vec{\epsilon}|^2 \rangle_{\text{or. av.}} &= \frac{|\vec{\mu}_{eg}|^2}{3}, \end{aligned} \quad (1.54)$$

which leads to the well-known textbook absorption cross section formula [46]

$$\sigma_{\text{or. av.,c}}(\omega) = \frac{2\pi\omega}{3\hbar c} |\vec{\mu}_{eg}|^2 \int_{\mathbb{R}} C(t) e^{i(\omega_{g,0} + \omega)t} dt, \quad (1.55)$$

where only the absolute value of the transition dipole moment matters.

Finally, if we focus on nonlinear spectroscopy such as time-resolved stimulated emission, we need to expand the time-dependent polarization up to third-order.

2 Approximations for the Molecule-Field Interaction

In order to help experimentalists to better understand the outcome of their experiments, the role of theorists is to develop efficient tools that are able to accurately describe molecular systems. For low-dimensional systems, solving the time-dependent Schrödinger equation is the most accurate and straightforward approach. However, it can be time consuming to apply numerical algorithms that employ the exact treatment of the interaction between quantum matter and a classical electromagnetic field; therefore, it is worth using approximations to accelerate calculations. In this chapter, we define and derive four of the most common approximations in relation to light-matter interaction: the time-dependent perturbation theory, the Condon, rotating-wave, and ultrashort-pulse approximations, as well as every possible combination thereof. It is not uncommon for one, or even a combination of these approximations, to be employed without previous knowledge of its validity. In order to avoid such problems, we predict the validity of these four basic approximations and their combinations by defining corresponding dimensionless parameters. Using one-dimensional model systems, we show how several approximations can work or break down, together with their performance compared to the exact quantum calculation. Furthermore, we use several approximate methods in a more realistic example: a pump-probe experiment applied to a three-dimensional model of pyrazine. The results of this chapter can be found in Ref. [121].

2.1 Basic Approximations

We describe several approximations to the exact propagation given by Eq. (1.18). In particular, we find approximations to the exact evolution operator $\hat{U}(t_f, t_i)$, where the interval (t_i, t_f) contains the full laser pulse. Outside of this interval, the molecular state can be propagated with the field-free molecular evolution operator \hat{U}_0 of Eq. (1.15). Since we would like to discuss combinations of various approximations, it is useful to think in terms of independent elementary approximations, or “generators.” The four basic generators that we consider are the Condon approximation, time-dependent perturbation theory, rotating-wave approximation, and ultrashort-pulse approximation; if these basic

approximations are combined independently, we obtain $2^4 = 16$ combinations (see Fig. 2.1). In addition, we define dimensionless parameters which allow to predict the validity of a given approximation. We assume all the basic approximations to be valid when we design a dimensionless parameter. Throughout this thesis, we use the abbreviations of the basic approximations defined in Table 2.1.

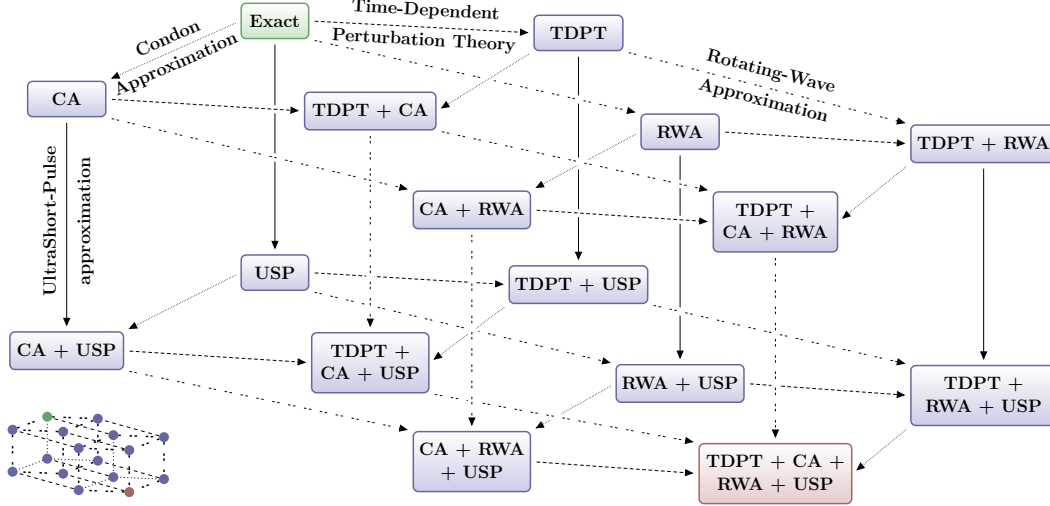


Figure 2.1 – Approximations involved in molecular quantum dynamics induced by the interaction with the electromagnetic field. Different approximations are distinguished by different line types: dotted lines = CA, dashed lines = TDPT, double dashed lines = RWA, and solid lines = USP approximation. The exact method is represented in green, approximations in blue, and the most approximate method in red.

Table 2.1 – Abbreviations of the basic approximations used in the formulas.

Basic approximation	Abbreviation
Condon approximation (CA)	c
Time-dependent perturbation theory (TDPT)	p
Rotating-wave approximation (RWA)	r
Ultrashort-pulse (USP) approximation	u

2.1.1 Condon Approximation

The Condon approximation assumes that the electric dipole moment is independent of nuclear position,

$$\begin{aligned}\vec{\mu}(Q) &\approx \vec{\mu}_c(Q) := \vec{\mu}(Q_0), \text{ i.e.,} \\ \hat{\vec{\mu}}_c &\equiv \hat{1}\vec{\mu}_c.\end{aligned}\tag{2.1}$$

Within the Condon approximation, the evolution operator $\hat{\mathbf{U}}_c(t_f, t_i)$ is given by Eq. (1.19) in which the interaction potential contained in $\hat{\mathbf{H}}(t)$ is modified according to Eq. (2.1) as

$$\hat{\mathbf{V}}_{\text{int},c}(t) \equiv \hat{\mathbf{1}}\mathbf{V}_{\text{int},c}(t). \quad (2.2)$$

Note that since $\hat{\mathbf{H}}_c(t) = \hat{\mathbf{T}} + \hat{\mathbf{V}}_{\text{int},c}(t)$ is Hermitian, the approximate evolution operator $\hat{\mathbf{U}}_c(t_f, t_i)$ remains unitary.

In order to be valid, the first derivative of the transition dipole moment μ'_{nm} times the width of the wavepacket σ divided by the constant transition dipole moment term must be much smaller than unity, i.e.,

$$\epsilon_c = \left| \frac{\mu'_{nm}(Q_0)\sigma}{\mu_{nm}(Q_0)} \right| \ll 1. \quad (2.3)$$

2.1.2 Time-Dependent Perturbation Theory

In standard texts, time-dependent perturbation theory is derived either for discrete or continuous degrees of freedom, but with our notation, the derivation is almost identical in the molecular setting with Hilbert space $\mathbb{C}^S \otimes \mathcal{L}^2(\mathbb{R}^D)$. As usual, we employ the interaction (I) picture [122], in which the evolved state is defined to be

$$|\psi_I(t)\rangle := \hat{\mathbf{U}}_0(-t)|\psi(t)\rangle. \quad (2.4)$$

Substitution of this definition into the time-dependent Schrödinger equation (1.11) yields

$$i\hbar \frac{d}{dt} |\psi_I(t)\rangle = \hat{\mathbf{V}}_{\text{int},I}(t) |\psi_I(t)\rangle, \quad (2.5)$$

i.e., the time-dependent Schrödinger equation in the interaction picture, in which the interaction potential is given by

$$\hat{\mathbf{V}}_{\text{int},I}(t) := \hat{\mathbf{U}}_0(-t) \hat{\mathbf{V}}_{\text{int}}(t) \hat{\mathbf{U}}_0(t). \quad (2.6)$$

Formal time integration of Eq. (2.5) yields an exact integral equation for $|\psi_I(t)\rangle$,

$$|\psi_I(t)\rangle = |\psi_I(t_0)\rangle - \frac{i}{\hbar} \int_{t_0}^t dt' \hat{\mathbf{V}}_{\text{int},I}(t') |\psi_I(t')\rangle. \quad (2.7)$$

By approximating $|\psi_I(t')\rangle$ with $|\psi_I(t_0)\rangle$ on the right-hand side, one obtains the first-order time-dependent perturbation theory result in the interaction picture,

$$|\psi_I(t)\rangle \approx \left[\hat{\mathbf{1}} - \frac{i}{\hbar} \int_{t_0}^t dt' \hat{\mathbf{V}}_{\text{int},I}(t') \right] |\psi_I(t_0)\rangle, \quad (2.8)$$

which, by employing Eq. (2.4), can be translated into the Schrödinger picture:

$$|\psi(t)\rangle \approx \hat{\mathbf{U}}_p(t, t_0) |\psi(t_0)\rangle. \quad (2.9)$$

The first-order perturbation theory gives the approximate, nonunitary evolution operator as

$$\hat{\mathbf{U}}_p(t, t_0) := \hat{\mathbf{U}}_0(t - t_0) - \frac{i}{\hbar} \int_{t_0}^t dt' \hat{\mathbf{U}}_0(t - t') \hat{\mathbf{V}}_{\text{int}}(t') \hat{\mathbf{U}}_0(t' - t_0). \quad (2.10)$$

To make sure that time-dependent perturbation theory is valid, the integral of the perturbation divided by the reduced Planck constant must be much smaller than unity, i.e.,

$$\epsilon_p = \frac{\left| \int_{t_i}^{t_f} (\tilde{V}_{\text{int},rc})_{nm}(t) dt \Delta t_{\text{pulse}} \right|}{\hbar} = \frac{|\mu_{nm}(Q_0) E_0 \Delta t_{\text{pulse}}|}{\hbar} \ll 1. \quad (2.11)$$

Note that $\tilde{\mathbf{V}}_{\text{int},rc}(t)$ assumes the transition dipole moment to be in the Condon approximation and that the electric field reduces to its slowly varying envelope.

2.1.3 Rotating-Wave Approximation

Assuming that the electromagnetic field is nearly in resonance with a particular electronic transition, it is useful to use the rotating-wave approximation. This approximation is best understood in the so-called rotating frame, where the molecular state is transformed as

$$|\tilde{\psi}(t)\rangle := \mathbf{W}(t)^{-1} |\psi(t)\rangle, \quad (2.12)$$

using a unitary transformation

$$\mathbf{W}(t) := \exp(-i\omega_{\text{pulse}} t \mathbf{\Pi}) = \text{diag} \left(1, e^{-i\omega_{\text{pulse}} t}, e^{-i\omega_{\text{pulse}} t} \right), \quad (2.13)$$

where

$$\mathbf{\Pi} := \text{diag}(0, 1, 1) \quad (2.14)$$

is the projection on the subspace spanned by the two excited states. In the new, time-dependent basis, all basis functions oscillate with frequency ω_{pulse} except for the electronic ground state, which remains time-independent. A three-state formulation, in which transitions to both states 2 and 3 are approximately resonant, was used for simplicity of exposition, but the rotating-wave approximation can be easily generalized to an S -state problem.

Insertion of Eq. (2.12) into Eq. (1.11) yields the exact time-dependent Schrödinger equation in the rotating frame,

$$i\hbar \frac{d}{dt} |\tilde{\psi}(t)\rangle = \hat{\mathbf{H}}(t) |\tilde{\psi}(t)\rangle, \quad (2.15)$$

where the tilde above a symbol denotes a state or operator in the rotating frame and where

the transformed Hamiltonian is defined by

$$\begin{aligned}\hat{\mathbf{H}}(t) &:= \mathbf{W}(t)^{-1} \hat{\mathbf{H}}(t) \mathbf{W}(t) - i\hbar \mathbf{W}(t)^{-1} \dot{\mathbf{W}}(t) \\ &= \mathbf{W}(t)^{-1} \hat{\mathbf{H}}(t) \mathbf{W}(t) - \hbar\omega_{\text{pulse}} \mathbf{\Pi} \hat{\mathbf{1}} \\ &= \hat{\mathbf{T}} + \hat{\mathbf{V}}(t).\end{aligned}\tag{2.16}$$

In general, we define $\hat{\hat{\mathbf{A}}}(t) := \mathbf{W}(t)^{-1} \hat{\mathbf{A}}(t) \mathbf{W}(t) - \hbar\omega_{\text{pulse}} \mathbf{\Pi} \hat{\mathbf{1}}$ if $\hat{\mathbf{A}}(t)$ contains the electronic potential $\hat{\mathbf{V}}_e$ and $\hat{\hat{\mathbf{A}}}(t) := \mathbf{W}(t)^{-1} \hat{\mathbf{A}}(t) \mathbf{W}(t)$ if $\hat{\mathbf{A}}(t)$ does not contain $\hat{\mathbf{V}}_e$. In the last row of Eq. (2.16), $\hat{\mathbf{H}}(t)$ was expressed in terms of the transformed potential

$$\hat{\mathbf{V}}(t) := \hat{\mathbf{V}}_0 + \hat{\mathbf{V}}_{\text{int}}(t),\tag{2.17}$$

where the transformed molecular and interaction potentials are, in the three-state case of Eqs. (2.13) and (2.14), given by

$$\hat{\mathbf{V}}_0 = \begin{pmatrix} (\hat{V}_0)_{11} & (\hat{V}_0)_{12}e^{-i\omega_{\text{pulse}}t} & (\hat{V}_0)_{13}e^{-i\omega_{\text{pulse}}t} \\ e^{i\omega_{\text{pulse}}t}(\hat{V}_0)_{21} & (\hat{V}_0)_{22} - \hbar\omega_{\text{pulse}} & (\hat{V}_0)_{23} \\ e^{i\omega_{\text{pulse}}t}(\hat{V}_0)_{31} & (\hat{V}_0)_{32} & (\hat{V}_0)_{33} - \hbar\omega_{\text{pulse}} \end{pmatrix},\tag{2.18}$$

$$\hat{\mathbf{V}}_{\text{int}}(t) = -E_0\mathcal{E}(t)\cos(\omega_{\text{pulse}}t + \varphi_{\text{pulse}}) \begin{pmatrix} \hat{\mu}_{11} & \hat{\mu}_{12}e^{-i\omega_{\text{pulse}}t} & \hat{\mu}_{13}e^{-i\omega_{\text{pulse}}t} \\ e^{i\omega_{\text{pulse}}t}\hat{\mu}_{21} & \hat{\mu}_{22} & \hat{\mu}_{23} \\ e^{i\omega_{\text{pulse}}t}\hat{\mu}_{31} & \hat{\mu}_{32} & \hat{\mu}_{33} \end{pmatrix}.\tag{2.19}$$

Note that in Eq. (2.18) the energies of the excited states 2 and 3 were lowered by $\hbar\omega_{\text{pulse}}$ and that the offdiagonal couplings to the ground state contain additional time dependence $e^{\pm i\omega_{\text{pulse}}t}$ due to the change of basis. Recalling that $\mathcal{E}(t)$ is a slowly changing envelope function, we may collect the powers of $e^{\pm i\omega_{\text{pulse}}t}$ and neglect the highly oscillatory terms, including factors $e^{\pm 2i\omega_{\text{pulse}}t}$ and $e^{\pm i\omega_{\text{pulse}}t}$, in comparison with time-independent terms or terms depending on time only via $\mathcal{E}(t)$. This is the rotating-wave approximation, in which the Hamiltonian and potential are approximated as

$$\hat{\mathbf{H}}(t) \approx \hat{\mathbf{H}}_r(t) := \hat{\mathbf{T}} + \hat{\mathbf{V}}_r(t),\tag{2.20}$$

$$\hat{\mathbf{V}}_r(t) := \hat{\mathbf{V}}_{0,r} + \hat{\mathbf{V}}_{\text{int},r}(t),\tag{2.21}$$

where

$$\hat{\mathbf{V}}_{0,r} := \begin{pmatrix} (\hat{V}_0)_{11} & 0 & 0 \\ 0 & (\hat{V}_0)_{22} - \hbar\omega_{\text{pulse}} & (\hat{V}_0)_{23} \\ 0 & (\hat{V}_0)_{32} & (\hat{V}_0)_{33} - \hbar\omega_{\text{pulse}} \end{pmatrix},\tag{2.22}$$

$$\hat{\mathbf{V}}_{\text{int},r}(t) := -\frac{E_0}{2}\mathcal{E}(t) \begin{pmatrix} 0 & \hat{\mu}_{12}e^{-i\varphi_{\text{pulse}}} & \hat{\mu}_{13}e^{-i\varphi_{\text{pulse}}} \\ \hat{\mu}_{21}e^{i\varphi_{\text{pulse}}} & 0 & 0 \\ \hat{\mu}_{31}e^{i\varphi_{\text{pulse}}} & 0 & 0 \end{pmatrix}.\tag{2.23}$$

Chapter 2. Approximations for the Molecule-Field Interaction

One may now invert the transformation (2.16) to transform the rotating-wave approximation Hamiltonian (2.20) back to the original diabatic basis to obtain $\hat{\mathbf{H}}_r(t)$ and find the rotating-wave approximation evolution operator as $\hat{\mathbf{U}}_r(t, t_0) = \hat{\mathbf{U}}_{\hat{\mathbf{H}}_r(t')}(t, t_0)$. Numerically, however, it is obviously much easier to perform the evolution in the rotating frame and only transform back to the original basis—if needed—at the end of the evolution. In the original, diabatic basis, the rotating-wave approximation evolution operator is thus given by

$$\hat{\mathbf{U}}_r(t, t_0) := \mathbf{W}(t) \hat{\mathbf{U}}_r(t, t_0) \mathbf{W}(t_0)^{-1} \quad (2.24)$$

$$\hat{\mathbf{U}}_r(t, t_0) := \hat{\mathbf{U}}_{\hat{\mathbf{H}}_r(t')}(t, t_0), \quad (2.25)$$

where $\hat{\mathbf{U}}_r$ is the rotating-wave approximation evolution operator in the rotating frame. Note that since $\hat{\mathbf{H}}_r(t)$ is Hermitian, the approximate evolution operator $\hat{\mathbf{U}}_r(t, t_0)$ remains unitary.

Finally, for future reference, it is useful to list all relations between the exact expressions and rotating-wave approximations for the four separate components of $\hat{\mathbf{H}}(t) = \hat{\mathbf{H}}_n + \hat{\mathbf{I}}\mathbf{V}_e + \hat{\mathbf{V}}_{ne} + \hat{\mathbf{V}}_{int}(t)$, expressed either in the rotating frame or in the Schrödinger picture:

$$\hat{\mathbf{H}}_{n,r} = \hat{\mathbf{H}}_n = \hat{\mathbf{H}}_n = \hat{\mathbf{H}}_{n,r}, \quad (2.26)$$

$$\tilde{\mathbf{V}}_{e,r} = \tilde{\mathbf{V}}_e = \mathbf{V}_e - \hbar\omega_{\text{pulse}}\mathbf{\Pi}, \quad (2.27)$$

$$\mathbf{V}_{e,r} = \mathbf{V}_e, \quad (2.28)$$

$$\hat{\mathbf{V}}_{ne,r} = \hat{\mathbf{V}}_{ne,r}. \quad (2.29)$$

In particular, the rotating-wave approximation only affects $\hat{\mathbf{V}}_{ne}$ and $\hat{\mathbf{V}}_{int}(t)$, and does not change $\hat{\mathbf{H}}_n$ and $\hat{\mathbf{I}}\mathbf{V}_e$. Moreover, the transformation into the rotating frame does not change $\hat{\mathbf{H}}_n$ and, within the rotating-wave approximation, $\hat{\mathbf{V}}_{ne,r}$, but transforms \mathbf{V}_e into $\mathbf{V}_e - \hbar\omega_{\text{pulse}}\mathbf{\Pi}$.

In order to be valid, two conditions must be fulfilled [34–36, 40]. The first one assumes that the detuning [the difference between the frequency of the laser and the vertical electronic transition ($\omega_e)_{nm}$ in frequency unit], $\Delta = |\omega_{\text{pulse}} - (\omega_e)_{nm}|$, must be much smaller than the laser frequency itself

$$\epsilon'_r = \frac{\Delta}{\omega_{\text{pulse}}} \ll 1. \quad (2.30)$$

Note that all calculations of this thesis that involved the rotating-wave approximation assume the resonant condition, i.e., $\epsilon'_r = 0$.

The second one requires that the biggest Rabi frequency $\Omega_R = \frac{\mu_{nm}(Q_0)E_0\mathcal{E}(t_m)}{\hbar} = \sqrt{\frac{2}{\pi}} \frac{\mu_{nm}(Q_0)E_0}{\hbar\Delta t_{\text{pulse}}}$ must be much smaller than the vertical electronic transition in frequency unit

$$\epsilon_r = \frac{\Omega_R}{(\omega_e)_{nm}} \ll 1. \quad (2.31)$$

2.1.4 Ultrashort-Pulse Approximation

Due to their very different weights, nuclei and electrons usually evolve on different time scales, the typical period t_n of nuclear motion being of the order of $100 \text{ fs} = 10^{-13} \text{ s}$, while that of electrons $t_e \approx 1 \text{ fs} = 10^{-15} \text{ s}$. In the ultrashort-pulse approximation, the full-width at half-maximum of the pulse is assumed to be much shorter than the nuclear time scale, but much longer than the electronic time scale,

$$t_e \ll \text{FWHM} \ll t_n. \quad (2.32)$$

As a result, the nuclear dynamics can be ignored, or—more precisely—separated from the electronic dynamics during the interaction of the molecule with the pulse. The separation of the nuclear dynamics is done by splitting the Hamiltonian as

$$\hat{\mathbf{H}}(t) \equiv \hat{\mathbf{H}}_{n+ne} + \hat{\mathbf{V}}_{e+int}(t), \quad (2.33)$$

where the first term, $\hat{\mathbf{H}}_{n+ne}$ contains both the nuclear Hamiltonian and vibronic coupling [see Eq. (1.9)], while the second term is the effective Hamiltonian during the interaction:

$$\hat{\mathbf{V}}_{e+int}(t) := \hat{\mathbf{I}}\mathbf{V}_e + \hat{\mathbf{V}}_{int}(t). \quad (2.34)$$

The evolution of the molecule from initial time t_i to final time t_f is effected with the approximate yet unitary evolution operator

$$\hat{\mathbf{U}}_u(t_f, t_i) := \hat{\mathbf{U}}_{\hat{\mathbf{H}}_{n+ne}}(t_f - t_m) \hat{\mathbf{U}}_{\hat{\mathbf{V}}_{e+int}(t)}(t_f, t_i) \hat{\mathbf{U}}_{\hat{\mathbf{H}}_{n+ne}}(t_m - t_i). \quad (2.35)$$

In Eq. (2.35), the effect of the pulse is taken into account with $\hat{\mathbf{U}}_{\hat{\mathbf{V}}_{e+int}(t)}(t_f, t_i)$, which treats the pulse instantaneously with respect to nuclei but explicitly, from time t_i to t_f , with respect to electrons.

The condition for the ultrashort-pulse approximation to be valid is such that the motion of the nuclear wavepacket on the excited state m during the interaction with the pulse (considering only the bulk of the pulse, i.e., its full-width at half-maximum) and using a classical picture must be smaller than the initial width of the wavepacket for the given nuclear degree of freedom, i.e.,

$$\epsilon_u = \frac{4\Delta Q_{mn} \text{FWHM}/(T_n)_m}{\sigma} \ll 1, \quad (2.36)$$

where $\Delta Q_{mn} = |(Q_0)_m - (Q_0)_n|$ is the nuclear displacement of the state m [$(Q_0)_m$ is its minimum position] with respect to state n and $(T_n)_m$ is the nuclear period of motion on the state m .

Moreover, as mentioned in the introduction, the nonadiabatic dynamics on the electronic state of interest, if it exists, must be small in the region of excitation. A way to control such phenomena is to observe the decay of the population of the given electronic state.

2.2 Combinations of the Basic Approximations

In this section, we describe various combinations of the basic approximations from Sec. 2.1; in other words, we go through all the layers of Fig. 2.1. Note that throughout this thesis, commutativity is not employed in its strict form, i.e., it holds only if the approximations are valid and does not if they break down.

2.2.1 Combinations with Condon Approximation

The easiest combinations to treat are all combinations with the Condon approximation; the only difference from a corresponding method without the Condon approximation is substitution of the approximate, coordinate-independent dipole moment (2.1). Below we therefore describe in detail only combinations that do not include the Condon approximation. Nevertheless, we point out that since the dipole moment and hence the interaction potential is independent of position [$\hat{\mathbf{V}}_{\text{int},c}(t) \equiv \hat{\mathbf{I}}\mathbf{V}_{\text{int},c}(t)$], invoking the Condon approximation simplifies the numerical implementation significantly. In particular, any combinations with the time-dependent perturbation theory or ultrashort-pulse approximation are greatly simplified since the molecular operators $\hat{\mathbf{U}}_{\hat{\mathbf{V}}_{\text{int}}(t)}$ and $\hat{\mathbf{U}}_{\hat{\mathbf{V}}_{\text{e+int}}(t)}$ in Eqs. (2.10) and (2.35) become just electronic operators: $\hat{\mathbf{U}}_{\hat{\mathbf{V}}_{\text{int}}(t)} \rightarrow \hat{\mathbf{I}}\mathbf{U}_{\mathbf{V}_{\text{int}}(t)}$ and $\hat{\mathbf{U}}_{\hat{\mathbf{V}}_{\text{e+int}}(t)} \rightarrow \hat{\mathbf{I}}\mathbf{U}_{\mathbf{V}_{\text{e+int}}(t)}$.

2.2.2 Time-Dependent Perturbation Theory and Rotating-Wave Approximation

This combination is obtained by applying the perturbation theory (2.10) to the rotating-wave approximation (2.24). In the rotating frame, the approximate Hamiltonian $\hat{\mathbf{H}}_r(t)$ is split into the unperturbed part and perturbation as

$$\hat{\mathbf{H}}_r(t) \equiv \hat{\mathbf{H}}_{0,r} + \hat{\mathbf{V}}_{\text{int},r}(t), \quad (2.37)$$

where

$$\hat{\mathbf{H}}_{0,r} := \hat{\mathbf{T}} + \hat{\mathbf{V}}_{0,r} \quad (2.38)$$

is the rotating-wave approximation of the molecular Hamiltonian, while $\hat{\mathbf{V}}_{0,r}$ and $\hat{\mathbf{V}}_{\text{int},r}(t)$, defined in Eqs. (2.22) and (2.23), represent the rotating-wave approximations of the molecular and interaction potentials. Application of the perturbation theory to the splitting (2.37) requires replacing $\hat{\mathbf{H}}_0$ with $\hat{\mathbf{H}}_{0,r}$ and $\hat{\mathbf{V}}_{\text{int}}$ with $\hat{\mathbf{V}}_{\text{int},r}(t)$ in Eq. (2.10), and yields the desired approximate evolution operator

$$\hat{\mathbf{U}}_{pr}(t, t_0) := \mathbf{W}(t)\hat{\mathbf{U}}_{pr}(t, t_0)\mathbf{W}(t_0)^{-1}, \quad (2.39)$$

$$\hat{\mathbf{U}}_{pr}(t, t_0) := \hat{\mathbf{U}}_{\hat{\mathbf{H}}_{0,r}}(t - t_0) - \frac{i}{\hbar} \int_{t_0}^t dt' \hat{\mathbf{U}}_{\hat{\mathbf{H}}_{0,r}}(t - t') \hat{\mathbf{V}}_{\text{int},r}(t') \hat{\mathbf{U}}_{\hat{\mathbf{H}}_{0,r}}(t' - t_0). \quad (2.40)$$

Alternatively, we can obtain this combination by applying the rotating-wave approximation

to the perturbation theory result (2.10). First, to move to the rotating frame, one multiplies the evolution operator $\hat{\mathbf{U}}_p(t, t_0)$ by $\mathbf{W}(t)^{-1}$ on the left and by $\mathbf{W}(t_0)$ on the right, to get

$$\begin{aligned} \mathbf{W}(t)^{-1} \hat{\mathbf{U}}_p(t, t_0) \mathbf{W}(t_0) &= \mathbf{W}(t)^{-1} \hat{\mathbf{U}}_0(t - t_0) \mathbf{W}(t_0) \\ &\quad - \frac{i}{\hbar} \int_{t_0}^t dt' \mathbf{W}(t)^{-1} \hat{\mathbf{U}}_0(t - t') \mathbf{W}(t') \hat{\mathbf{V}}_{\text{int}}(t') \mathbf{W}(t')^{-1} \hat{\mathbf{U}}_0(t' - t_0) \mathbf{W}(t_0) \\ &\approx \hat{\mathbf{U}}_{\hat{\mathbf{H}}_{0,r}}(t - t_0) - \frac{i}{\hbar} \int_{t_0}^t dt' \hat{\mathbf{U}}_{\hat{\mathbf{H}}_{0,r}}(t - t') \hat{\mathbf{V}}_{\text{int}}(t') \hat{\mathbf{U}}_{\hat{\mathbf{H}}_{0,r}}(t' - t_0), \end{aligned} \quad (2.41)$$

where in the first equality we use the definition (2.19) of $\hat{\mathbf{V}}_{\text{int}}(t')$ and in the second apply the rotating-wave approximation $\hat{\mathbf{U}}_0 \approx \hat{\mathbf{U}}_{\hat{\mathbf{H}}_{0,r}}$ and the relation

$$\mathbf{W}(t'')^{-1} \hat{\mathbf{U}}_{\hat{\mathbf{H}}_{0,r}}(t'' - t') \mathbf{W}(t') \approx \hat{\mathbf{U}}_{\hat{\mathbf{H}}_{0,r}}(t'' - t'), \quad (2.42)$$

which follows from the definition (2.13) of \mathbf{W} and the fact that $[\hat{\mathbf{H}}_{0,r}, \hat{\mathbf{\Pi}}] = 0$. [Note that the approximation $\hat{\mathbf{U}}_0 \approx \hat{\mathbf{U}}_{\hat{\mathbf{H}}_{0,r}}$, i.e., setting $\hat{\mathbf{H}}_0 \approx \hat{\mathbf{H}}_{0,r}$ simply removes the vibronic couplings between the ground state and either of the excited states. Equation (2.41) would be exact if $[\hat{\mathbf{H}}_0, \hat{\mathbf{\Pi}}] = 0$, i.e., if there were no vibronic couplings between the ground state and either of the excited states in the first place.] Now the time-dependent perturbation theory and rotating-wave approximation relation (2.40) follows by applying the rotating-wave approximation to $\hat{\mathbf{V}}_{\text{int}}(t)$ in Eq. (2.41).

2.2.3 Time-Dependent Perturbation Theory and Ultrashort-Pulse Approximation

This combination is obtained from the ultrashort-pulse approximation (2.35) by applying the time-dependent perturbation theory (2.10) to the evolution operator $\hat{\mathbf{U}}_{\hat{\mathbf{V}}_{e+\text{int}}(t)}(t_f, t_i)$. For the purposes of time-dependent perturbation theory, the effective Hamiltonian $\hat{\mathbf{V}}_{e+\text{int}}(t)$ is split into the unperturbed and perturbed parts as

$$\hat{\mathbf{V}}_{e+\text{int}}(t) \equiv \hat{\mathbf{I}} \mathbf{V}_e + \hat{\mathbf{V}}_{\text{int}}(t), \quad (2.43)$$

which gives the desired time-dependent perturbation theory and ultrashort-pulse approximation evolution operator

$$\hat{\mathbf{U}}_{pu}(t_f, t_i) := \hat{\mathbf{U}}_{\hat{\mathbf{H}}_{n+\text{ne}}}(t_f - t_m) \hat{\mathbf{U}}_{\hat{\mathbf{V}}_{e+\text{int}}(t), p}(t_f, t_i) \hat{\mathbf{U}}_{\hat{\mathbf{H}}_{n+\text{ne}}}(t_m - t_i), \quad (2.44)$$

$$\hat{\mathbf{U}}_{\hat{\mathbf{V}}_{e+\text{int}}(t), p}(t_f, t_i) := \hat{\mathbf{I}} \mathbf{U}_{\mathbf{V}_e}(t_f - t_i) - \frac{i}{\hbar} \int_{t_i}^{t_f} dt \mathbf{U}_{\mathbf{V}_e}(t_f - t) \hat{\mathbf{V}}_{\text{int}}(t) \mathbf{U}_{\mathbf{V}_e}(t - t_i). \quad (2.45)$$

To check that the same result (2.44) is obtained by applying the two approximations in the opposite order, we start from the evolution operator $\hat{\mathbf{U}}_p(t_f, t_i)$ given by Eq. (2.10) and uses the ultrashort-pulse approximation (2.35) four times, for $\Delta t \in \{t_f - t_m, t_m - t_i, t_f - t, t - t_i\}$.

Note that an alternative way to evaluate the combination of the time-dependent perturbation theory and ultrashort-pulse approximation, which is simpler and more accurate, has been derived and will be discussed in Chapter 4.

2.2.4 Rotating-Wave and Ultrashort-Pulse Approximations

This combination is obtained by applying the ultrashort-pulse approximation (2.35) to the evolution operator in the rotating-wave approximation (2.24). This requires splitting the approximate Hamiltonian $\hat{\mathbf{H}}_r(t)$ in the rotating frame into two parts, as

$$\hat{\mathbf{H}}_r(t) \equiv \hat{\mathbf{H}}_{n+ne,r} + \hat{\mathbf{V}}_{e+int,r}(t), \quad (2.46)$$

where the two components are

$$\hat{\mathbf{H}}_{n+ne,r} = \hat{\mathbf{H}}_{n+ne,r} = \hat{H}_n \mathbf{1} + \hat{\mathbf{V}}_{ne,r}, \quad (2.47)$$

$$\hat{\mathbf{V}}_{e+int,r}(t) = \hat{\mathbf{1}} \tilde{\mathbf{V}}_{e,r} + \hat{\mathbf{V}}_{int,r}(t) = \hat{\mathbf{1}} (\mathbf{V}_e - \hbar\omega_{\text{pulse}} \mathbf{\Pi}) + \hat{\mathbf{V}}_{int,r}(t), \quad (2.48)$$

and the simplifying relations (2.26), (2.27), and (2.29) have been used. Recall that $\hat{\mathbf{V}}_{ne,r}$ is given by $\hat{\mathbf{V}}_{ne}$, in which all matrix elements with the ground state have been deleted.

Applying the ultrashort-pulse approximation to the splitting (2.46) of $\hat{\mathbf{H}}_r(t)$ yields the desired evolution operator

$$\hat{\mathbf{U}}_{ru}(t_f, t_i) := \mathbf{W}(t_f) \hat{\mathbf{U}}_{ru}(t_f, t_i) \mathbf{W}(t_i)^{-1}, \quad (2.49)$$

$$\hat{\mathbf{U}}_{ru}(t_f, t_i) := \hat{\mathbf{U}}_{\hat{\mathbf{H}}_{n+ne,r}}(t_f - t_m) \hat{\mathbf{U}}_{\hat{\mathbf{V}}_{e+int,r}(t)}(t_f, t_i) \hat{\mathbf{U}}_{\hat{\mathbf{H}}_{n+ne,r}}(t_m - t_i). \quad (2.50)$$

To verify the commutativity of the two approximations, we apply the rotating wave (2.24) after the ultrashort-pulse approximation (2.35). In the rotating frame, the rotating-wave approximations of $\hat{\mathbf{H}}_{n+ne}$ and $\hat{\mathbf{V}}_{e+int}(t)$ [Eq. (2.34)] are $\hat{\mathbf{H}}_{n+ne,r}$ and $\hat{\mathbf{V}}_{e+int,r}(t)$, respectively, and the resulting evolution operator is

$$\hat{\mathbf{U}}_{ur}(t_f, t_i) = \hat{\mathbf{U}}_{\hat{\mathbf{H}}_{n+ne,r}}(t_f - t_m) \mathbf{W}(t_f) \hat{\mathbf{U}}_{\hat{\mathbf{V}}_{e+int,r}(t)}(t_f, t_i) \mathbf{W}(t_i)^{-1} \hat{\mathbf{U}}_{\hat{\mathbf{H}}_{n+ne,r}}(t_m - t_i), \quad (2.51)$$

which is easily seen to agree with Eq. (2.49) because the electronically blockdiagonal operators $\hat{\mathbf{U}}_{\hat{\mathbf{H}}_{n+ne,r}}(t')$ and $\mathbf{W}(t'')$ commute for any t' and t'' as a consequence of the relation:

$$[\hat{\mathbf{H}}_{n+ne,r}, \mathbf{W}(t'')] = 0. \quad (2.52)$$

2.2.5 Time-Dependent Perturbation Theory, Rotating-Wave, and Ultrashort-Pulse Approximations

This combination can be derived, e.g., by applying the time-dependent perturbation theory to the propagator $\hat{\mathbf{U}}_{\hat{\mathbf{V}}_{e+int,r}(t)}(t_f, t_i)$ in the expression (2.50) for the rotating wave and

ultrashort-pulse approximations propagator. This requires splitting the potential $\hat{\mathbf{V}}_{e+\text{int},r}(t)$ into a sum

$$\hat{\mathbf{V}}_{e+\text{int},r}(t) \equiv \hat{\mathbf{1}}\tilde{\mathbf{V}}_{e,r} + \hat{\mathbf{V}}_{\text{int},r}(t) \quad (2.53)$$

of the unperturbed part $\hat{\mathbf{1}}\tilde{\mathbf{V}}_{e,r}$ and the perturbation $\hat{\mathbf{V}}_{\text{int},r}(t)$, which gives

$$\hat{\mathbf{U}}_{\hat{\mathbf{V}}_{e+\text{int},r}(t),p}(t_f, t_i) = \hat{\mathbf{1}}\mathbf{U}_{\tilde{\mathbf{V}}_{e,r}}(t_f - t_i) - \frac{i}{\hbar} \int_{t_i}^{t_f} dt \mathbf{U}_{\tilde{\mathbf{V}}_{e,r}}(t_f - t) \hat{\mathbf{V}}_{\text{int},r}(t) \mathbf{U}_{\tilde{\mathbf{V}}_{e,r}}(t - t_i). \quad (2.54)$$

The desired time-dependent perturbation theory, rotating-wave, and ultrashort-pulse approximations evolution operator is then

$$\begin{aligned} \hat{\mathbf{U}}_{pru}(t_f, t_i) &:= \mathbf{W}(t_f) \hat{\mathbf{U}}_{pru}(t_f, t_i) \mathbf{W}(t_i)^{-1} \\ \hat{\mathbf{U}}_{pru}(t_f, t_i) &:= \hat{\mathbf{U}}_{\hat{\mathbf{H}}_{n+\text{ne},r}}(t_f - t_m) \hat{\mathbf{U}}_{\hat{\mathbf{V}}_{e+\text{int},r}(t),p}(t_f, t_i) \hat{\mathbf{U}}_{\hat{\mathbf{H}}_{n+\text{ne},r}}(t_m - t_i). \end{aligned} \quad (2.55)$$

2.3 Numerical Examples

The performance of our algorithms are tested using three different models: (1) a one-dimensional two-state harmonic system with linear transition-dipole couplings, (2) a one-dimensional three-state harmonic system with linear vibronic and transition-dipole couplings (further calculations and analysis of one-dimensional systems can be found in Appendix B), and (3) a three-dimensional three-state harmonic model of pyrazine with linear vibronic and quadratic transition-dipole couplings.

2.3.1 A Two-State Harmonic System with Linear Transition-Dipole Couplings

We perform the calculations using natural units (n.u.) that are defined such that the reduced Planck constant, the mass, the ground electronic state nuclear frequency, and the zeroth-order transition dipole are equal to unity, i.e., $\hbar = M = \omega_n = \mu_{12}(Q_0) = 1$, which leads to a unit ground state force constant ($k = 1$). In these units, dimensionless parameters simplify and are summarized in Table 2.2. First, we consider a one-dimensional two-state

Table 2.2 – Dimensionless parameters in natural units.

ϵ_c	ϵ_r	ϵ_p	ϵ_u
$ \mu'_{12}(Q_0) $	$\sqrt{\frac{2}{\pi}} \frac{E_0}{(\omega_e)_{12} \Delta t_{\text{pulse}}}$	$E_0 \Delta t_{\text{pulse}}$	$\frac{4\Delta Q_{21} \text{FWHM}}{(T_n)_2}$

undisplaced harmonic oscillator [see Fig. 2.2 (a)] with the minimum energy of the excited state S_2 being 100 n.u. The initial state is the vibrational ground state of the ground potential energy surface S_1 discretized on a linear grid composed of 4096 points from -80 to 80 n.u. We assume the resonant condition for the electric field meaning that the laser frequency is given by the energy difference of the two electronic states of interest at position Q_0 and its phase factor φ_{pulse} is set to 0. We propagate the wavefunction with electronic

Chapter 2. Approximations for the Molecule-Field Interaction

Table 2.3 – Dimensionless parameters (in natural units) for the one-dimensional two-state undisplaced harmonic system such that each basic approximation either works or breaks down.

	$\epsilon_c = \mu'_{12}(Q_0) $	ϵ_r	$\epsilon_p = E_0 \Delta t_{\text{pulse}}$	ϵ_u
working	0.1	$3 \cdot 10^{-3}$ ($E_0 = 0.1$ n.u.)	0.025	0 ($\Delta Q_{21} = 0$, $E_0 = 0.1$ n.u.)
failure	2.0	2 ($E_0 = 75$ n.u.)	0.25	0 ($\Delta Q_{21} = 0$, $E_0 = 20$ n.u.)

time step Δt_e of $2^{-11} \approx 5 \cdot 10^{-4}$ n.u. or nuclear time step Δt_n of $2^{-7} \approx 8 \cdot 10^{-3}$ n.u. using a fourth-order split-operator algorithm generated from the recursive method developed by Yoshida [67] and, when needed, combined with the sixth-order commutator-free Magnus expansion with five exponentials [76] and with the sixth-order Newton-Cotes-like formula known as Boole's rule [123]. Such choices for the grid and the time steps ensure that no error is coming from the grid spacing and propagation scheme.

We make a systematic study of the basic approximations. To do so, we set $\mu'_{12}(Q_0) = 0.1$, $\Delta t_{\text{pulse}} = 0.25$, and $E_0 = 0.1$ n.u., which ensure that all basic approximations are working and we make all of them to break down one at a time by changing a single parameter. Corresponding dimensionless parameters are given in Table 2.3. Laser pulse shapes and population dynamics for each of the basic approximations are depicted on Fig. 2.2 (b)-(f) when approximations work on the left side and when they break down on the right side.

On the left side of Fig. 2.2 (c)-(f), all the exact results are the same and each basic approximation is accurate and matches the exact value. We observe that due to the coupling with the electric field, the ground state population slightly decreases and the excited state starts to be populated. Moreover, we see fast and very small oscillations in the population dynamics which are due to the counter rotating term of the electric field and are completely smoothed-out when rotating-wave approximation is used.

As for the right side of Fig. 2.2 (c)-(f), we notice that for a huge electric field strength [panels (d) and (f)], population dynamics oscillates between zero and one. It corresponds to the time-dependent Rabi oscillations, $\Omega_R(t) = \mu_{12}(Q_0)E_0\mathcal{E}(t)/\hbar$, which are fast and large around the maximum of the pulse and long and small in the tails.

Besides, we see that Condon approximation, rotating-wave approximation, and time-dependent perturbation theory break down according to the value of the dimensionless parameters. The rotating-wave approximation fails due to the counter-rotating term which becomes important with large electric field strength but not taken into account within this approximation. As for the ultrashort-pulse approximation, it should be valid because we have $\epsilon_u = 0$. Indeed, we can show that the combination of ultrashort-pulse and Condon

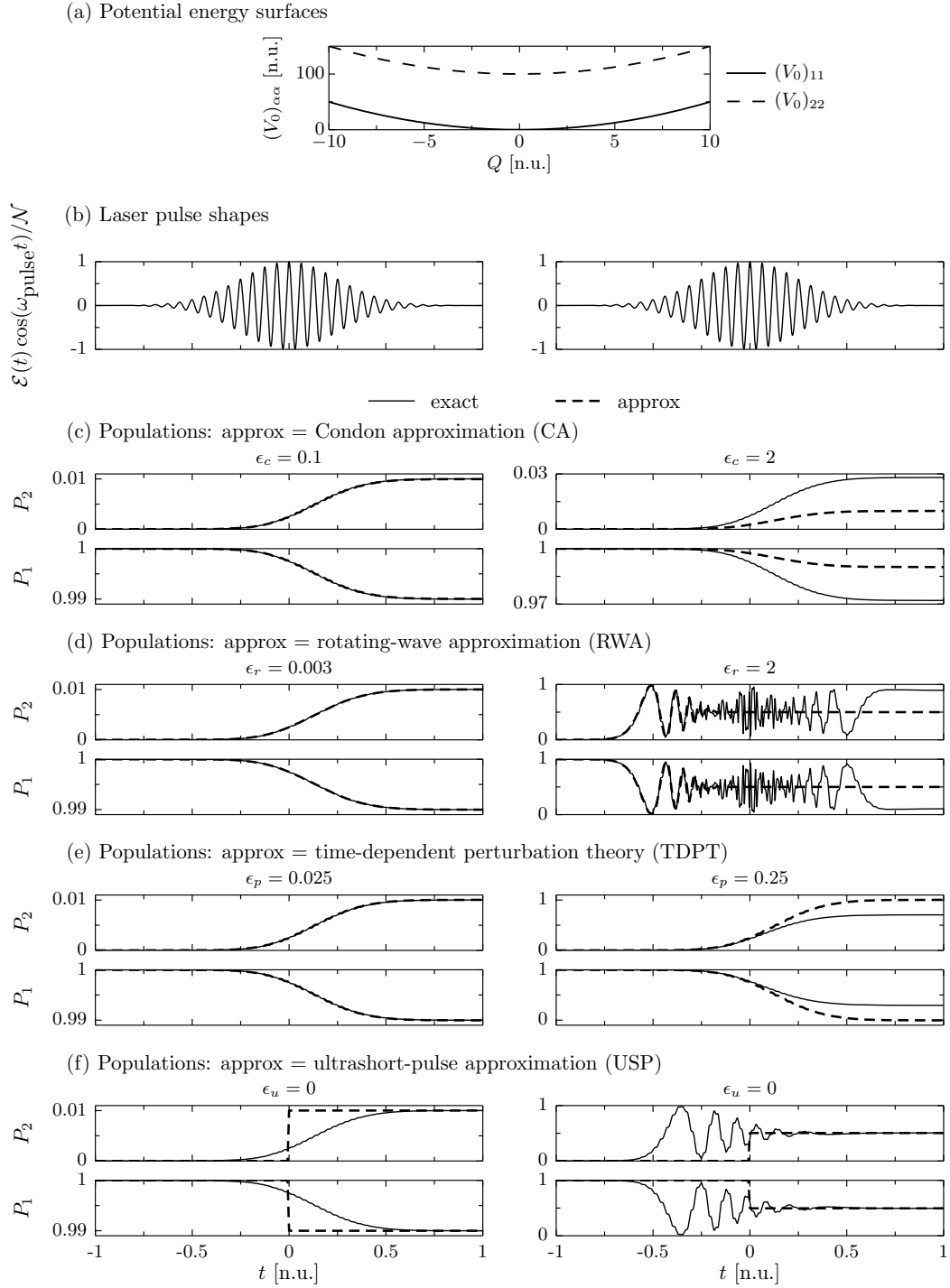


Figure 2.2 – Several examples of population dynamics for the four basic approximations (c)-(f) together with the laser pulse shapes (b) applied to a one-dimensional two-state undisplaced harmonic system (a). The left panels show the agreement between approximate and exact quantum calculations. A single parameter has been changed in each of the right panels which causes the breakdown of the corresponding approximation with respect to its exact counterpart.

approximations is equal to the Condon approximation:

$$\begin{aligned}
 \hat{U}_c(t_f, t_i) &:= \mathcal{T} \exp \left[-\frac{i}{\hbar} \int_{t_i}^{t_f} \hat{\mathbf{H}}_c(t) dt \right] \\
 &= \hat{U}_{\hat{\mathbf{H}}_{n+ne}}(t_f - t_i) \mathcal{T} \exp \left[-\frac{i}{\hbar} \int_{t_i}^{t_f} \mathbf{V}_{e+int,c}(t) dt \right] \\
 &= \hat{U}_{\hat{\mathbf{H}}_{n+ne}}(t_f - t_m) \mathbf{U}_{\mathbf{V}_{e+int,c}(t)}(t_f, t_i) \hat{U}_{\hat{\mathbf{H}}_{n+ne}}(t_m - t_i) \\
 &=: \hat{U}_{uc}(t_f, t_i),
 \end{aligned}$$

where in the first step, we use the fact that for uncoupled potentials where excited state surfaces differ from the ground state only by vertical shifts: $\hat{\mathbf{V}}_{ne} = 0$, the relation $[\hat{\mathbf{H}}_{n+ne}, \hat{\mathbf{I}}_{\mathbf{V}_{e+int,c}}(t)] = 0$ holds. Therefore, it could slightly break down if the Condon approximation is not perfectly valid.

Another way to quantify the accuracy of a given method is by computing the fidelity between the exact and approximate wavefunctions that is defined as

$$F(t) = \left| \frac{\langle \psi_{\text{exact}}(t) | \psi_{\text{approx}}(t) \rangle}{\| \psi_{\text{exact}}(t) \| \| \psi_{\text{approx}}(t) \|} \right|^2. \quad (2.56)$$

We depicted the fidelity of the four basic approximations on Fig. 2.3 when the approximations work and break down on the left and right side, respectively. We might say that the Condon approximation does not break down because the fidelity decreases only to 0.98. However, it does fail and the reason for having such a huge fidelity is that the excitation is very small so the fidelity is mostly determined by the ground state wavefunctions that are both almost the same. As for the break down of the time-dependent perturbation theory, we observe that the fidelity decays to 0.95. As this value is still close to unity, it means that a pretty good agreement, up to a scaling factor, exists between the exact and time-dependent perturbation theory wavefunctions, for all time. Concerning the ultrashort-pulse approximation, the working example shows that the fidelity is slowly and smoothly decreasing until that the molecule-field interaction is included within this approximation ($t = 0$). As for its break down counterpart, a smooth decrease is followed by huge oscillations due to the Rabi oscillations. Then, both examples have very fast oscillations due to a phase shift between the excited state wavepackets of the exact quantum calculation and the ultrashort-pulse approximation. However, at the end of the simulation, the phase is recovered and both fidelities tend to unity which means that the ultrashort-pulse approximation perfectly matches the exact quantum calculation.

2.3.2 A Three-State Harmonic System with Linear Vibronic and Transition-Dipole Couplings

We consider a one-dimensional three-state displaced harmonic oscillator with different force constants, linear transition-dipole couplings between states S_1 and S_2 , and linear vibronic coupling between states S_2 and S_3 [see Fig. 2.4 (a)]. The displacements and force constants

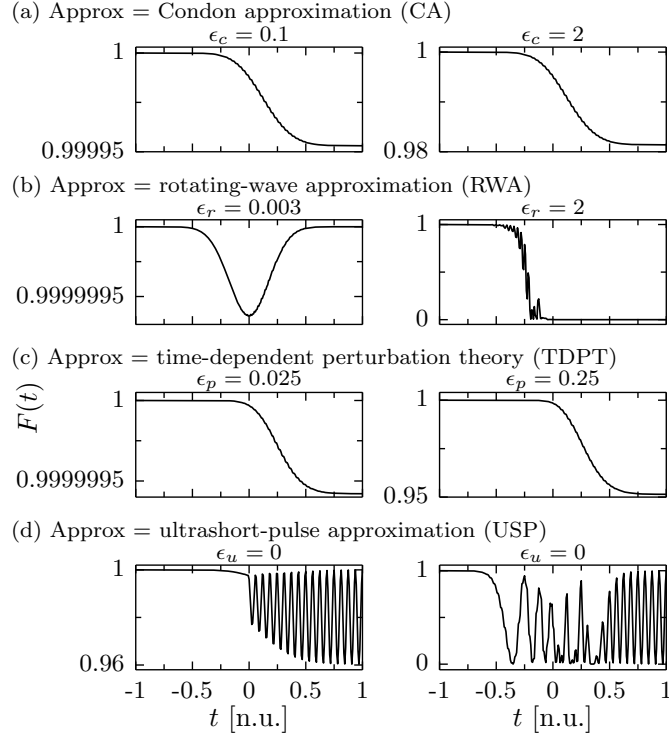


Figure 2.3 – Several examples of fidelity of the four basic approximations applied to a one-dimensional two-state undisplaced harmonic model. Same set of parameters as in Fig. 2.2 for left and right panels.

are $\Delta Q_{21} = 1$, $\Delta Q_{31} = 11$, $k_2 = 1.1k$ and $k_3 = 1.5k$, respectively. The minimum energy of the electronic state S_3 is 75 n.u. and the strength of the linear vibronic coupling is $a_{23} = 0.3$ n.u. $[(V_0)_{23}(Q) = a_{23}(Q - Q_0)]$. Computational details are the same as the one given in Sec. 2.3.1 except that the grid is now made of 8192 points from -40 to 176 n.u.

As before, we make a systematic study of the basic approximations, using $\Delta t_{\text{pulse}} = 0.1875$ and $E_0 = 0.075$ n.u. (see Table 2.4 for the dimensionless parameters). Fig. 2.4 (b)-(f) depicts laser pulse shapes and population dynamics for each of the basic approximations.

In addition to what we already observe on Fig. 2.2, the left side of Fig. 2.4 shows that due to

Table 2.4 – Dimensionless parameters (in natural units) for the one-dimensional three-state displaced harmonic system with different force constants such that each basic approximation either works or breaks down.

	$\epsilon_c = \mu'_{12}(Q_0) $	ϵ_r	$\epsilon_p = E_0 \Delta t_{\text{pulse}}$	ϵ_u
working	0.1	$3 \cdot 10^{-3}$ ($E_0 = 0.075$ n.u.)	0.014	0.3 ($\Delta Q_{21} = 1$ n.u.)
failure	2.0	2 ($E_0 = 50$ n.u.)	0.14	1.2 ($\Delta Q_{21} = 4$ n.u.)

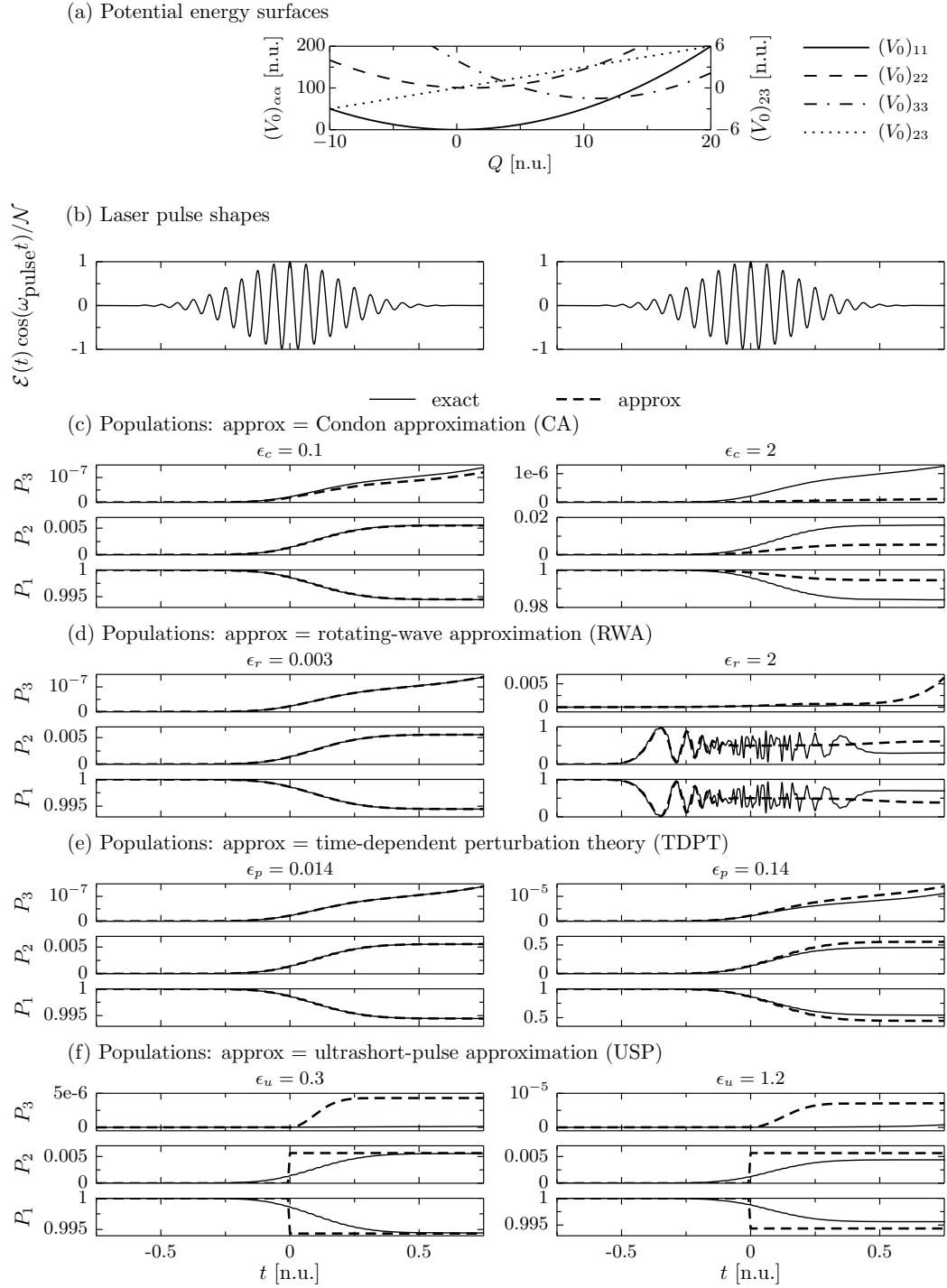


Figure 2.4 – Several examples of population dynamics following the excitation of a one-dimensional three-state displaced harmonic system with different force constants. See Fig. 2.2 for more details.

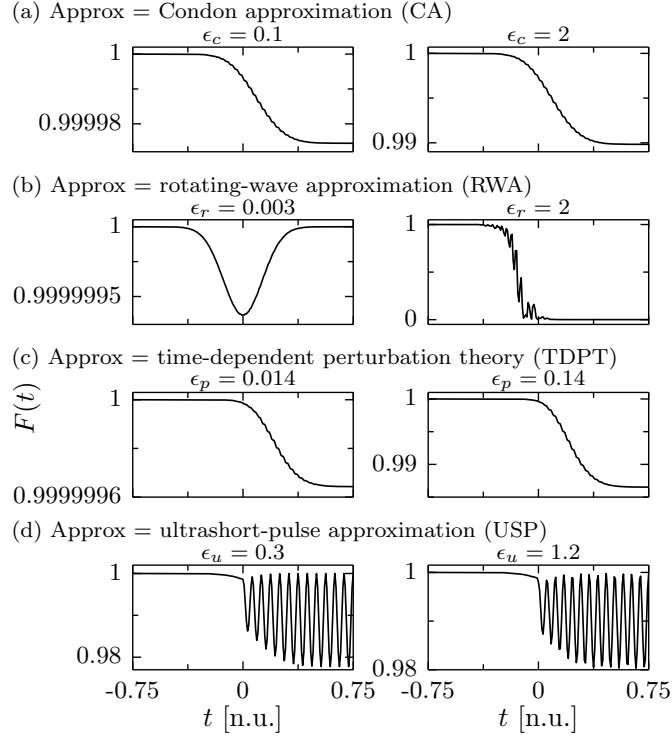


Figure 2.5 – Several examples of fidelity of the four basic approximations applied to a one-dimensional three-state displaced harmonic system with different force constants. Same set of parameters as in Fig. 2.4 for left and right panels.

the vibronic couplings between excited states S_2 and S_3 , as soon as S_2 is getting populated, there is a population transfer to S_3 . Moreover, the ultrashort-pulse approximation is not able to reproduce the exact population on S_3 because the vibronic couplings are not treated during the interaction with the pulse. However, the population on S_3 is very small, thus, we can still assume that the ultrashort-pulse approximation is doing very well. As for the break down example of the ultrashort-pulse approximation, we shift the electronic state S_2 by four natural units with respect to the ground electronic state instead of a single unit of displacement. It leads to a much bigger curvature of the potential energy surface which makes the wavepacket to move faster (the nuclear period of motion is conserved). Therefore, the nuclear motion is not slow enough anymore during the interaction with the pulse, and the approximation breaks down.

As in the two-state case, fidelity is computed (using Eq. 2.56) and is depicted in Fig. 2.5 for each of the basic approximations. As for the break down of the ultrashort-pulse approximation, as the electric field strength is relatively small, the huge oscillations that were present in the two-state case before time zero have disappeared. Nevertheless, we observe fast oscillations due to a phase shift between excited state wavefunctions after time $t = 0$. Moreover, one might see that at the end of the simulation, the fidelity does not go back to one anymore because the phase is not totally recovered. However, it tends to a value very close to one because the ground state depopulation is very small, hence fidelity is mostly determined by the overlap of the ground state wavefunctions.

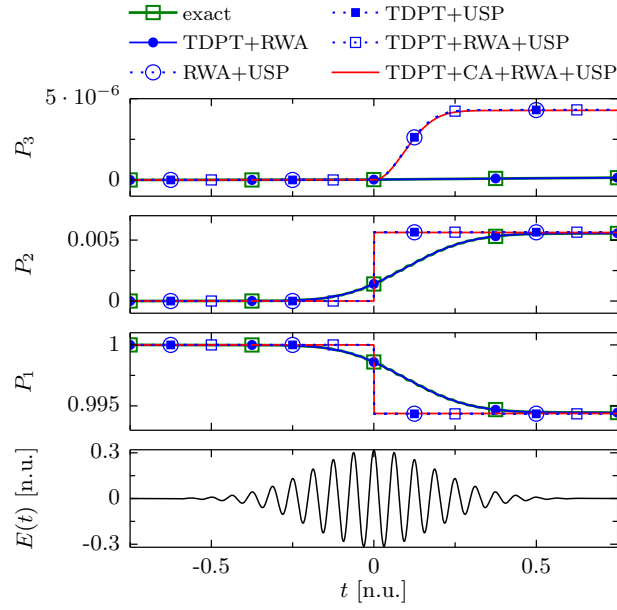


Figure 2.6 – Laser pulse shape and population dynamics obtained with the exact quantum calculation and with several combinations of the basic approximations applied to a one-dimensional three-state displaced harmonic system with different force constants.

Then, we test several combinations of the basic approximations. Fig. 2.6 displays laser pulse shape and population dynamics obtained with the exact quantum calculation and with several approximate methods. We see that the ground and first excited state populations are almost perfectly reproduced. However, as for the combinations including the ultrashort-pulse approximation, they are not able to reproduce the second excited state population. But, the population on S_3 is much smaller than the one on S_2 , therefore we can still assume that those combinations that involved the ultrashort-pulse approximation are working very well.

Finally, the CPU time and speedup of several approximations with respect to the exact propagation is investigated and summarized in Table 2.5. We assume a convergence within the error of the approximation, therefore each method is propagated with its own time step(s). We refer the reader to Appendix C for more informations about the procedure to determine the required time steps and to compute the CPU cost and speedup. Note that we do an average over 10 simulations.

Since the vibronic couplings are not so important in the harmonic system, the nuclear and electronic time scales are quite different. Therefore, the speedup of a method which requires a nuclear time step should be very important. Indeed, it can go up to 83 for the most approximate method, i.e., the combination of time-dependent perturbation theory, and the Condon, rotating wave, and ultrashort-pulse approximations.

2.3. Numerical Examples

Table 2.5 – CPU time and speedup with respect to the exact propagation for several approximate methods averaged over 10 simulations using a single core of a Six-Core AMD Opteron 2427 processor chip. Δt_{ME} and Δt_{NI} refer to the time step needed to perform Magnus expansion and numerical integration, respectively.

method	Δt [n.u.]	$\Delta t_{\text{ME/NI}}$ [n.u.]	CPU time [s]	speedup
exact	0.0046875	-	99.6 \pm 0.6	“1”
CA	0.0075	-	65.6 \pm 0.5	1.5 \pm 0.01
RWA	0.06	-	9.04 \pm 0.02	11 \pm 0.07
TDPT	0.0234375	$b_j \Delta t$	37.8 \pm 0.08	2.6 \pm 0.02
USP	0.125	0.015625	68.1 \pm 0.6	1.4 \pm 0.02
RWA+USP	0.125	0.25	5.08 \pm 0.03	20 \pm 0.2
TDPT+USP	0.15	0.025	9.57 \pm 0.05	10 \pm 0.08
TDPT+RWA	0.0625	$b_j \Delta t$	11.2 \pm 0.06	8.9 \pm 0.07
TDPT+RWA+USP	0.15	0.3	1.53 \pm 0.002	65 \pm 0.4
TDPT+CA+RWA+USP	0.15	0.3	1.20 \pm 0.003	83 \pm 0.5

2.3.3 A Pump-Probe Experiment in Pyrazine

We focus on pyrazine, a molecule that has been extensively studied and for which only certain of the 24 vibrational modes are proved to be important for short time dynamics [124]. Therefore, we consider the three-dimensional three-state vibronic coupling model of pyrazine composed of ground S_0 and excited S_1 [$^1B_{3u}(n\pi^*)$] and S_2 [$^1B_{2u}(\pi\pi^*)$] electronic states. The excited states represent a classic example of vibronic coupling in aromatic system. Note that in what follows, we switch from natural units to atomic units (a.u.). We base our model from ab initio complete active space self consistent field calculation which is described in Refs. [125] and [126]. The transition dipole moment is expanded up to second-order and we set the zeroth-order terms to $(\vec{\mu}(Q_0))_{01} = (0.360, 0, 0)$ and $(\vec{\mu}(Q_0))_{02} = (0, 0.617, 0) e a_0$. The initial state is the ground vibrational state of the electronic ground state discretized, for each of the three modes, on a grid composed of 64 points equally spaced between -8 and 8 a_0 . We test several approximations by simulating a pump-probe experiment using two perpendicularly polarized Gaussian pulses (FWHM = 20 fs). Other laser pulses parameters are given in Table 2.6. We perform the propagation using a fourth-order split-operator scheme [67] with electronic and nuclear time step of 1 and 4 \hbar/E_h , respectively. As for the ultrashort-pulse approximation and the combination of the Condon and ultrashort-pulse approximations, we use a sixth-order commutator-free Magnus expansion [76] ($\Delta t = 8 \hbar/E_h$) and for the combinations involving the rotating-wave, ultrashort-pulse, and Condon approximations, we use the fourth-order version ($\Delta t = 32 \hbar/E_h$). We refer the reader to Appendix D for the error analysis which reflects our actual choice of grid, algorithms, and time steps.

Chapter 2. Approximations for the Molecule-Field Interaction

Table 2.6 – Pump and probe laser pulse parameters in atomic units.

	$\vec{\epsilon}$	$E_0 [E_h^2/ea_0\hbar]$	$t_m [\hbar/E_h]$	$\omega_{\text{pulse}} [E_h/\hbar]$	φ_{pulse}
pump	(0,1,0)	4	0	0.179704	0
probe	(1,0,0)	10	4878	0.139090	0

Population dynamics under the influence of the laser pulses for several level of approximations is depicted in Fig. 2.7. During the interaction with the pump laser pulse, the population is transferred from S_0 to S_2 and S_1 gets populated almost instantaneously due to the vibronic couplings. Then, the probe pulse populates back S_0 from S_1 . The Condon and rotating-wave approximations, as well as the combination of these two approximations perfectly reproduce the exact dynamics. However, it is not the case for the ultrashort-pulse approximation and its combinations with the Condon and rotating-wave approximations because a full-width at half-maximum of 20 fs cannot be considered as ultrashort anymore. All the combinations that involved the ultrashort-pulse approximation give the same result, therefore, the break down is due to the ultrashort-pulse approximation itself. Further analysis of the pump-probe simulation can be found in Appendix D.

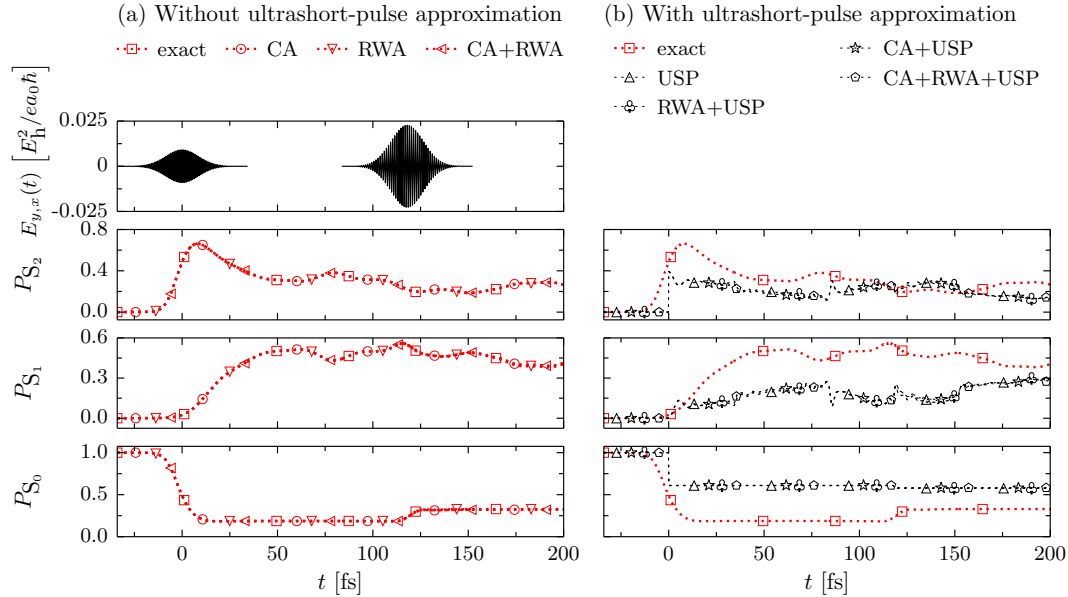


Figure 2.7 – Laser pulse shape and population dynamics obtained with the exact quantum calculation and with several level of approximations during the interaction with pump and probe laser pulses applied to a three-dimensional three-state vibronic coupling model of pyrazine.

In addition, the CPU time and speedup with respect to the exact propagation are given in Table 2.7 for the approximations used in Fig. 2.7. Note that due to the high cost of the three-dimensional calculations, the analysis of CPU time simplifies compared to Sec. 2.3.2. Using the Condon approximation does almost not produce any speedup. However, using the rotating-wave approximation or the combination of Condon and rotating-wave approximation accelerate the calculations by a factor of 3 without losing almost any

2.3. Numerical Examples

accuracy. Concerning the ultrashort-pulse approximation and its combinations, one can achieve a speedup up to 7. This is quite impressive because of the strong nonadiabatic nature of the system, i.e., the nuclear time scale approaches the electronic time scale. However, such methods, even if very powerful, are not able to reproduce the exact quantum dynamics.

Table 2.7 – CPU time and speedup with respect to the exact propagation for several approximate methods using a single core of a Six-Core AMD Opteron 2427 processor chip.

method	CPU time [h]	speedup
exact	16.0	“1”
CA	15.8	1.0
RWA	4.67	3.4
CA+RWA	4.55	3.5
USP	6.47	2.5
CA+USP	4.48	3.6
RWA+USP	2.31	7.0
CA+RWA+USP	2.19	7.3

3 Split-Operator and Magnus Integrators of Arbitrary Order

The time-dependent Schrödinger equation has to be converted, independently of the number of approximations included, into a numerically tractable problem; and a numerical algorithm is required to propagate the initial wavefunction in time. In this chapter, we develop geometric integrators of arbitrary order of accuracy in the time step, for which time-reversal symmetry, unitarity, and symplectic structure are preserved. The general split-operator/Magnus integrator algorithm is such an integrator and is the one we use. After implementing this geometric integrator for the exact nonadiabatic quantum dynamics of a molecule interacting with a time-dependent electromagnetic field, we derive and implement such geometric integrators for the time-dependent perturbation theory, the Condon, rotating-wave, and ultrashort-pulse approximations, as well as every possible combination thereof. Using a one-dimensional model system, we show that these integrators exactly preserve the geometric invariants, and achieve an arbitrary prescribed order of accuracy in the time step and an exponential convergence in the grid spacing. In addition, we demonstrate the importance of the use of the high-order geometric integrators. The results of this chapter can be found in Ref. [127].

3.1 General Definition of Split-Operator Method and Magnus Expansion

3.1.1 Split-Operator Method

Assuming a time-independent Hamiltonian that can be split into two parts $\hat{\mathbf{A}}$ and $\hat{\mathbf{B}}$, which can be identified in our molecular Hamiltonian definition $\hat{\mathbf{H}}_0$ [see Eq. (1.3)] to $\hat{\mathbf{T}}$ and $\hat{\mathbf{V}}_0$, respectively, a single split-operator (SO) step of order $M_{\text{SO}} + 1$ and composed on N_{SO}

splitting steps reads

$$\hat{\mathbf{U}}_{\hat{\mathbf{A}}+\hat{\mathbf{B}}}(\Delta t) = \hat{\mathbf{U}}_{\hat{\mathbf{A}}+\hat{\mathbf{B}}}^{\text{SO}}(\Delta t) + \mathcal{O}(\Delta t^{M_{\text{SO}}+1}), \quad (3.1)$$

$$\hat{\mathbf{U}}_{\hat{\mathbf{A}}+\hat{\mathbf{B}}}^{\text{SO}}(\Delta t) := \mathcal{T} \prod_{j=1}^{N_{\text{SO}}} \hat{\mathbf{U}}_{\hat{\mathbf{B}}}(b_j \Delta t) \hat{\mathbf{U}}_{\hat{\mathbf{A}}}(a_j \Delta t), \quad (3.2)$$

where the a_j s and b_j s are a set of predefined coefficients with the property $\sum_{j=1}^{N_{\text{SO}}} a_j = \sum_{j=1}^{N_{\text{SO}}} b_j = 1$ that ensures the proper convergence of the algorithm. For long time propagation, t_0 to t , the full evolution needs to be decomposed into a number of small time steps Δt . Therefore, we define a concatenated split-operator (CSO) of order M_{SO} , which is as follows

$$\hat{\mathbf{U}}_{\hat{\mathbf{A}}+\hat{\mathbf{B}}}(t - t_0) = \hat{\mathbf{U}}_{\hat{\mathbf{A}}+\hat{\mathbf{B}}}^{\text{CSO}}(t - t_0) + \mathcal{O}(\Delta t^{M_{\text{SO}}}), \quad (3.3)$$

$$\hat{\mathbf{U}}_{\hat{\mathbf{A}}+\hat{\mathbf{B}}}^{\text{CSO}}(t - t_0) := \hat{\mathbf{U}}_{\hat{\mathbf{A}}+\hat{\mathbf{B}}}^{\text{SO}}(\Delta t)^{S_{\text{SO}}}, \quad (3.4)$$

where the number of split-operator steps is given by $S_{\text{SO}} := (t - t_0)/\Delta t$.

If we now assume that the operator $\hat{\mathbf{B}}$ is time-dependent, $\hat{\mathbf{B}} \rightarrow \hat{\mathbf{B}}(t)$, which can be identified in our case to the total time-dependent potential $\hat{\mathbf{V}}(t)$, then, the single split-operator step slightly changes such that the time-dependence of the operator is taken into account and reads [70]

$$\hat{\mathbf{U}}_{\hat{\mathbf{A}}+\hat{\mathbf{B}}(t')}(t + \Delta t, t) = \hat{\mathbf{U}}_{\hat{\mathbf{A}}+\hat{\mathbf{B}}(t')}^{\text{SO}}(t + \Delta t, t) + \mathcal{O}(\Delta t^{M_{\text{SO}}+1}), \quad (3.5)$$

$$\hat{\mathbf{U}}_{\hat{\mathbf{A}}+\hat{\mathbf{B}}(t')}^{\text{SO}}(t + \Delta t, t) := \mathcal{T} \prod_{j=1}^{N_{\text{SO}}} \hat{\mathbf{U}}_{\hat{\mathbf{B}}(t_j)}(b_j \Delta t) \hat{\mathbf{U}}_{\hat{\mathbf{A}}}(a_j \Delta t), \quad (3.6)$$

where $t_j = t + c_j \Delta t$, and $c_j = \sum_{k=1}^j a_k$ with $1 \leq j \leq N_{\text{SO}}$. A third coefficient, c_j , appears in order to make sure that time t_j at which $\hat{\mathbf{B}}(t_j)$ is evaluated ensures the proper convergence of the algorithm. As before, for long time propagation, t_0 to t , S_{SO} small steps of length Δt are needed and the concatenated version is given by

$$\hat{\mathbf{U}}_{\hat{\mathbf{A}}+\hat{\mathbf{B}}(t')}(t, t_0) = \hat{\mathbf{U}}_{\hat{\mathbf{A}}+\hat{\mathbf{B}}(t')}^{\text{CSO}}(t, t_0) + \mathcal{O}(\Delta t^{M_{\text{SO}}}), \quad (3.7)$$

$$\hat{\mathbf{U}}_{\hat{\mathbf{A}}+\hat{\mathbf{B}}(t')}^{\text{CSO}}(t, t_0) := \mathcal{T} \prod_{k=1}^{S_{\text{SO}}} \hat{\mathbf{U}}_{\hat{\mathbf{A}}+\hat{\mathbf{B}}(t')}^{\text{SO}}(t_k, t_{k-1}), \quad (3.8)$$

where $t_k := t_0 + k \Delta t$ for $k \in \{1, \dots, S_{\text{SO}}\}$ is the final time of a given split-operator step.

Amongst all the possibility of splitting, the probably best known is the second-order algorithm [46] which is as widespread as Verlet algorithm for classical molecular dynamics [128] and has already been referred to in the introduction [see Eqs. (1.25)-(1.28)]. Appendix E illustrates how the choice of the set of c coefficients can affect the order of convergence of the second-order algorithm. Another well-known algorithm is the one developed by Yoshida [67] which is based on a symmetric repetition of the second-order splitting such that any

3.1. General Definition of Split-Operator Method and Magnus Expansion

even order M_{SO} can be obtained. The fourth-order version reads after some simplifications

$$\begin{aligned} \hat{\mathbf{U}}_{\hat{\mathbf{A}}+\hat{\mathbf{B}}}^{\text{SO } 4^{\text{th}}}(\Delta t) = & \hat{\mathbf{U}}_{\hat{\mathbf{A}}}(a_1\Delta t)\hat{\mathbf{U}}_{\hat{\mathbf{B}}(t+c_3\Delta t)}(b_1\Delta t)\hat{\mathbf{U}}_{\hat{\mathbf{A}}}(a_2\Delta t)\hat{\mathbf{U}}_{\hat{\mathbf{B}}(t+c_2\Delta t)}(b_2\Delta t) \\ & \hat{\mathbf{U}}_{\hat{\mathbf{A}}}(a_2\Delta t)\hat{\mathbf{U}}_{\hat{\mathbf{B}}(t+c_1\Delta t)}(b_1\Delta t)\hat{\mathbf{U}}_{\hat{\mathbf{A}}}(a_1\Delta t), \end{aligned} \quad (3.9)$$

where $a_1 = \frac{1}{2(2-z)}$, $a_2 = (1-z)a_1$, $b_1 = \frac{1}{2-z}$, $b_2 = -zb_1$, and $z = 2^{1/3}$.

Assuming that the split-operator algorithm starts with $\hat{\mathbf{U}}_{\hat{\mathbf{B}}(t)}(\Delta t)$ propagator, diagonal in the coordinate representation, and follows with $\hat{\mathbf{U}}_{\hat{\mathbf{A}}}(\Delta t)$ propagator, diagonal in the momentum representation, the numerical procedure is as follows: First, propagation of the molecular state $|\psi(t)\rangle$ is performed in coordinate space

$$\langle Q|\hat{\mathbf{U}}_{\hat{\mathbf{B}}(t')}(t)\psi(t)\rangle = \mathbf{U}_{\mathbf{B}(Q,t')}(t)\langle Q|\psi(t)\rangle = \langle Q|\psi'(t)\rangle.$$

Next, switching from coordinate to momentum representation is performed using Fourier transforms, which are numerically computed using the fast Fourier transform algorithm [118, 119], in order to take advantage of the simple form of $\hat{\mathbf{U}}_{\hat{\mathbf{A}}}(\Delta t)$ in that representation. Then, the quantum state $|\psi'(t)\rangle$ is propagated as

$$\langle P|\hat{\mathbf{U}}_{\hat{\mathbf{A}}}(t)\psi'(t)\rangle = \mathbf{U}_{\mathbf{A}(P)}(t)\langle P|\psi'(t)\rangle.$$

Finally, inverse Fourier transform is used to go back to coordinate representation and the procedure is repeated for the given number of splitting steps N_{SO} present in the single split-operator step. This procedure is then repeated S_{SO} times in order to propagate the initial state from time t_0 to t .

3.1.2 Magnus Expansion

Assuming a time-dependent operator $\hat{\mathbf{A}}(t)$ and a single short enough time step Δt , the Magnus propagator, based on the Magnus expansion (ME) $\hat{\mathbf{\Omega}}_{\hat{\mathbf{A}}(t)}$ reads

$$\hat{\mathbf{U}}_{\hat{\mathbf{A}}(t')}(t + \Delta t, t) =: e^{\hat{\mathbf{\Omega}}_{\hat{\mathbf{A}}(t')}(t + \Delta t, t)}, \quad (3.10)$$

where the Magnus expansion is defined as

$$\hat{\mathbf{\Omega}}_{\hat{\mathbf{A}}(t')}(t + \Delta t, t) = \sum_{j=1}^{\infty} \hat{\mathbf{\Omega}}_{\hat{\mathbf{A}}(t'),j}. \quad (3.11)$$

It exists a sufficient (but not necessary) condition for convergence which reads

$$\int_t^{t+\Delta t} dt' \|\hat{\mathbf{A}}(t')\| < \pi\hbar.$$

In our case, it is always fulfilled for short enough times because $\hat{\mathbf{A}}(t)$ is always part of the total time-dependent potential $\hat{\mathbf{V}}(t)$ and never contains the unbounded nuclear kinetic

operator $\hat{\mathbf{T}}$.

We shall use specific algorithms that approximate $\hat{\Omega}_{\hat{\mathbf{A}}(t')}(t + \Delta t, t)$ to some order M_{ME} in Δt . Magnus expansion for a single step of order $M_{\text{ME}} + 1$, using a short enough time step Δt , reads

$$\hat{\Omega}_{\hat{\mathbf{A}}(t')}(t + \Delta t, t) = \hat{\Omega}_{\hat{\mathbf{A}}(t')}^{\text{ME}}(t + \Delta t, t) + \mathcal{O}(\Delta t^{M_{\text{ME}}+1}), \quad (3.12)$$

hence, the corresponding Magnus propagator is given by

$$\hat{\mathbf{U}}_{\hat{\mathbf{A}}(t')}(t + \Delta t, t) = e^{\hat{\Omega}_{\hat{\mathbf{A}}(t')}^{\text{ME}}(t + \Delta t, t)} + \mathcal{O}(\Delta t^{M_{\text{ME}}+1}). \quad (3.13)$$

Since the Magnus series only converges locally, to guarantee convergence for long propagation times, t_0 to t , the time interval (t_0, t) has to be divided into S_{ME} subintervals of length $\Delta t := (t - t_0)/S_{\text{ME}}$ such that the Magnus series converges in each subinterval. The exact evolution operator is approximated numerically as

$$\hat{\mathbf{U}}_{\hat{\mathbf{A}}(t')}(t, t_0) = \hat{\mathbf{U}}_{\hat{\mathbf{A}}(t')}^{\text{ME}}(t, t_0) + \mathcal{O}(\Delta t^{M_{\text{ME}}}), \quad (3.14)$$

where the numerical evolution operator based on Magnus expansion is the concatenation of the elementary steps (3.13)

$$\hat{\mathbf{U}}_{\hat{\mathbf{A}}(t')}^{\text{ME}}(t, t_0) := \mathcal{T} \prod_{k=1}^{S_{\text{ME}}} e^{\hat{\Omega}_{\hat{\mathbf{A}}(t')}^{\text{ME}}(t_k, t_{k-1})}, \quad (3.15)$$

with $t_k := t_0 + k \Delta t$ for $k \in \{1, \dots, S_{\text{ME}}\}$ defined as the final time of a given step.

Amongst all the possible algorithms, we should cite the second-order scheme [74] for which the Magnus expansion of a single step is given by

$$\hat{\Omega}_{\hat{\mathbf{A}}(t')}^{\text{ME } 2^{\text{nd}}}(t + \Delta t, t) = -\frac{i}{\hbar} \Delta t \hat{\mathbf{A}}(t + \Delta t/2). \quad (3.16)$$

As for higher-order schemes, the Magnus expansion includes computation of commutators. As it is computationally expensive, we decide to use propagators based on commutator-free Magnus expansion (CFME) [76]. They are derived from propagators based on usual Magnus expansion and are shown to be completely equivalent [76]. They lead to an evolution operator that is a product of exponential terms from which each of them evaluates linear combinations of $\hat{\mathbf{A}}(t_i)$. An example of a single step numerical fourth-order evolution operator based on commutator-free Magnus expansion is given by

$$e^{\hat{\Omega}_{\hat{\mathbf{A}}(t')}^{\text{CFME } 4^{\text{th}}}(t + \Delta t, t)} = e^{-\frac{i}{\hbar} \Delta t (\hat{\mathbf{A}}^0 + \hat{\mathbf{A}}^1)} e^{-\frac{i}{\hbar} \Delta t (\hat{\mathbf{A}}^0 - \hat{\mathbf{A}}^1)}, \quad (3.17)$$

where $\hat{\mathbf{A}}^0 = \frac{1}{4}(\hat{\mathbf{A}}_+ + \hat{\mathbf{A}}_-)$, $\hat{\mathbf{A}}^1 = \frac{\sqrt{3}}{6}(\hat{\mathbf{A}}_+ - \hat{\mathbf{A}}_-)$, and $\hat{\mathbf{A}}_{\pm} = \hat{\mathbf{A}}(t + c_{\pm} \Delta t)$ with $c_{\pm} = \frac{1}{2} \pm \frac{\sqrt{3}}{6}$.

It is interesting to note that, as $\hat{\mathbf{A}}(t)$ is only part of the total time-dependent potential

3.2. Numerical Implementation of the Exact Propagation

$\hat{\mathbf{V}}(t)$, it is obviously independent of nuclear momenta. Therefore, Magnus propagation is always performed in coordinate representation, i.e., fast Fourier transforms that switch between coordinate and momentum representations are avoided.

3.1.3 Combination of Split-Operator Method with Magnus Expansion

The combined split-operator/Magnus expansion evolution operator, which will be used for the ultrashort-pulse approximation and several combinations that include it, reads

$$\hat{\mathbf{U}}_{\hat{\mathbf{A}}+\hat{\mathbf{B}}(t')}^{\text{SO/ME}}(t+\Delta t, t) := \mathcal{T} \prod_{j=1}^{N_{\text{SO}}} \hat{\mathbf{U}}_{\hat{\mathbf{B}}(t'_j)}^{\text{ME}}(t_j, t_{j-1}) \hat{\mathbf{U}}_{\hat{\mathbf{A}}}(a_j \Delta t), \quad (3.18)$$

where $t_j = t + d_j \Delta t$ and $d_j = \sum_{k=1}^j b_k$ for $0 \leq j \leq N_{\text{SO}}$. Note that $\hat{\mathbf{U}}^{\text{SO/ME}}$ is of order M_{SO} if $\hat{\mathbf{U}}_{\hat{\mathbf{B}}(t')}^{\text{ME}}$ is exact or has an error of a higher-order in Δt than the split-operator algorithm.

3.2 Numerical Implementation of the Exact Propagation

We describe the numerical implementation of the exact propagation scheme as defined by Eqs. (1.16) and (1.19), in the absence and in the presence of laser field, respectively.

3.2.1 Exact Propagation in the Absence of Laser Field

In the absence of the field, the Hamiltonian $\hat{\mathbf{H}}_0 \equiv \hat{\mathbf{T}} + \hat{\mathbf{V}}_0$ is time-independent. Therefore, the exact evolution operator $\hat{\mathbf{U}}_0(\Delta t)$ is implemented in terms of Eq. (3.2) with $\hat{\mathbf{A}} = \hat{\mathbf{T}}$ and $\hat{\mathbf{B}} = \hat{\mathbf{V}}_0$ as

$$\hat{\mathbf{U}}_0^{\text{SO}}(\Delta t) := \hat{\mathbf{U}}_{\hat{\mathbf{T}}+\hat{\mathbf{V}}_0}^{\text{SO}}(\Delta t). \quad (3.19)$$

Typically, nuclear propagation time step is used ($\Delta t = \Delta t_n$) since both $\hat{\mathbf{U}}_{\hat{\mathbf{T}}}(\Delta t)$, $\hat{\mathbf{U}}_{\hat{\mathbf{V}}_0}(\Delta t)$ can be evaluated exactly for arbitrary Δt .

3.2.2 Exact Propagation in the Presence of Time-Dependent Laser Field

During the laser pulse, the full Hamiltonian $\hat{\mathbf{H}}(t) \equiv \hat{\mathbf{T}} + \hat{\mathbf{V}}(t)$ necessitates using the time-dependent version (3.6) of the split-operator method with $\hat{\mathbf{A}} = \hat{\mathbf{T}}$ and $\hat{\mathbf{B}}(t) = \hat{\mathbf{V}}(t)$. The evolution operator is implemented as

$$\hat{\mathbf{U}}^{\text{SO}}(t+\Delta t, t) := \hat{\mathbf{U}}_{\hat{\mathbf{T}}+\hat{\mathbf{V}}(t')}^{\text{SO}}(t+\Delta t, t), \quad (3.20)$$

where Δt is typically the electronic time step Δt_e . Indeed, fast electronic oscillations present in the laser field expression need to be resolved.

3.3 Numerical Implementation of the Basic Approximations

In this section, we describe the numerical implementation of the basic approximations to the exact propagation scheme. As for the exact implementation (Sec. 3.2), a single numerical step is presented. One has to know that the numerical implementation of the time-dependent perturbation theory does not carry all the geometric properties. Indeed, as a direct consequence of its definition, its implementation is neither unitary nor symplectic.

3.3.1 Condon Approximation

In the Condon approximation, the exact propagator (3.20) is simplified by the fact that the interaction potential is independent of position

$$\hat{\mathbf{V}}_{\text{int},c}(t) \equiv \hat{\mathbf{I}}\mathbf{V}_{\text{int},c}(t). \quad (3.21)$$

3.3.2 Time-Dependent Perturbation Theory

The time-dependent perturbation theory expression (2.10), if implemented directly, would scale quadratically with time because of the time integral over intermediate times. Instead, it is possible to derive a recursive relation for $\hat{\mathbf{U}}_p(t + \Delta t, t_0)$, which, however, depends on both $\hat{\mathbf{U}}_p(t, t_0)$ and $\hat{\mathbf{U}}_0(t - t_0)$ at the previous time step

$$\hat{\mathbf{U}}_p(t + \Delta t, t_0) := \hat{\mathbf{U}}_0(\Delta t) \left[\hat{\mathbf{U}}_p(t, t_0) - \frac{i}{\hbar} \int_t^{t+\Delta t} dt' \hat{\mathbf{U}}_0(t - t') \hat{\mathbf{V}}_{\text{int}}(t') \hat{\mathbf{U}}_0(t' - t_0) \right]. \quad (3.22)$$

We should emphasize that our goal is to have a consistent implementation with the split-operator method, which is obviously not the case of the above formula.

If the interaction potential is evaluated only once at every full split-operator step, we can use (3.22) to implement the time-dependent perturbation theory in the split-operator formalism. More appropriate, however, is to take into account different length $a_j \Delta t$ and $b_j \Delta t$ of the kinetic and potential propagation steps, in which case one has to apply formula (3.22) separately to the kinetic propagation, for which $\Delta t \rightarrow \Delta t_T = a_j \Delta t$, $\hat{\mathbf{H}}_0 \rightarrow \hat{\mathbf{T}}$, and $\hat{\mathbf{V}}_{\text{int}} \rightarrow 0$, and to the potential propagation, for which $\Delta t \rightarrow \Delta t_V = b_j \Delta t$ and $\hat{\mathbf{H}}_0 \rightarrow \hat{\mathbf{V}}_0$. In summary, the time-dependent perturbation theory consistent with arbitrary split-operator

3.4. Numerical Implementation of the Combinations of the Basic Approximations

splitting is implemented as follows

$$\hat{U}_{p,T}^{\text{ESO}}(t + \Delta t_T, t_0) := \hat{U}_{\hat{\mathbf{T}}}(\Delta t_T) \hat{U}_{p,V}^{\text{ESO}}(t, t_0), \quad (3.23)$$

$$\hat{U}_{0,T}^{\text{ESO}}(t + \Delta t_T, t_0) := \hat{U}_{\hat{\mathbf{T}}}(\Delta t_T) \hat{U}_{0,V}^{\text{ESO}}(t, t_0), \quad (3.24)$$

$$\hat{U}_{p,V}^{\text{ESO}}(t + \Delta t_V, t_0) := \hat{U}_{\hat{\mathbf{V}}_0}(\Delta t_V) \left[\hat{U}_{p,T}^{\text{ESO}}(t, t_0) \right. \quad (3.25)$$

$$\left. - \frac{i}{\hbar} \int_t^{t+\Delta t_V} dt' \hat{U}_{\hat{\mathbf{V}}_0}(t - t') \hat{V}_{\text{int}}(t') \hat{U}_{\hat{\mathbf{V}}_0}(t' - t) \hat{U}_{0,T}^{\text{ESO}}(t, t_0) \right], \quad (3.26)$$

$$\hat{U}_{0,V}^{\text{ESO}}(t + \Delta t_V, t_0) := \hat{U}_{\hat{\mathbf{V}}_0}(\Delta t_V) \hat{U}_{0,T}^{\text{ESO}}(t, t_0), \quad (3.27)$$

where elementary split-operator (ESO) have been introduced. The unperturbed propagation is the same as in Eq. (3.19), while the time-dependent perturbation theory propagation is coupled to it at each potential propagation step via Eq. (3.26). In order for the time-dependent perturbation theory algorithm to have the same order in Δt as the unperturbed propagation, the integral present in Eqs. (3.22) and (3.26) must be computed exactly or using a numerical integration scheme with an error of higher-order in Δt than the order required by the unperturbed split-operator.

3.3.3 Rotating-Wave Approximation

The split-operator implementation of the rotating-wave approximation in the rotating frame consists in using the time-dependent split-operator formula (3.6) with $\hat{\mathbf{A}} = \hat{\mathbf{T}}$ and $\hat{\mathbf{B}}(t) = \hat{\mathbf{V}}_r(t)$,

$$\hat{U}_r^{\text{SO}}(t + \Delta t, t) := \hat{U}_{\hat{\mathbf{T}} + \hat{\mathbf{V}}_r(t')}^{\text{SO}}(t + \Delta t, t). \quad (3.28)$$

3.3.4 Ultrashort-Pulse Approximation

The ultrashort-pulse approximation evolution operator (2.35) is implemented via a combination of the Magnus expansion (3.15) applied to the electronic propagation and the concatenated split-operator method (3.4) applied to the nuclear and vibronic coupling propagation

$$\hat{U}_u^{\text{CSO/ME}}(t_f, t_i) := \hat{U}_{\hat{\mathbf{H}}_{\text{n+ne}}}^{\text{CSO}}(t_f - t_m) \hat{U}_{\hat{\mathbf{V}}_{\text{e+int}}(t)}^{\text{ME}}(t_f, t_i) \hat{U}_{\hat{\mathbf{H}}_{\text{n+ne}}}^{\text{CSO}}(t_m - t_i). \quad (3.29)$$

3.4 Numerical Implementation of the Combinations of the Basic Approximations

In what follows, we present the numerical implementation of the combination of the basic approximations. As the numerical implementation of the time-dependent perturbation theory is neither unitary nor symplectic, then, any of its combination will also not be.

3.4.1 Combinations with Condon Approximation

The combinations with the Condon approximation are the simplest to express and therefore are not written down explicitly. Note that since the dipole moment and hence the interaction potential is independent of position [$\hat{\mathbf{V}}_{\text{int},c}(t) \equiv \hat{\mathbf{I}}\mathbf{V}_{\text{int},c}(t)$], adding the Condon approximation simplifies the numerical implementation significantly. In particular, any combinations with the time-dependent perturbation theory or ultrashort-pulse approximation greatly simplify since the molecular operators $\hat{\mathbf{V}}_{\text{int}}$ and $\hat{\mathbf{U}}_{\hat{\mathbf{V}}_{\text{e+int}}(t)}$ in Eqs. (2.10) and (2.35) become just electronic operators: $\hat{\mathbf{V}}_{\text{int}} \rightarrow \hat{\mathbf{I}}\mathbf{V}_{\text{int}}$ and $\hat{\mathbf{U}}_{\hat{\mathbf{V}}_{\text{e+int}}(t)} \rightarrow \hat{\mathbf{I}}\mathbf{U}_{\mathbf{V}_{\text{e+int}}(t)}$.

3.4.2 Time-Dependent Perturbation Theory and Rotating-Wave Approximation

The combination of the time-dependent perturbation theory with rotating-wave approximation is implemented in the rotating frame in the same way as the time-dependent perturbation theory itself, except that one has to make the following obvious replacements in Eqs. (3.23)-(3.27): $\hat{\mathbf{U}}_p^{\text{ESO}} \rightarrow \hat{\mathbf{U}}_{pr}^{\text{ESO}}$, $\hat{\mathbf{U}}_0^{\text{ESO}} \rightarrow \hat{\mathbf{U}}_{0,r}^{\text{ESO}}$, $\hat{\mathbf{V}}_0 \rightarrow \hat{\mathbf{V}}_{0,r}$, and $\hat{\mathbf{V}}_{\text{int}} \rightarrow \hat{\mathbf{V}}_{\text{int},r}$. The most important, Eq. (3.26), changes to

$$\begin{aligned} \hat{\mathbf{U}}_{pr,V}^{\text{ESO}}(t + \Delta t_V, t_0) := & \hat{\mathbf{U}}_{\hat{\mathbf{V}}_{0,r}}(\Delta t_V) \left[\hat{\mathbf{U}}_{pr,T}^{\text{ESO}}(t, t_0) \right. \\ & \left. - \frac{i}{\hbar} \int_t^{t+\Delta t_V} dt' \hat{\mathbf{U}}_{\hat{\mathbf{V}}_{0,r}}(t - t') \hat{\mathbf{V}}_{\text{int},r}(t') \hat{\mathbf{U}}_{\hat{\mathbf{V}}_{0,r}}(t' - t) \hat{\mathbf{U}}_{0,r,T}^{\text{ESO}}(t, t_0) \right]. \end{aligned} \quad (3.30)$$

3.4.3 Time-Dependent Perturbation Theory and Ultrashort-Pulse Approximation

As for the time-dependent perturbation theory and ultrashort-pulse approximation, one has to deal with Eq. (2.44) which is numerically implemented as follows

$$\hat{\mathbf{U}}_{pu}^{\text{CSO}}(t_f, t_i) := \hat{\mathbf{U}}_{\hat{\mathbf{H}}_{\text{n+ne}}}^{\text{CSO}}(t_f - t_m) \hat{\mathbf{U}}_{\hat{\mathbf{V}}_{\text{e+int}}(t),p}(t_f, t_i) \hat{\mathbf{U}}_{\hat{\mathbf{H}}_{\text{n+ne}}}^{\text{CSO}}(t_m - t_i), \quad (3.31)$$

where $\hat{\mathbf{U}}_{\hat{\mathbf{V}}_{\text{e+int}}(t),p}$ is propagated with the time-dependent perturbation theory scheme (3.22) based on the splitting $\hat{\mathbf{V}}_{\text{e+int}}(t) \equiv \hat{\mathbf{I}}\mathbf{V}_{\text{e}} + \hat{\mathbf{V}}_{\text{int}}(t)$

$$\begin{aligned} \hat{\mathbf{U}}_{\hat{\mathbf{V}}_{\text{e+int}}(t'),p}(t + \Delta t, t_0) := & \mathbf{U}_{\mathbf{V}_{\text{e}}}(\Delta t) \left[\hat{\mathbf{U}}_{\hat{\mathbf{V}}_{\text{e+int}}(t'),p}(t, t_0) \right. \\ & \left. - \frac{i}{\hbar} \int_t^{t+\Delta t} dt' \mathbf{U}_{\mathbf{V}_{\text{e}}}(t - t') \hat{\mathbf{V}}_{\text{int}}(t') \mathbf{U}_{\mathbf{V}_{\text{e}}}(t' - t_0) \right]. \end{aligned} \quad (3.32)$$

3.4.4 Rotating-Wave and Ultrashort-Pulse Approximations

The rotating-wave and ultrashort-pulse approximation evolution operator in the rotating frame is implemented via a combination of the Magnus expansion (3.15) applied to the electronic propagation with an effective potential $\hat{\mathbf{V}}_{\text{e+int},r}(t)$ and of the split-operator method (3.2) applied to the nuclear and vibronic coupling propagation

$$\hat{\mathbf{U}}_{ru}^{\text{CSO/ME}}(t_f, t_i) := \hat{\mathbf{U}}_{\hat{\mathbf{H}}_{\text{n+ne},r}}^{\text{CSO}}(t_f - t_m) \hat{\mathbf{U}}_{\hat{\mathbf{V}}_{\text{e+int},r}(t)}^{\text{ME}}(t_f, t_i) \hat{\mathbf{U}}_{\hat{\mathbf{H}}_{\text{n+ne},r}}^{\text{CSO}}(t_m - t_i). \quad (3.33)$$

3.4.5 Time-Dependent Perturbation Theory, Rotating-Wave, and Ultrashort-Pulse Approximations

This combination is implemented by applying the time-dependent perturbation theory to the evolution operator $\hat{\mathbf{U}}_{\hat{\mathbf{V}}_{\text{e+int},r}(t)}$. The resulting evolution operator in the rotating frame is

$$\hat{\mathbf{U}}_{pru}^{\text{CSO}}(t_f, t_i) := \hat{\mathbf{U}}_{\hat{\mathbf{H}}_{\text{n+ne},r}}^{\text{CSO}}(t_f - t_m) \hat{\mathbf{U}}_{\hat{\mathbf{V}}_{\text{e+int},r}(t),p}^{\hat{\mathbf{V}}_{\text{e+int},r}(t)}(t_f, t_i) \hat{\mathbf{U}}_{\hat{\mathbf{H}}_{\text{n+ne},r}}^{\text{CSO}}(t_m - t_i), \quad (3.34)$$

where $\hat{\mathbf{U}}_{\hat{\mathbf{V}}_{\text{e+int},r}(t),p}$ is propagated using the time-dependent perturbation theory implementation (3.22) as

$$\begin{aligned} \hat{\mathbf{U}}_{\hat{\mathbf{V}}_{\text{e+int},r}(t'),p}^{\hat{\mathbf{V}}_{\text{e+int},r}(t')}(t + \Delta t, t_0) &:= \mathbf{U}_{\hat{\mathbf{V}}_{\text{e},r}}(\Delta t) \left[\hat{\mathbf{U}}_{\hat{\mathbf{V}}_{\text{e+int},r}(t'),p}^{\hat{\mathbf{V}}_{\text{e+int},r}(t')}(t, t_0) \right. \\ &\quad \left. - \frac{i}{\hbar} \int_t^{t+\Delta t} dt' \mathbf{U}_{\hat{\mathbf{V}}_{\text{e},r}}(t - t') \hat{\mathbf{V}}_{\text{int},r}(t') \mathbf{U}_{\hat{\mathbf{V}}_{\text{e},r}}(t' - t_0) \right]. \end{aligned} \quad (3.35)$$

3.5 Numerical Tests

We present the verification of the order of convergence, unitarity, and symplecticity of the algorithms by using a one-dimensional two-state displaced harmonic oscillator. Moreover, we raised the question of the speedup when using higher-order schemes.

3.5.1 Verification of the Geometric Properties of the Implemented Integrators

We assume a one-dimensional two-state displaced harmonic oscillator with linear transition-dipole couplings and we perform the calculations using natural units. The nuclear displacement of the excited state with respect to the ground state is set to $\Delta Q_{21} = |(Q_0)_2 - Q_0| = 4$ n.u. where $Q_0 = 0$ and $(Q_0)_2$ is the minimum position of the excited state. This makes the vertical energy gap $(\omega_e)_{12}$ to be 108 n.u. The zeroth- and first-order terms of the transition dipole moment $[\mu_{12}(Q_0)$ and $\mu'_{12}(Q_0)]$ are set to 1 and 0.1 n.u., respectively. In addition, we do not consider any nonadiabatic couplings between the two electronic states. The

initial state is the vibrational ground state of the ground potential energy surface S_1 . By definition, the vibrational state has a Gaussian shape centered at Q_0 , and because of our choice of units, its width σ is equal to unity.

In order to test our different algorithms, we propagate the wavefunction for 16 n.u. As for the time-independent Hamiltonian, initially, we vertically transfer the wavefunction to the excited state and let it evolve. It ensures that there is some nuclear dynamics during the propagation. Indeed, the initial state is no longer a vibrational eigenstate of the given electronic state. As for the time-dependent Hamiltonian, a single laser pulse of finite length with the following properties: $\Delta t_{\text{pulse}} = 2$, $t_m = 0$, $\varphi_{\text{pulse}} = 0$, $\omega_{\text{pulse}} = (\omega_e)_{12}$, and $E_0 = 5$ n.u. have been used. Moreover, the grid is composed of 256 points equally spaced between -10 and 26 n.u. The propagation is performed, if not otherwise indicated, assuming an electronic time step Δt_e of 2^{-11} n.u. and a nuclear time step Δt_n of 2^{-7} n.u., using a fourth-order split-operator algorithm generated from the recursive method developed by Yoshida [67], and, when needed, combined with the sixth-order commutator-free Magnus expansion with five exponentials [76] and with the sixth-order Newton-Cotes-like formula known as Boole's rule [123].

First, the population dynamics under the influence of the electric field for the exact quantum calculation, the basic approximations, and the most approximate method are depicted in Fig. 3.1. We observe that the set of parameters we are using is such that the time-dependent perturbation theory is not able to reproduce the exact result and that the ultrashort-pulse approximation slightly breaks down.

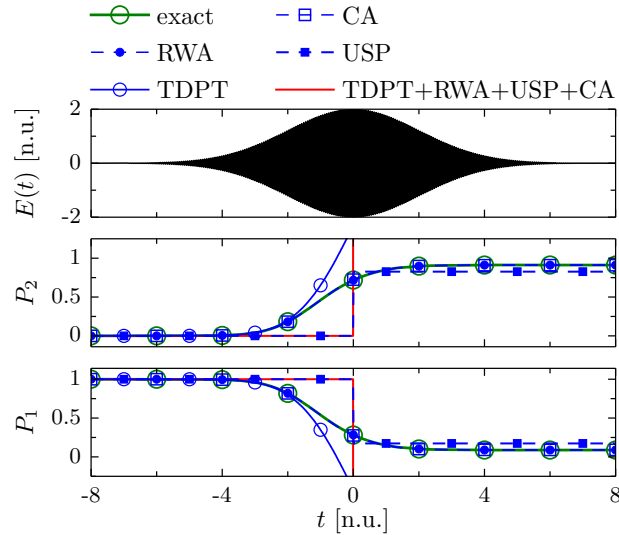


Figure 3.1 – Laser pulse shape and population dynamics obtained with the exact quantum calculation and with several level of approximations applied to a one-dimensional two-state displaced harmonic system. Time-dependent perturbation theory and its combinations are not able to reproduce the exact calculation.

Then, we investigate the convergence with respect to grid density for the exact quantum calculation and all the approximations. To do so, we compute the error of the wavefunction

at initial and final time using the exact propagation scheme as a function of the number of grid points. ψ_0 represents the benchmark wavefunction, assumed to be fully converged, and propagated using a grid composed of 65536 points. We depict the error in Figs. 3.2 and 3.3 and it reflects our actual choice of the grid.

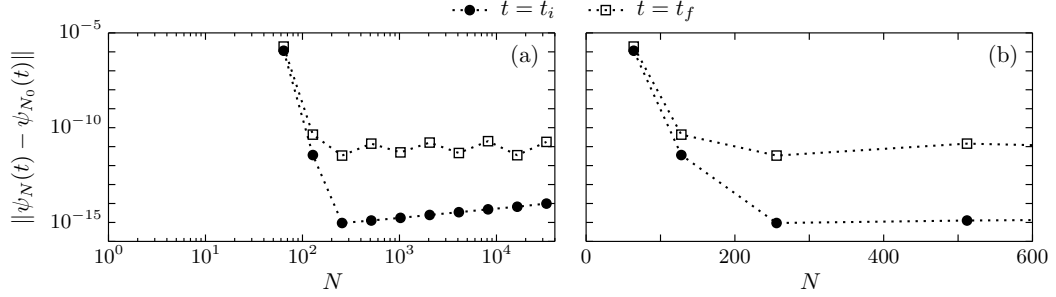


Figure 3.2 – (a) loglog scale and (b) semilog scale of the convergence with respect to grid density for the exact quantum calculation applied to a one-dimensional two-state displaced harmonic system.

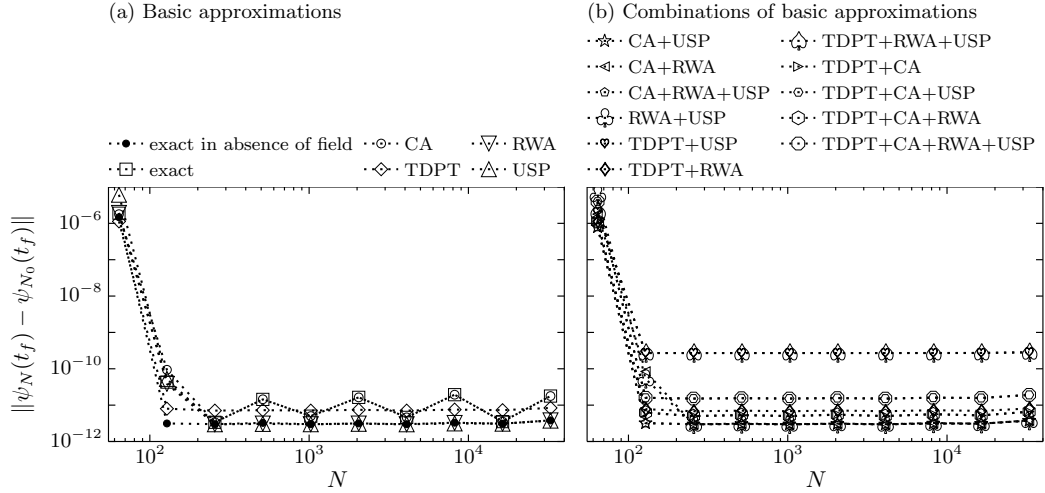


Figure 3.3 – Convergence with respect to grid density for the exact quantum calculation and all possible approximations applied to a one-dimensional two-state displaced harmonic system.

In addition, in order to demonstrate that our different algorithms are accurate up to any order in the time step Δt , we compute the error of the wavefunction at final time and depict it in Fig. 3.4 for the exact, exact in absence of field, and basic approximations up to eighth-order split-operator scheme and in Fig. 3.5 for all the possible combinations of the basic approximations using second- and fourth-order split-operator schemes. ψ_0 represents the benchmark wavefunction, assumed to be fully converged, and propagated with a very small time step of 2^{-15} n.u.

As for the time-dependent perturbation theory, we observe that instead of being fourth-, sixth-, or eighth-order at high accuracy, it is only first-order. The reason is that a competition between numerical integration and split-operator error is present. At low accuracy, the numerical integration error is probably much smaller than the split-operator

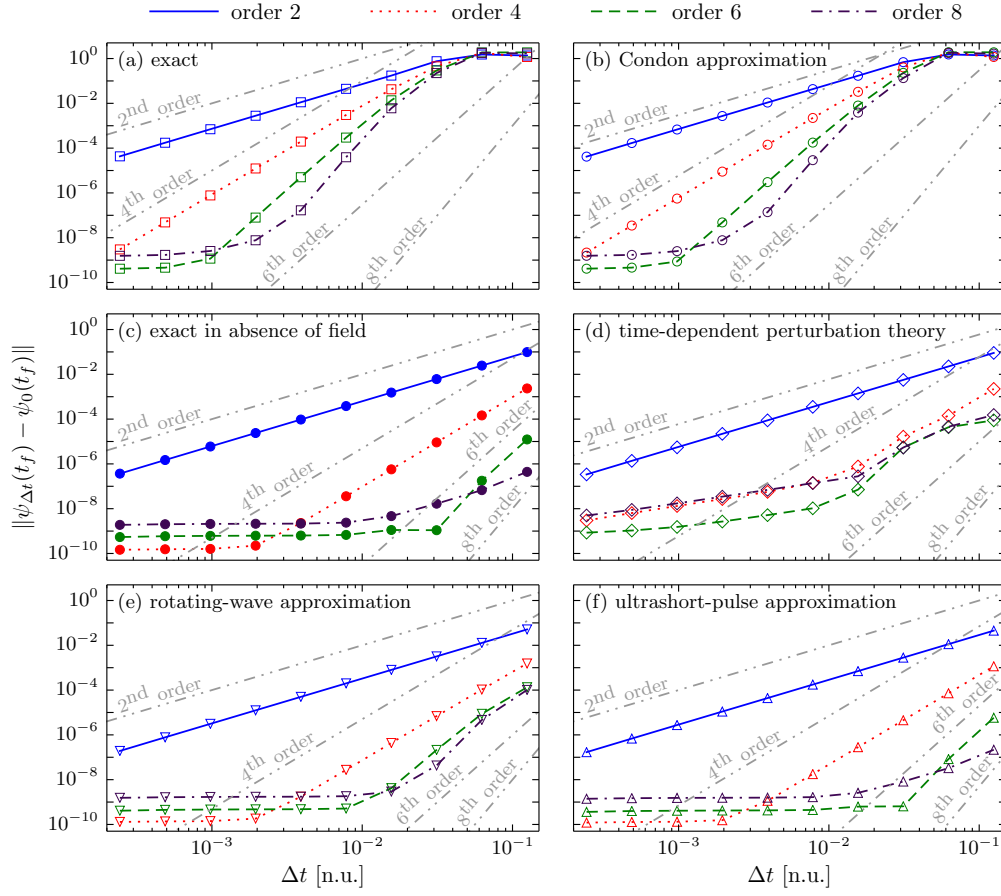


Figure 3.4 – Error of various approximations as a function of the time step Δt using second-, fourth-, sixth-, and eighth-order split-operator algorithms.

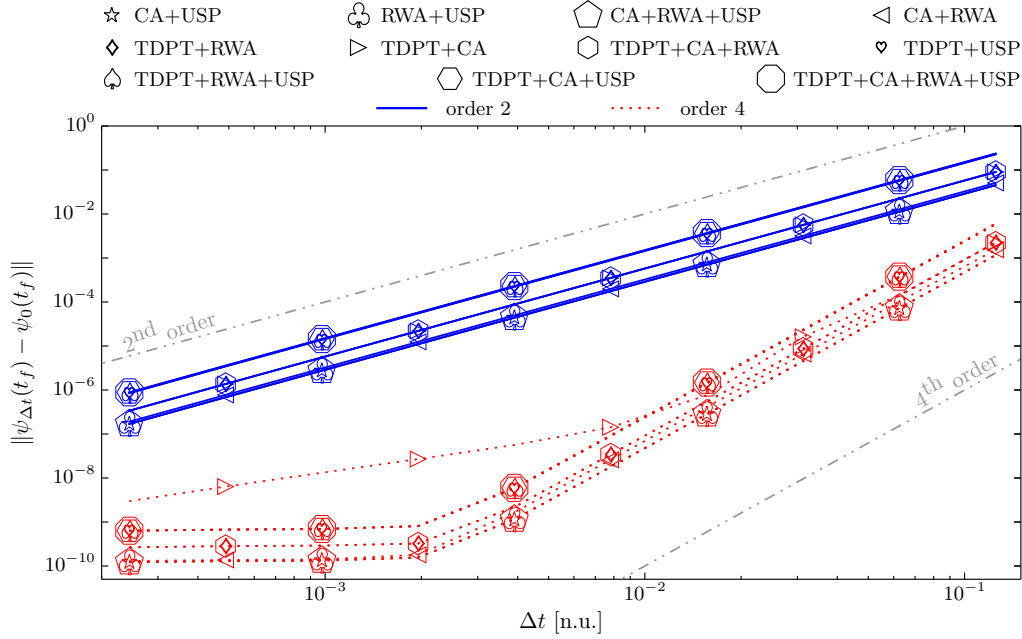


Figure 3.5 – Error of various combinations of the basic approximations as a function of the time step Δt using second- and fourth-order split-operator algorithms.

error so the leading order is due to split-operator. At high accuracy, the numerical integration error is presumably close to the split-operator error so there is no leading order anymore. The combination of the time-dependent perturbation theory and Condon approximation is first- instead of fourth-order at high accuracy for the same reason. Besides, the reason why eighth-order curves for the exact in absence of field and ultrashort-pulse approximation do not have the right order of convergence is certainly due to the fact that for the biggest time step we are using, the error is already too small. As for an error around 10^{-10} , we observe a plateau that is due to the fact that machine precision is reached.

Furthermore, we distinguish two different groups of convergence, which means that two different set of time steps exist. The first one is composed by the exact calculation and the Condon approximation and the second one by all the other methods. The first group requires an electronic time step whereas the second one a nuclear time step. Indeed, as for the exact calculation and the Condon approximation, the oscillations of the laser field need to be resolved and they obviously occur on an electronic time scale. As for the second group, as for the exact in absence of field, a nuclear time step is sufficient to resolve the nuclear dynamics when nonadiabatic couplings are not present. As for the rotating-wave approximation, the essence of the approximation is to smooth out the electronic oscillations of the electric field so they need not to be resolved anymore. As for the time-dependent perturbation theory, treating the time-dependent perturbation to first-order enables to use a nuclear time step. Finally, as for the ultrashort-pulse approximation, the split-operator algorithm only deals with the nuclear part of the full Hamiltonian, so a nuclear time step is sufficient.

In addition, when we assume an error of 10^{-5} , we observe that when using the second-order scheme, a time step 16 times bigger is enabled for the rotating-wave approximation, time-dependent perturbation theory, and ultrashort-pulse approximation compared to the one for the exact calculation or the Condon approximation. Moreover, using a fourth-order scheme instead of a second-order one enables to use a time step 16 times bigger for a given method. Thus, combining both kind of speedups provide the availability to use a time step 256 times bigger.

Then, the convergence of the electronic propagator contained in the ultrashort-pulse approximation $\hat{U}_{\hat{V}_{e+int}(t)}(t_f, t_i)$ and its combinations with the Condon and rotating-wave approximations is investigated. It is obtained using the numerical Magnus expansion. To do so, the split-operator nuclear time step is fixed to $2^{-7} \hbar/E_h$ and the electronic time step Δt present in the electronic evolution operator is varied. We depict the results using second-order Magnus expansion and fourth- and sixth-order commutator-free Magnus expansion in Fig. 3.6.

Assuming an error of 10^{-5} , we see that for the ultrashort-pulse approximation and its combination with the Condon approximation, using a sixth-order commutator-free Magnus expansion enables to use a time step 64 times bigger than with the second-order Magnus expansion. As for the combination of the rotating-wave and ultrashort-pulse approximations

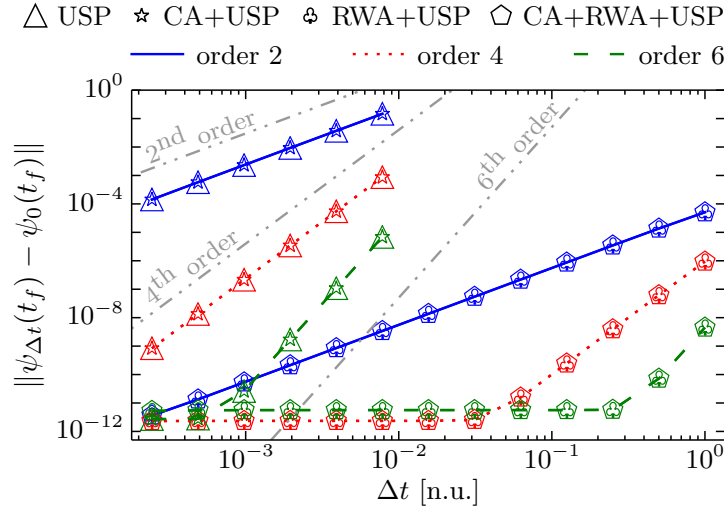


Figure 3.6 – Error of various approximations as a function of the time step Δt using second-order Magnus expansion and fourth- and sixth-order commutator-free Magnus expansions.

and its combination with the Condon approximation, for an error of 10^{-9} , the same scaling factor for the time step is observed when using a sixth-order commutator-free Magnus expansion instead of the second-order Magnus expansion. If we compare the ultrashort-pulse approximation (and its combination with the Condon approximation) with the combination of the rotating-wave and ultrashort-pulse approximations (and its combination with the Condon approximation), when using sixth-order commutator-free Magnus expansion, a time step 256 times bigger is allowed for the approximations containing the rotating-wave approximation. Therefore, assuming an error of 10^{-9} and extrapolating the error of the second-order Magnus expansion, a speedup of 16384 is achieved when using the combination of the Condon, rotating-wave, and ultrashort-pulse approximations with sixth-order commutator-free Magnus expansion instead of the ultrashort-pulse approximation with second-order Magnus expansion. Finally, we observe a plateau for an error of 10^{-12} because machine precision is reached.

Next, we investigate the convergence of the integral present in the numerical implementation of the time-dependent perturbation theory. To do so, the integral, assuming an integration time of 2^{-7} n.u. (the nuclear time step), is computed at the maximum value of the electric field. We vary the number of steps from 1 to 256. The latter is assumed to provide a fully converged result. We depict the error of the wavefunction right after the integration in Fig. 3.7.

We observe in Fig. 3.7 that using the sixth-order scheme instead of the first-order one implies the possible use of a time step 64 times bigger. Moreover, as the sixth-order scheme has a very small error, we assume that for a given reasonable nuclear time step, the integral will be accurate enough when computed using a single step.

Fig. 3.8 depicts the order of convergence of the integral for the combination of the time-

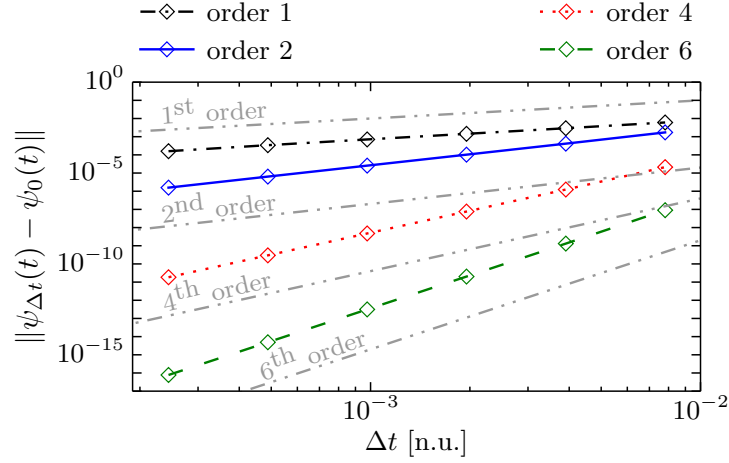


Figure 3.7 – Error of the integral in time-dependent perturbation theory as a function of the time step Δt using first-, second-, fourth-, and sixth-order numerical integration schemes.

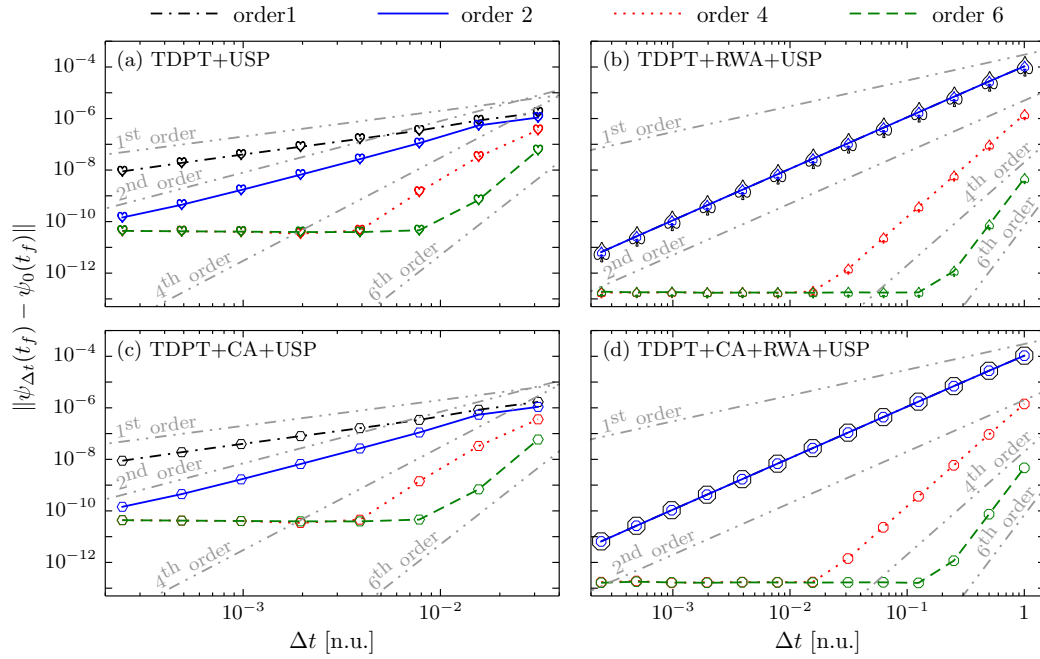


Figure 3.8 – Error of the integral in the combination of time-dependent perturbation theory and ultrashort-pulse approximation and its combinations with the Condon and rotating-wave approximations as a function of the time step Δt using first-, second-, fourth-, and sixth-order numerical integration schemes.

dependent perturbation theory and ultrashort-pulse approximation and its combinations with the Condon and rotating-wave approximations, computed at the end of the simulation. The fully converged result assumes a time step of 2^{-15} n.u. We observe that when the time-dependent perturbation theory and ultrashort-pulse approximation is combined with the rotating-wave approximation, first- and second-order algorithms merge. The reason is probably due to the fact that the function to integrate is so smooth that taking the left-, right-, or middle-point for the numerical integration scheme provides an algorithm accurate up to second-order.

In addition, the unitarity of the exact calculation and the Condon, rotating-wave, and ultrashort-pulse approximations, using a fourth-order split-operator method, is depicted in Fig. 3.9. The electronic time step is 2^{-11} n.u. while the nuclear one is set 2^{-7} n.u. Note that, by definition, the time-dependent perturbation theory is non-unitary that is why we do not show it here.

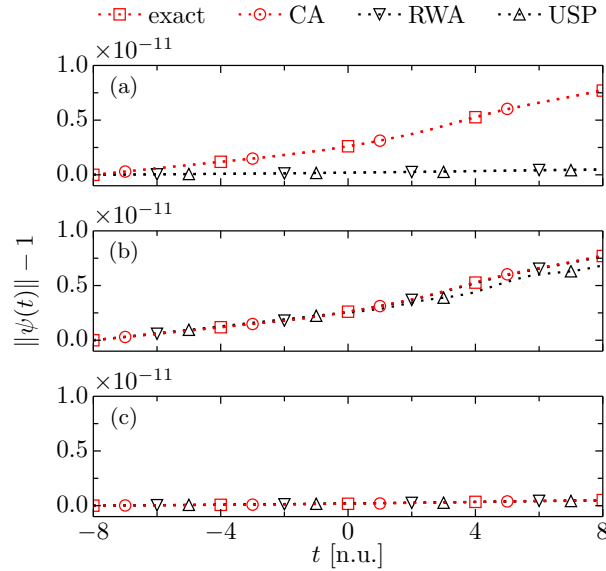


Figure 3.9 – Verification of the unitarity of several algorithms using a fourth-order split-operator method. (a): an electronic time step is used for the exact quantum calculation and the Condon approximation and a nuclear time step is used for the rotating-wave and ultrashort-pulse approximations, (b): only the electronic time step is used, and (c): only the nuclear time step is used.

As for the three panels, the error on the norm of the wavefunction lies in the machine precision. In addition, we observe in panel (a) that a bigger continuous drift is observed for the exact calculation and the Condon approximation than for the rotating-wave and ultrashort-pulse approximations. The reason is that as an electronic time step, that is eight times smaller than the nuclear one, is used for the formers, there is a faster accumulation of error. Indeed, we see from panel (b) that when the four numerical schemes are propagating with the electronic time step, they all share the same drift, that is similar to the one of the exact calculation and the Condon approximation from panel (a). In contrary, if we use a nuclear time step for propagating the four methods, as in panel (c), they also all

share the same drift, but it is much smaller and similar to the one of the rotating-wave and ultrashort-pulse approximations from panel (a).

Besides, we verify the symplecticity, defined as a canonical symplectic two-form Ω on the Hilbert space [129]

$$\Omega[\psi_1(t), \psi_2(t)] = -2\hbar \text{Im}\langle\psi_1(t)|\psi_2(t)\rangle, \quad (3.36)$$

where $\psi_1(t), \psi_2(t) \in \text{Hilbert space}$,

for our algorithms and we depict it in Fig. 3.10. At initial time, $\psi_1(t_i)$ is the ground vibrational state of the electronic ground state with an initial momentum of 1 n.u. and $\psi_2(t_i)$ is the same as $\psi_1(t_i)$ but displaced by 1 n.u. and equally distributed between both ground and first excited states.

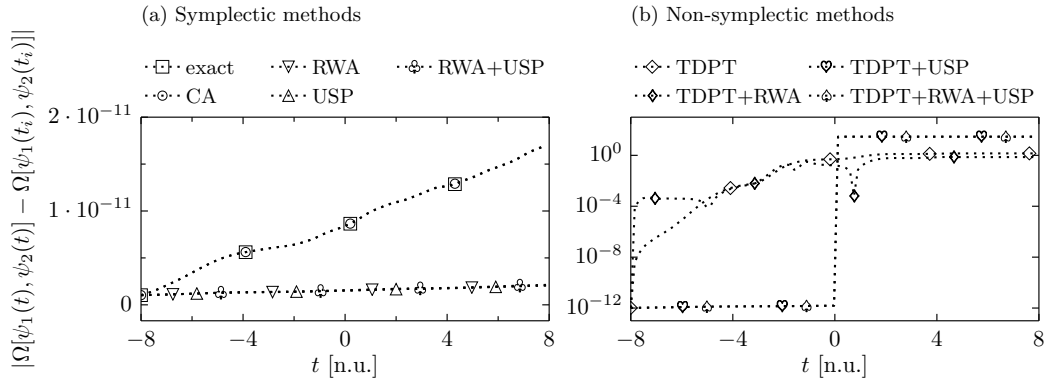


Figure 3.10 – Verification of the symplecticity of several algorithms using a fourth-order split-operator method: (a) symplectic methods, (b) non-symplectic ones.

The real bilinear form Ω of the exact calculation, the Condon, rotating-wave, and ultrashort-pulse approximations, as well as the combination of the rotating-wave and ultrashort-pulse approximations is preserved up to machine precision. Due to the factor of two given in Eq. (3.36), the drift is twice bigger than the one observed in Fig. 3.9. Note that we do not show the combinations with the Condon approximation because any symplectic method combined with the Condon approximation stays symplectic and vice-versa.

3.5.2 Speedup Achieved with the High-Order Geometric Integrators

Despite the fact that our algorithms are accurate up to any order in the time step, one question may be raised: is it worth going to higher-order accuracy? Indeed, why not simply use, as most people do, the very well-known second-order algorithm. The answer is all about cost (CPU time) versus accuracy (error). In fact, any given error, even very low, can be achieved with a first-order method. However, the cost will be very huge. Therefore, in order to minimize this cost, the idea is to use a higher-order scheme which should, in principle, allow for a bigger time step. Then, even if a single splitting step is

computationally more expensive for a higher-order scheme, the total number of steps to be performed is smaller, so the total CPU time is reduced.

In order to illustrate what we wrote, panel (a) of Figs. 3.11 and 3.12 depicts the computational cost when using first-, second-, and fourth-order split-operator methods and second-order Magnus expansion, and fourth- and sixth-order commutator-free Magnus expansions, respectively. Panel (b) of Figs 3.11 and 3.12 shows the speedup of the exact calculation and the ultrashort-pulse approximation, respectively. The speedup is defined as the ratio between the CPU time obtained from two different orders of accuracy of a given propagation method.

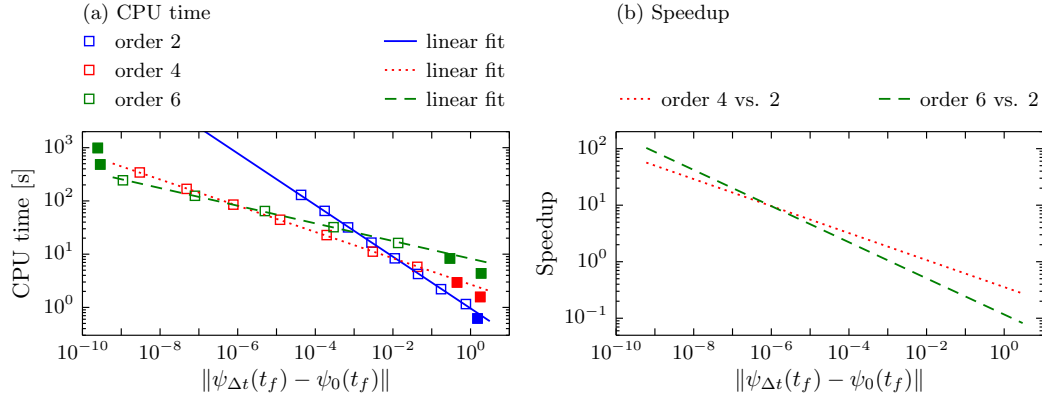


Figure 3.11 – (a) Computational cost and (b) speedup for the exact quantum calculation as a function of the error using second-, fourth- and sixth-order split-operator algorithms. Note that we discarded filled markers to do the linear fit.

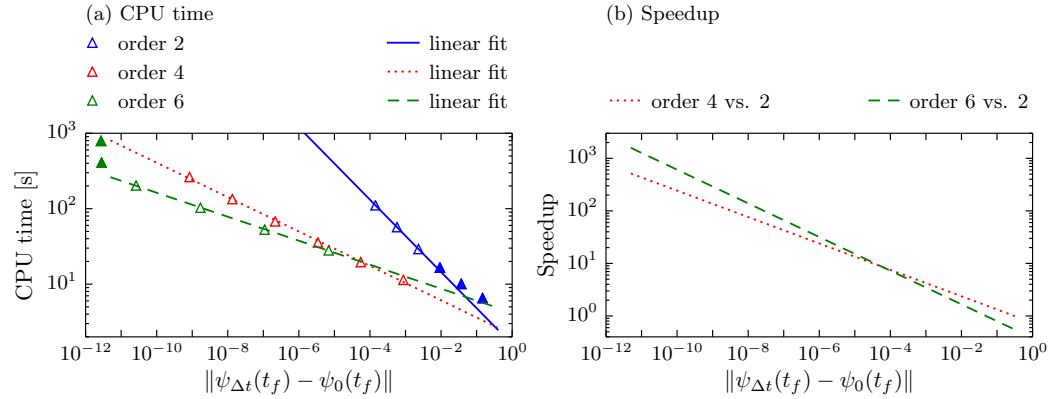


Figure 3.12 – (a) Computational cost and (b) speedup for the ultrashort-pulse approximation as a function of the error using second-order Magnus expansion and fourth- and sixth-order commutator-free Magnus expansions. Note that we discarded filled markers to do the linear fit.

As depicted in Fig. 3.11, we see that it pays off to use the fourth-order scheme already for an error of 10^{-2} and that for an error of 10^{-7} , a speedup of 10 is achieved. In addition, it pays off to use the sixth-order algorithm when the requested error is less than 10^{-7} . A speedup of 100 can be achieved when using sixth-order instead of second-order for an

accuracy of 10^{-9} .

As for the ultrashort-pulse approximation, we see that the second-order scheme must never be used. Indeed, the fourth-order commutator-free Magnus expansion is always faster. Furthermore, we observe that the sixth-order version is paying off for an error below 10^{-5} and that there is an exponential wall for an error of 10^{-12} which is due to the fact that the accuracy reaches the machine precision. Therefore, even by reducing the time step (which will increase the CPU time), the error stays the same.

4 Ultrashort- and δ -Pulse Approximations

The δ -function pulse, or “infinitely short” pulse approximation seems natural for the description of time-resolved spectroscopy. However, such pulses are not experimentally feasible and, moreover, are undesirable because they would simultaneously excite all dipole-allowed electronic states of the system. As a result, it is useful to consider the impulsive limit that defines a new kind of pulse and its related ultrashort-pulse approximation. In this chapter, we explore in more detail the ultrashort-pulse approximation and derive an analytical expression for its combination with the time-dependent perturbation theory; this expression significantly accelerates numerical calculations. We show that in the limit of the zero pulse width, the δ -pulse approximation is recovered. We illustrate the performance of the introduced approximations, using a three-dimensional model of pyrazine, in which it is essential to go beyond the δ -pulse limit in order to describe the dynamics correctly. The results of this chapter can be found in Ref. [130].

4.1 Theory

4.1.1 Analytical Expression for the Combination of Time-Dependent Perturbation Theory and Ultrashort-Pulse Approximation

Using the interaction picture (2.4) with a reference time at the center t_m of the pulse, the evolution operator given by Eq. (2.45) transforms to

$$\hat{\mathbf{U}}_{\hat{\mathbf{V}}_{e+\text{int}}(t),p,I}(t_f, t_i) := \mathbf{U}_{\mathbf{V}_e}(t_m - t_f) \hat{\mathbf{U}}_{\hat{\mathbf{V}}_{e+\text{int}}(t),p}(t_f, t_i) \mathbf{U}_{\mathbf{V}_e}(t_i - t_m) \quad (4.1)$$

$$= \hat{\mathbf{1}} - \frac{i}{\hbar} \int_{t_i}^{t_f} dt \mathbf{U}_{\mathbf{V}_e}(t_m - t) \hat{\mathbf{V}}_{\text{int}}(t) \mathbf{U}_{\mathbf{V}_e}(t - t_m). \quad (4.2)$$

While either of the last two expressions would already be useful for numerical implementation, it turns out that this evolution operator can be evaluated analytically if we know the Fourier transform

$$\tilde{E}(\omega) := \frac{1}{2\pi} \int_{\mathbb{R}} dt E(t) e^{i\omega t}$$

of the electric field.

Using the Fourier representation of the electric field

$$E(t) = \int_{\mathbb{R}} d\omega \tilde{E}_0(\omega) e^{-i\omega(t-t_m)},$$

$$\tilde{E}_0(\omega) := \tilde{E}(\omega) e^{-i\omega t_m},$$

and inserting the resolution of identity $\mathbf{1} = \sum_{n=1}^S |n\rangle\langle n|$ on both sides of $\hat{\mathbf{V}}_{\text{int}}(t)$ in Eq. (4.2) enables us to expand the expression in the electronic basis and gives

$$\begin{aligned} \hat{\mathbf{U}}_{\hat{\mathbf{V}}_{\text{e+int}}(t),p,I}(t_f, t_i) &= \hat{\mathbf{1}} + \frac{i}{\hbar} \sum_{j,k=1}^S \hat{\mu}_{jk} |j\rangle\langle k| \int_{t_i}^{t_f} dt e^{i\omega_{jk}(t-t_m)} E(t) \\ &= \hat{\mathbf{1}} + \frac{i}{\hbar} \sum_{j,k=1}^S \hat{\mu}_{jk} |j\rangle\langle k| \int_{\mathbb{R}} d\omega \tilde{E}_0(\omega) \int_{t_i}^{t_f} dt e^{i(\omega_{jk}-\omega)(t-t_m)} \\ &\approx \hat{\mathbf{1}} + \frac{2\pi i}{\hbar} \sum_{j,k=1}^S \hat{\mu}_{jk} |j\rangle\langle k| \int_{\mathbb{R}} d\omega \tilde{E}_0(\omega) \delta(\omega_{jk} - \omega) \\ &= \hat{\mathbf{1}} + \frac{2\pi i}{\hbar} \sum_{j,k=1}^S \hat{\mu}_{jk} |j\rangle\langle k| \tilde{E}_0(\omega_{jk}), \end{aligned} \quad (4.3)$$

where $\hat{\mu}_{jk} := \langle j|\hat{\boldsymbol{\mu}}|k\rangle$ is the matrix element of the transition dipole moment and $\omega_{jk} := (E_j - E_k)/\hbar$ is the transition frequency. In the penultimate row, we take the ultrashort-pulse approximation into account by setting $t_i \rightarrow -\infty$ and $t_f \rightarrow \infty$ to yield the δ -function. This beautiful formula is very intuitive and provides a rigorous justification for ignoring electronic states that are far off resonance. Indeed, the term $\sum_{j,k=1}^S \hat{\mu}_{jk} |j\rangle\langle k| \tilde{E}_0(\omega_{jk})$ provides a smooth cutoff for off-resonant states and not the usual abrupt cutoff where some states are considered and others completely ignored.

We rewrite the evolution operator given by Eq. (2.44) as

$$\begin{aligned} \hat{\mathbf{U}}_{pu}(t_f, t_i) &:= \hat{\mathbf{U}}_{\hat{\mathbf{H}}_{\text{n+ne}}}(t_f - t_m) \hat{\mathbf{U}}_{\hat{\mathbf{V}}_{\text{e+int}}(t),p,I}(t_f, t_i) \hat{\mathbf{U}}_{\hat{\mathbf{H}}_{\text{n+ne}}}(t_m - t_i) \\ &= \hat{\mathbf{U}}_{\hat{\mathbf{H}}_{\text{n+ne}}}(t_f - t_m) \mathbf{U}_{\mathbf{V}_e}(t_f - t_m) \hat{\mathbf{U}}_{\hat{\mathbf{V}}_{\text{e+int}}(t),p,I}(t_f, t_i) \mathbf{U}_{\mathbf{V}_e}(t_m - t_i) \hat{\mathbf{U}}_{\hat{\mathbf{H}}_{\text{n+ne}}}(t_m - t_i) \\ &= \hat{\mathbf{U}}_0(t_f - t_m) \left[\hat{\mathbf{1}} + \frac{2\pi i}{\hbar} \sum_{j,k=1}^S \hat{\mu}_{jk} |j\rangle\langle k| \tilde{E}_0(\omega_{jk}) \right] \hat{\mathbf{U}}_0(t_m - t_i), \end{aligned} \quad (4.4)$$

where in the penultimate row, we invoke the ultrashort-pulse approximation, i.e.,

$$\left[\hat{\mathbf{U}}_{\hat{\mathbf{H}}_{\text{n+ne}}}(t), \mathbf{U}_{\mathbf{V}_e}(t) \right] \approx 0,$$

which enables us to use the following concatenation

$$\hat{\mathbf{U}}_{\hat{\mathbf{H}}_{\text{n+ne}}}(t) \mathbf{U}_{\mathbf{V}_e}(t) = \mathbf{U}_{\mathbf{V}_e}(t) \hat{\mathbf{U}}_{\hat{\mathbf{H}}_{\text{n+ne}}}(t) = \hat{\mathbf{U}}_0(t). \quad (4.5)$$

Thus, if the Fourier transform of the electric field $\tilde{E}_0(\omega)$ is known analytically, we are able

to analytically compute $\hat{\mathbf{U}}_{\hat{\mathbf{V}}_{\text{e+int}}(t),p,I}(t_f, t_i)$ that represents the instantaneous insertion of the effect of the pulse.

If we use the electric field defined by Eq. (1.21), $\tilde{E}_0(\omega)$ becomes

$$\begin{aligned}\tilde{E}_0(\omega) &= \frac{\mathcal{N}E_0}{2\pi} e^{-i\omega t_m} \int_{\mathbb{R}} dt e^{-(t-t_m)^2/2\Delta t_{\text{pulse}}^2} \cos(\omega_{\text{pulse}} t + \varphi_{\text{pulse}}) e^{i\omega t} \\ &= \frac{E_0}{2\pi} \left[e^{-\Delta t_{\text{pulse}}^2 (\omega_{\text{pulse}} + \omega)^2 / 2 + i(\omega_{\text{pulse}} t_m + \varphi_{\text{pulse}})} + e^{-\Delta t_{\text{pulse}}^2 (\omega_{\text{pulse}} - \omega)^2 / 2 - i(\omega_{\text{pulse}} t_m + \varphi_{\text{pulse}})} \right].\end{aligned}\quad (4.6)$$

If, on top of that, we assume the resonant condition, i.e., $\omega_{\text{pulse}} = \omega$, then, two interesting cases are worth being discussed. First, we observe that, if $\Delta t_{\text{pulse}} \rightarrow \infty$, which can be understood as a continuous wave, Eq. (4.6) simplifies to

$$\lim_{\Delta t_{\text{pulse}} \rightarrow \infty} \tilde{E}_0(\omega) = \frac{E_0}{2\pi} e^{-i(\omega_{\text{pulse}} t_m + \varphi_{\text{pulse}})} \quad (4.7)$$

and applies only to the resonant state.

Second, in the case of $\Delta t_{\text{pulse}} \rightarrow 0$, which reflects a δ -pulse, we obtain

$$\lim_{\Delta t_{\text{pulse}} \rightarrow 0} \tilde{E}_0(\omega) = \frac{E_0}{\pi} \cos(\omega_{\text{pulse}} t_m + \varphi_{\text{pulse}}), \quad (4.8)$$

which applies to all electronic states.

4.1.2 δ -Pulse Approximation

In the δ -pulse approximation, we take the limit $\Delta t_{\text{pulse}} \rightarrow 0$. Assuming our Gaussian shape definition of the electric field, the δ -pulse evolution operator reads

$$\hat{\mathbf{U}}_{\delta\text{-pulse}}(t_f, t_i) := \hat{\mathbf{U}}_0(t_f - t_m) \left[\hat{\mathbf{1}} + \frac{2iE_0}{\hbar} \cos(\omega_{\text{pulse}} t_m + \varphi_{\text{pulse}}) \sum_{j,k=1}^S \hat{\mu}_{jk} |j\rangle \langle k| \right] \hat{\mathbf{U}}_0(t_m - t_i). \quad (4.9)$$

4.2 Results and Discussion

We apply our different methods, as in Sec. 2.3.3, to the three-state three-dimensional vibronic coupling model of pyrazine, but with different parameters that can be found in Ref. [124]. We assume the Condon approximation for the transition dipole moment. It is non-zero only for the $S_0 \rightarrow S_2$ transition and, for simplicity, set to unity. We choose the initial state to be the ground vibrational state of the electronic ground state; discretized, for each of the three modes, on a grid composed of 64 points equally spaced between -8 and 8 a_0 . We propagate it with electronic and nuclear time steps of 1 and 2 or 4 \hbar/E_h , respectively, by using a fourth-order split-operator algorithm generated from the recursive method developed by Yoshida [67]. We refer the reader to Appendix F for convergence with

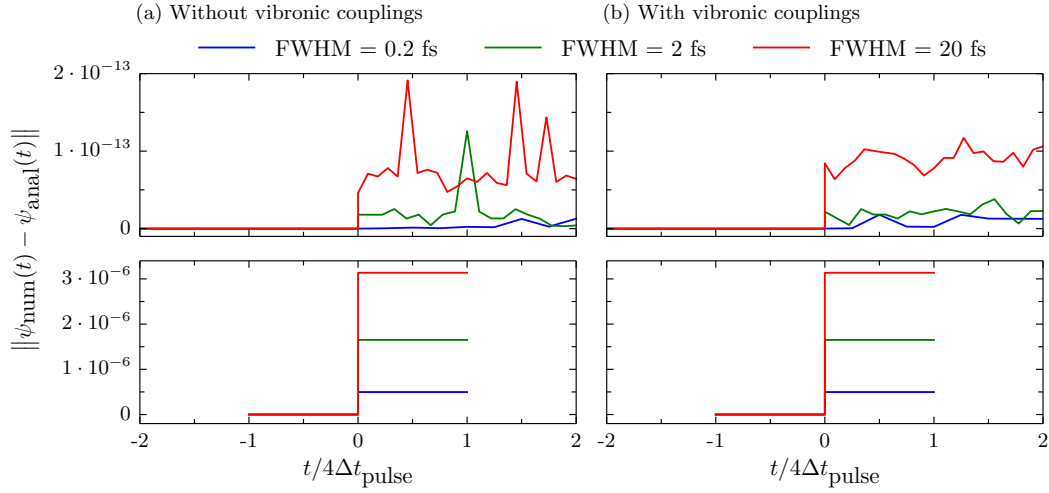


Figure 4.1 – Error between the analytical and numerical evaluations of the time-dependent perturbation theory and ultrashort-pulse approximation. (a): without vibronic couplings, (b): with vibronic couplings.

respect to grid density and to the time step. We use three different Gaussian envelopes with a full-width at half-maximum of 0.2, 2.0, and 20 fs for the electric field. They share the following parameters: $t_m = 0$, $E_0 = 0.05 E_h^2 / ea_0 \hbar$, $\varphi_{\text{pulse}} = 0$, and the carrier frequency ω_{pulse} is equal to the difference between the second electronic excited state energy at the position of the ground state equilibrium and the energy of the ground electronic state at the same position (vertical transition). This leads to an electronic period of motion T_e of approximately 1 fs, whereas the smallest nuclear period of motion T_n for this specific system is approximately 30 fs.

4.2.1 Comparison Between Analytical and Numerical Results for the Combination of Time-Dependent Perturbation Theory and Ultrashort-Pulse Approximation

We compare the analytical and numerical propagators of the combination of time-dependent perturbation theory and ultrashort-pulse approximation by computing the error of the difference between corresponding wavefunctions as a function of time. The results are depicted in Fig. 4.1 without and with vibronic couplings in panel (a) and (b), respectively. The lower panel assumes a numerical integration from $t_m - 4\Delta t_{\text{pulse}}$ to $t_m + 4\Delta t_{\text{pulse}}$, whereas the upper one assumes a numerical integration from $t_m - 8\Delta t_{\text{pulse}}$ to $t_m + 8\Delta t_{\text{pulse}}$.

We obtain an error of 10^{-6} when the pulse is assumed to be fully contained in $8\Delta t_{\text{pulse}}$ (lower panel of Fig. 4.1). As the error does not lie in the machine precision, the numerical integration must be problematic. We conclude that going from $t_m - 4\Delta t_{\text{pulse}}$ to $t_m + 4\Delta t_{\text{pulse}}$ is not sufficient to fully include the interaction with the laser field. When we assume that $16\Delta t_{\text{pulse}}$ fully contained the pulse (upper panel of Fig. 4.1), the machine precision is reached, which ensures that the wavefunctions computed from the numerical and analytical

propagators of the combined time-dependent perturbation theory and ultrashort-pulse approximation are similar. However, as a range of $16\Delta t_{\text{pulse}}$ leads to time consuming calculations and as an error of 10^{-6} will not be reflected in any observables, we keep a range of $8\Delta t_{\text{pulse}}$ when we numerically compute the interaction with the laser field. Nevertheless, we should emphasize that the analytical calculations are always preferable, first, because the pulse is automatically included from $-\infty$ to ∞ and second, due to a smaller computational cost.

Finally, we compare the population dynamics during excitation with ultrashort laser pulses computed with the ultrashort-pulse approximation and with the combination of time-dependent perturbation theory and ultrashort-pulse approximation (numerical and analytical). We depict the results in Fig. 4.2 without vibronic couplings in panel (a) and with vibronic couplings in panel (b). We observe that for each of the three different laser pulses, the populations obtained from the three propagation methods are overlapping, which proves that all three propagators converge to the same result.

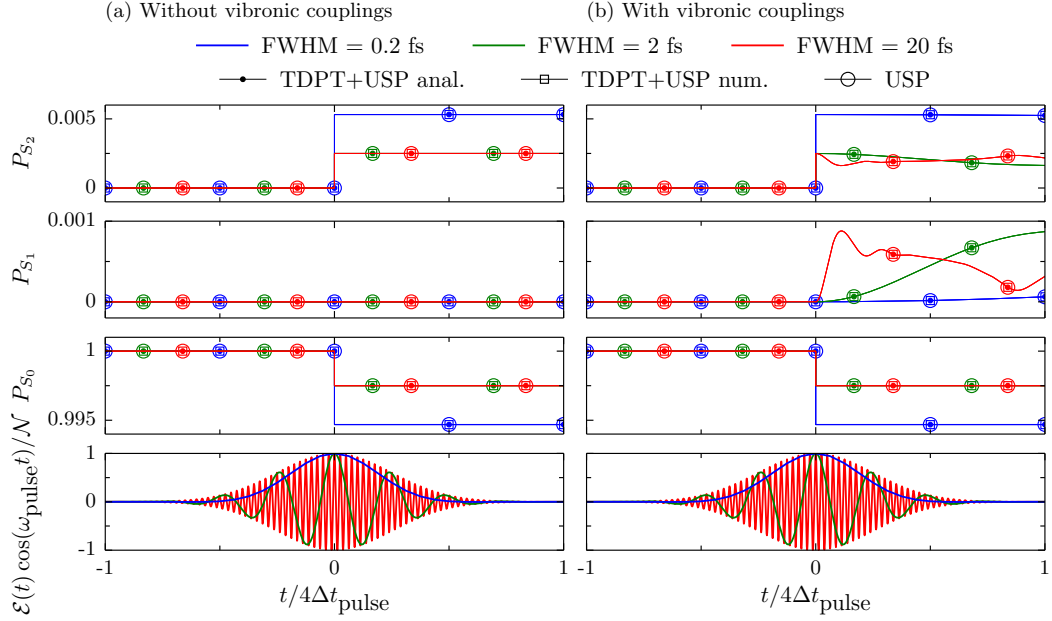


Figure 4.2 – Equivalence of the ultrashort-pulse approximation and the combination of the time-dependent perturbation theory and ultrashort-pulse approximation. (a): without vibronic couplings and (b): with vibronic couplings.

4.2.2 Population Dynamics

We compare the populations obtained from the time-dependent perturbation theory and ultrashort-pulse approximation and the δ -pulse approximation to the one obtained from the exact method during the vertical photoexcitation with ultrashort laser pulses in absence and in presence of vibronic couplings. Panel (a) of Fig. 4.3 depicts the unnormalized electric field, whereas panel (b) and (c) show the ground P_{S_0} and excited P_{S_1} and P_{S_2}

state populations without and with vibronic couplings, respectively.

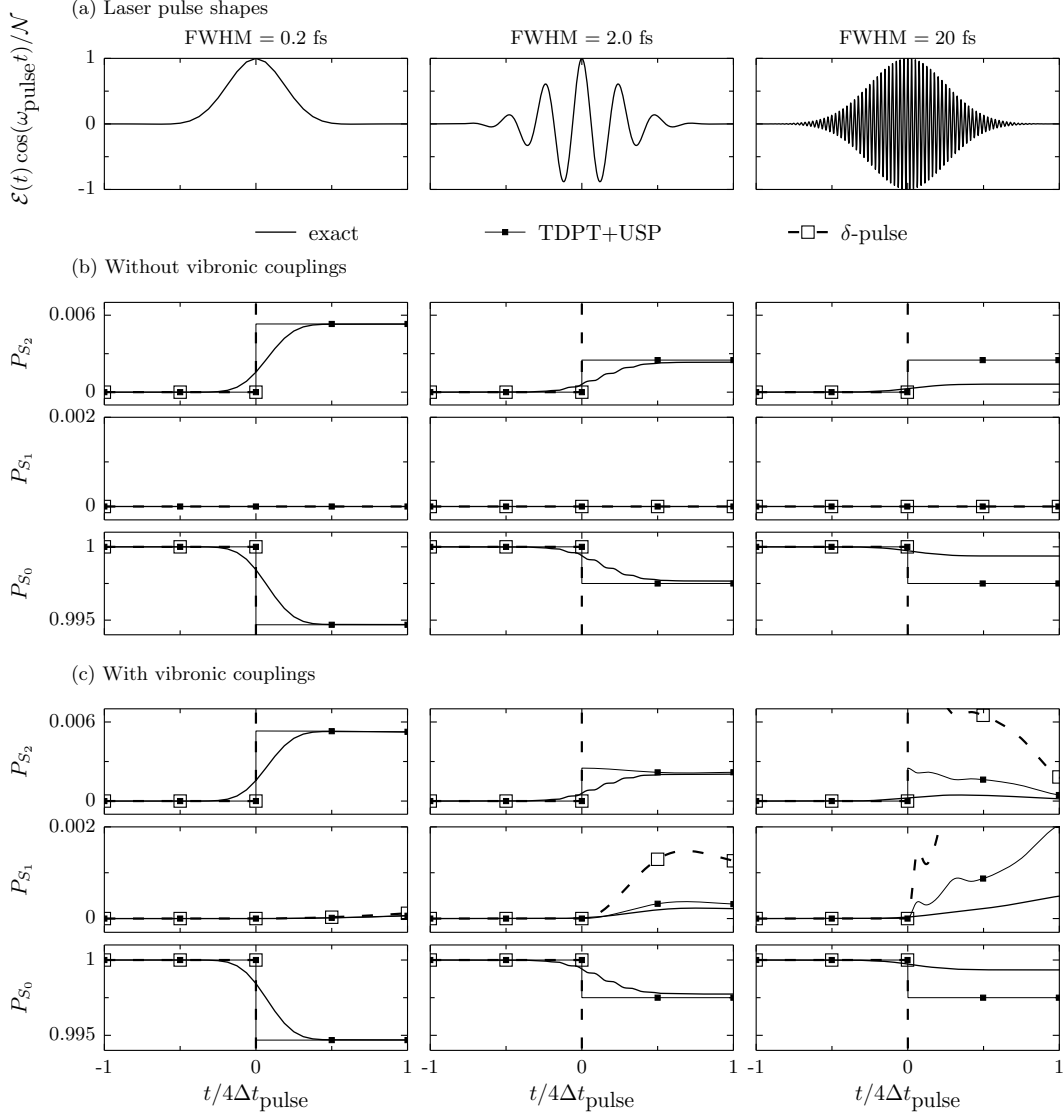


Figure 4.3 – Laser pulse shapes (a) and population dynamics obtained with the exact quantum calculation and with several level of approximations during the vertical photoexcitation with ultrashort laser pulses without vibronic couplings (b) and with vibronic couplings (c).

As given by Eq. (4.7), we observe a threshold in population transfer when using 2.0 or 20 fs full-width at half-maximum pulses ($\Delta t_{\text{pulse}} \rightarrow \infty$). Indeed, those two pulse lengths produce the same deexcitation of the ground state when the time-dependent perturbation theory and ultrashort-pulse approximation is used. In addition, we should comment on the shortest pulse (FWHM = 0.2 fs) depicted in Fig. 4.3 (a). It is also used by Stock, Schneider, and Domcke in Ref. [26]. As they mention, it is an unrealistic pulse. Indeed, such a pulse cannot propagate because its integral is non-zero [30]. The pulses with a FWHM of 0.2 and 2 fs are the two pulses for which the time-dependent perturbation theory and ultrashort-pulse approximation is able to reproduce perfectly the exact calculation

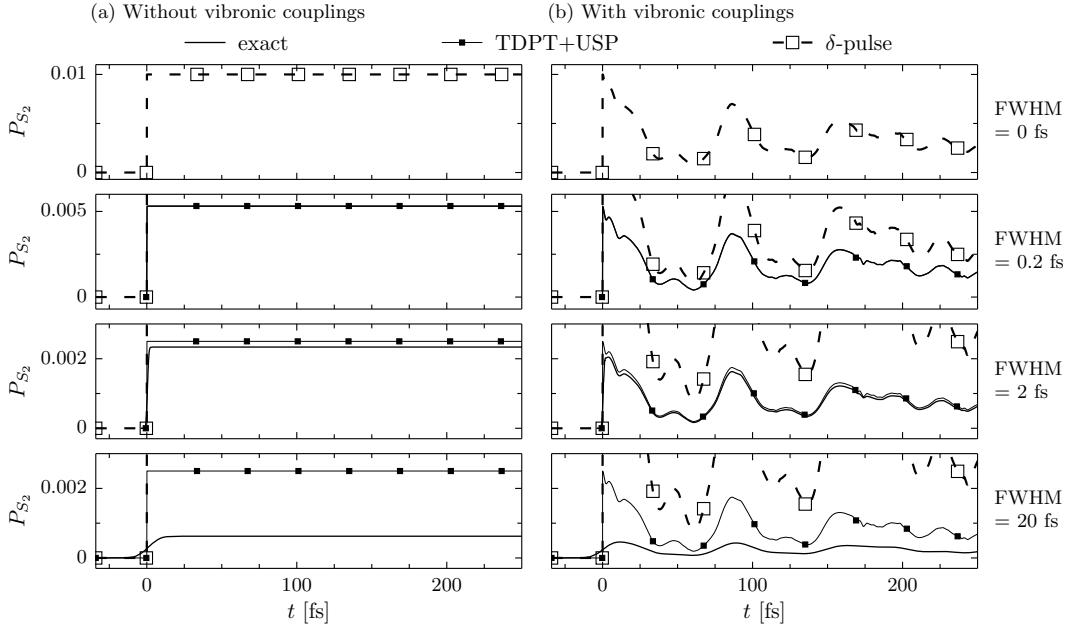


Figure 4.4 – Population dynamics on the second excited state obtained with the exact quantum calculation and with several level of approximations after the vertical photoexcitation with ultrashort laser pulses without vibronic couplings (a) and with vibronic couplings (b).

during the photoexcitation process. As for the third one (FWHM = 20 fs), we see a large difference with the exact result. Moreover, as a general trend, we observe a decrease of the population transfer with an increase of the pulse length.

We compare the same approximations to the exact method for 250 fs after the photoexcitation using the same three laser pulses. Note that the propagation is performed with the usual time-independent Hamiltonian and a nuclear time step after time $t_m + 4\Delta t_{\text{pulse}}$. Panel (a) of Fig. 4.4 depicts the second excited population without vibronic couplings, whereas panel (b) depicts it in presence of vibronic couplings.

We observe, first, that our δ -pulse approximation does not allow to obtain the right prefactor for the population transfer. However, the community is not interested in the magnitude of the photoexcitation process (the initial wavefunction is set to the excited state of interest and evolved). We point out that as they usually compute the absorption spectrum, the amplitude of the wavefunction produced on the excited state of interest does in principle not matter and will simply be reflected as an overall scaling of the spectrum. Second, we note that even though the δ -pulse approximation is not able to give the correct amount of population transfer, it produces a similar excited state population dynamics (oscillation pattern) as the one obtained with a resonant Gaussian pulse using the exact propagation scheme [131].

In addition, as mentioned in Refs. [28, 31], although the authors know that under the ultrashort-pulse approximation, the pulse length must be short compared to the nuclear time scale; for the specific system under study, they realize that such pulses are not

sufficiently small to guarantee the validity of the impulsive limit. Therefore, another criterion must exist for the validity of the ultrashort-pulse approximation. Indeed, the pulse length must be short compared to the time scale on which the vibronic couplings are occurring, if any. As for our pyrazine model under the excitation with an ideally short laser pulse in presence of vibronic couplings [panel (b) of Fig. 4.4], we observe that the second excited state population decays very fast in the first femtoseconds. It means that the nonadiabatic couplings are very important in the Franck-Condon region. Therefore, the impulsive limit cannot be valid with realistic pulses. Besides, we emphasize that the time-dependent perturbation theory and ultrashort-pulse approximation is, for our system under study (which reflects quite well most of the electronic and nuclear timescales of common molecules), perfectly working for unrealistic pulses and pulses which are on the edge of realization.

Finally, we note that when using the exact propagation, the longer the pulse duration, the smoother the second excited state population, which is obviously not captured by both the time-dependent perturbation theory and ultrashort pulse approximation and the δ -pulse approximations. In addition, the oscillation pattern is shifted to positive time for the exact calculation. This shift corresponds to the time it takes for the pulse to finish the photoexcitation transfer.

4.2.3 Error Analysis

In what follows, we compare the combination of time-dependent perturbation theory with ultrashort-pulse approximation, the δ -pulse approximation to the exact propagation scheme. To do so, we compute the error on the wavefunctions as a function of time with and without vibronic couplings and depict it in Fig. 4.5.

As already noticed from the population analysis, because the δ -pulse approximation is the crudest approximation, it gives the largest error. We observe that all curves have the same trend: they start with nil error, increase until a maximum at time zero, and then decrease to a given value (more or less close to zero depending of the accuracy of the approximation). Note that when using an approximate method, the time-dependent potential is included instantaneously with respect to the nuclear time scale at time zero, whereas for the exact propagation it is continuously inserted. Therefore, before time zero, the interaction with the field is missing for the approximate method and the error increases. Then, at time zero, the full interaction with the electric field is inserted, which leads to a further increase of the error. Finally, after time zero, the exact propagator includes continuously the missing interaction which in turns reduces the error present with respect to the approximate method.

Then, we report in Fig. 4.6 the error at the final time of the interaction ($t_m + 4\Delta t_{\text{pulse}}$) for the three different pulses. As for both panels, the error of the δ -pulse approximation increases with the length of the pulse, which reflects the fact that the longer the pulse, the worst the accuracy of the approximation. In the case of the time-dependent perturbation

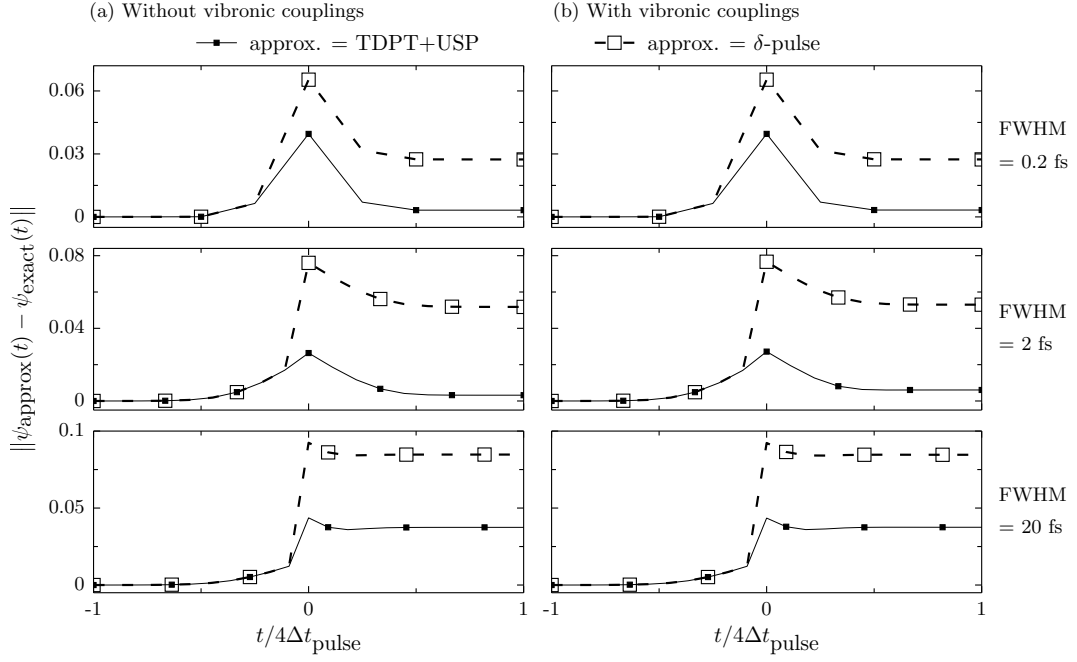


Figure 4.5 – Errors of various ultrashort-pulse approximations as a function of time. (a): without vibronic couplings, (b): with vibronic couplings.

theory and ultrashort-pulse approximation, the error stays approximately the same for the pulses with a FWHM of 0.2 and 2 fs, whereas the error grows for the 20 fs pulse, which demonstrates that the approximation is not valid for such pulse.

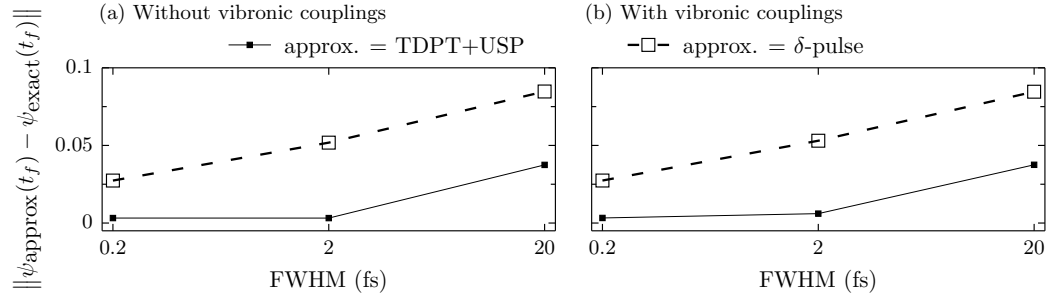


Figure 4.6 – Errors of various ultrashort-pulse approximations as a function of the pulse length. (a): without vibronic couplings, (b): with vibronic couplings.

5 Photodissociation of Iodomethane Following the Pump-Pulse Excitation to the A Band: Nonadiabatic Quantum Dynamical Study

Using the usual split-operator algorithm is straightforward when dealing with Cartesian coordinates. However, when studying a more realistic example, such as polyatomic photodissociation dynamics, internal coordinates are often more appropriate as they enable to lower the dimensionality of the system. But, they result in a more involved kinetic energy term. In this chapter, motivated by the experiments in the H.-J. Wörner group at ETH Zürich, we perform exact nonadiabatic quantum dynamics simulations of the photodissociation of iodomethane induced by a pump laser pulse. To do so, we modify the methodology of the previous chapter to non-Cartesian coordinates; and we implement a general split-operator algorithm with both discrete-variable and finite-basis representations that can treat one non-Cartesian, such as angular coordinate. In order to test the effect of various degrees of freedom and of the nonadiabatic dynamics, we apply these algorithms to one-, two-, and three-dimensional models of iodomethane, both in the presence and in the absence of nonadiabatic couplings. The results of this chapter can be partially found in Refs. [132] and [133].

5.1 Theoretical Model

5.1.1 Reduced Dimensionality Models

Exact nonadiabatic quantum dynamics simulations of the photodissociation process of iodomethane is performed using reduced dimensionality models. These models enable us to study systematically the importance of nonadiabatic dynamics and of various degrees

Chapter 5. Photodissociation of Iodomethane Following the Pump-Pulse Excitation to the A Band: Nonadiabatic Quantum Dynamical Study

of freedom in the dissociation process. Up to three active degrees of freedom have been used for the calculations and are represented by the Jacobi coordinates (R, r, θ) [134], as depicted in Fig. 5.1. R is the distance between the iodine atom and the center of mass of CH_3 , it denotes the dissociation coordinate. r represents the umbrella bend of the $\text{C}-\text{H}_3$ group: the CX distance, X being a pseudoatom located at the center of mass of the three H atoms. A reduction of the umbrella bend to a stretching mode is proven to be a good approximation [135–138]. θ is the Jacobi angle between R and r vectors that denotes the $\text{X}-\text{C}-\text{I}$ bend. Iodomethane is represented by a pseudo triatomic molecule. One- and two-dimensional models considered only the R and (R, r) coordinates, respectively, and discarded coordinates are held fixed at their equilibrium values.

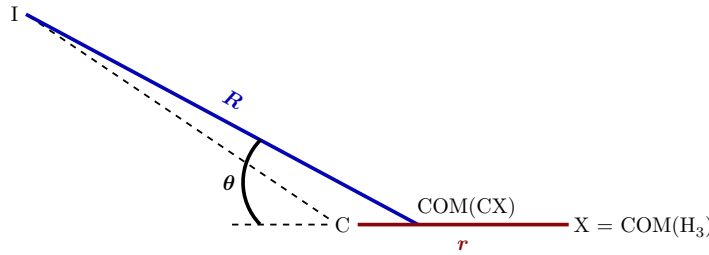


Figure 5.1 – Jacobi coordinates used in the three-dimensional model of iodomethane.

5.1.2 Kinetic Energy Operator

Kinetic energy operator defined by Eq. (1.5) requires Cartesian or normal mode coordinates. However, in this chapter, we are dealing with a set of internal coordinates, which makes the kinetic energy operator be different. Assuming zero total angular momentum, it reads for the three-dimensional model,

$$T_{R,r,\theta} = -\frac{\hbar^2}{2M_R R^2} \frac{\partial}{\partial R} R^2 \frac{\partial}{\partial R} - \frac{\hbar^2}{2M_r r^2} \frac{\partial}{\partial r} r^2 \frac{\partial}{\partial r} - \frac{\hbar^2}{2I} \frac{1}{\sin \theta} \frac{\partial}{\partial \theta} \sin \theta \frac{\partial}{\partial \theta}. \quad (5.1)$$

Full details about masses and moment of inertia are given in Ref. [134]. Briefly, M_R and M_r are the reduced masses for CH_3-I and $\text{C}-\text{H}_3$, respectively, i.e.,

$$M_R = \frac{m_I(m_C + 3m_H)}{m_I + m_C + 3m_H} \text{ and } M_r = \frac{3m_C m_H}{m_C + 3m_H}. \quad (5.2)$$

The moment of inertia is taken as [139]

$$\frac{1}{I} = \frac{1}{M_R R^2} + \frac{1}{I_{\text{CH}_3}}, \quad (5.3)$$

where I_{CH_3} is the perpendicular component of the total moment of inertia of CH_3 . The parallel component is ignored as proven by experimental facts [140–143].

5.1.3 Potential Energy Surfaces and Initial State

Our calculations require three electronic states: ground 1A_1 and excited $^3Q_{0+}$ and 1Q_1 states. We take the potential energy surfaces from the recent study of Evenhuis and Manthe [144]. The ground state potential is based on empirical potentials [135, 145] and on the ab initio CH_3 potential of Medvedev et al. [146]. We take the potential energy surfaces of the excited states from the full nine-dimensional coupled diabatic potential of Amatatsu et al. [147] and modified according to Ref. [148]. We reduce the dimensionality of the model to three dimensions by fixing extra coordinates to their equilibrium values. Vibronic couplings couple the excited electronic states $^3Q_{0+}$ and 1Q_1 . Due to the nature of the equation, the latter are non-zero only in the three-dimensional case. Moreover, the dynamics requires transition dipole moment couplings that are taken under the Condon approximation [41–44] and only non-zero and equal to unity between ground 1A_1 and excited $^3Q_{0+}$ electronic states.

We chose the initial wavefunction $|\psi(t_0)\rangle$ to be the ground vibrational state of the electronic ground state. In order to obtain it, we use a numerical procedure that is described in Sec. 5.2.2.

5.1.4 Analysis: Radial Distribution Function and Expectation Value

We obtain the radial distribution function of both radial R and stretching r coordinates of any given electronic state from the wavefunction at any time. It reads

$$\text{rdf}_n(x, t) = \int \int |\psi(x, y, \theta, t)|^2 x^2 \sin \theta d\theta dy \quad (5.4)$$

where $x = R$ and $y = r$ or vice versa.

We write the expectation value of any of the three degrees of freedom on a single surface as

$$\langle Q \rangle_n = \frac{\langle \psi_n | \hat{Q} | \psi_n \rangle}{P_n}, \quad (5.5)$$

where $P_n = \langle \psi_n | \psi_n \rangle$ represents the population of the electronic state n and Q is any of the R, r , and θ coordinates. Then, we give the expectation value of any of the three degrees of freedom over the full molecular state as

$$\langle Q \rangle = \langle \psi | \hat{Q} | \psi \rangle = \sum_{n=1}^S P_n \langle Q \rangle_n. \quad (5.6)$$

5.2 Numerical Implementation

5.2.1 Exact Propagation Applied to Iodomethane

We treat reduced dimensionality models of iodomethane using Jacobi coordinates. The kinetic energy operator Eq. (5.1) contains mixed terms (a product of the coordinate itself and its corresponding derivative, i.e.: Q and $\partial/\partial Q$), which implies that the split-operator algorithm cannot be applied in a straightforward way. Assuming the one-dimensional model and using the following transformation of the wavefunction

$$\phi(R, t) = R \psi(R, t) \quad (5.7)$$

enables us to obtain the following, hugely simplified, kinetic energy operator

$$\tilde{T}_R = -\frac{\hbar^2}{2M_R} \frac{\partial^2}{\partial R^2} = \frac{P_R^2}{2M_R}, \quad (5.8)$$

where $P_R = -i\hbar \frac{\partial}{\partial R}$ is the momentum operator conjugate to R . Thereby, the split-operator algorithm can be used. For the two-dimensional model, the split-operator algorithm is directly applicable when, first, $\phi(R, r, t) = R r \psi(R, r, t)$ is applied.

As for the three-dimensional model, we follow the work given in Ref. [134]. Assuming the splitting $\hat{\mathbf{H}}(t) = \hat{\mathbf{A}} + \hat{\mathbf{B}} + \hat{\mathbf{C}}(t)$, for small enough time step Δt , the evolution of the molecular state can be approximated to second-order [70, 149], as

$$\begin{aligned} \exp \left[-\frac{i}{\hbar} \int_t^{t+\Delta t} \hat{\mathbf{H}}(t') dt' \right] &= e^{-\frac{i}{2\hbar} \hat{\mathbf{A}} \Delta t} e^{-\frac{i}{\hbar} [\hat{\mathbf{B}} + \hat{\mathbf{C}}(t+\Delta t/2)] \Delta t} e^{-\frac{i}{2\hbar} \hat{\mathbf{A}} \Delta t} + \mathcal{O}(\Delta t^3) \\ &= e^{-\frac{i}{2\hbar} \hat{\mathbf{A}} \Delta t} e^{-\frac{i}{2\hbar} \hat{\mathbf{B}} \Delta t} e^{-\frac{i}{\hbar} \hat{\mathbf{C}}(t+\Delta t/2) \Delta t} e^{-\frac{i}{2\hbar} \hat{\mathbf{B}} \Delta t} e^{-\frac{i}{2\hbar} \hat{\mathbf{A}} \Delta t} + \mathcal{O}(\Delta t^3). \end{aligned} \quad (5.9)$$

Using the wavefunction transformation

$$\phi(R, r, \theta, t) = R r \psi(R, r, \theta, t) \quad (5.10)$$

enables us to obtain the following kinetic energy operator

$$\tilde{T}_{R,r,\theta} = \frac{P_R^2}{2M_R} + \frac{p_r^2}{2M_r} - \frac{\hbar^2}{2I} \frac{1}{\sin \theta} \frac{\partial}{\partial \theta} \sin \theta \frac{\partial}{\partial \theta} = \tilde{T}_R + \tilde{T}_r + T_\theta, \quad (5.11)$$

for which the last term still contains mixed terms. However, we can realize that T_θ is proportional to the angular momentum operator for which eigenfunctions and eigenvalues are well-known. Indeed,

$$\frac{\hat{L}^2}{2I} |P_j\rangle = \frac{\hbar^2}{2I} j(j+1) |P_j\rangle \quad (5.12)$$

Where $\langle \theta | P_j \rangle = P_j(\theta)$ is the j 's Legendre polynomial. An orthonormal basis is defined by

considering the full set of the renormalized polynomials given as

$$|\varphi_j\rangle = \left(\frac{2j+1}{2}\right)^{1/2} |P_j\rangle. \quad (5.13)$$

Knowing so, we can construct a unitary matrix $\mathbf{U} = U\mathbf{1}$ that enables us to transform from grid to basis representation in spirit similar to Fourier transforms, but for the angular kinetic energy term. Then, the split-operator algorithm as defined by Eq. (5.9) can be used directly with $\hat{A} = \hat{T}_R + \hat{T}_r$, $\hat{B} = \hat{T}_\theta$, and $\hat{\mathbf{C}}(t) = \hat{\mathbf{V}}(t)$. The U matrix performs nothing else than a diagonalization in grid representation of the angular momentum operator, i.e.,

$$e^{-\frac{i}{\hbar}T_\theta\Delta t} = U^\dagger \text{diag} \left[e^{-i\frac{\hbar}{2I}j(j+1)\Delta t} \right] U, \quad (5.14)$$

where we use the property $e^{U^\dagger XU} = U^\dagger e^X U$.

In order to construct the unitary matrix U , let us define a grid composed of N_θ nodes $\chi = \cos \theta$ [being the zeros of the Legendre polynomial $P_{N_\theta}(\chi)$] and the corresponding weights w from Gauss-Legendre quadrature. A matrix element is then given by

$$U_{j,k} = w_k^{1/2} \varphi_j(\chi_k) \quad (5.15)$$

where j goes from 0 to $N_\theta - 1$ and k from 1 to N_θ . This procedure, called discrete-variable representation (DVR), was first developed by Light et al. [150, 151].

The action of $\exp(-i\hat{T}_\theta\Delta t/\hbar)$ on the wavefunction $|\phi(t)\rangle$ is performed in three steps. First, we slightly modify the wavefunction $|\phi(t)\rangle$ to $|\phi_{\text{DVR}}(t)\rangle$ by using

$$\phi_{\text{DVR}}(R, r, \theta, t) = w^{1/2} \phi(R, r, \theta, t). \quad (5.16)$$

Secondly, we apply the evolution operator by using Eq. (5.14). Finally, we recover the original representation of the wavefunction via the inverse transform of Eq. (5.16). Note that numerically, we do not want to switch between $|\phi(t)\rangle$ and $|\phi_{\text{DVR}}(t)\rangle$ every single step. Thus, we do the transformation at initial time: $\phi_{\text{DVR}}(R, r, \theta, t_i) = w^{1/2} \phi(R, r, \theta, t_i)$ and invert it back at final time: $\phi(R, r, \theta, t_f) = w^{-1/2} \phi_{\text{DVR}}(R, r, \theta, t_f)$.

5.2.2 Numerical Evaluation of the Ground Vibrational State

As for all the calculations presented in this thesis, the initial state is taken as the ground vibrational state of the electronic ground state. We obtain it via diagonalization of the molecular Hamiltonian $\mathbf{H}_0(Q)$ by using discrete-variable representation. As usual, the potential energy is diagonal and the grid representation of \tilde{T}_R and \tilde{T}_r is given by the procedure defined by Colbert and Miller in Ref. [152]. Assuming the following one-dimensional kinetic energy operator in coordinate representation

$$T_Q = -\frac{\hbar^2}{2M_Q} \frac{\partial^2}{\partial Q^2}, \quad (5.17)$$

Chapter 5. Photodissociation of Iodomethane Following the Pump-Pulse Excitation to the A Band: Nonadiabatic Quantum Dynamical Study

considering an equidistant grid composed of N_Q points with $\Delta Q = (Q_{\max} - Q_{\min})/N_Q$ such that

$$Q_k = Q_{\min} + k\Delta Q, \quad k = 0, \dots, N_Q - 1, \quad (5.18)$$

and that the wavefunction vanishes at the endpoints, then, we obtain for a ‘‘Cartesian’’ coordinate ($-\infty < Q < \infty$)

$$T_{Q_{kk'}} = \frac{\hbar^2}{2M_Q\Delta Q^2}(-1)^{k-k'} \left\{ \begin{array}{ll} \frac{\pi^2}{3}, & k = k' \\ \frac{2}{(k-k')^2}, & k \neq k' \end{array} \right\}. \quad (5.19)$$

It is possible to prune the formula for a radial or polar coordinate, but we keep Eq. (5.19) for both \tilde{T}_R and \tilde{T}_r .

We construct the angular part of the kinetic energy similarly to Eq. (5.14)

$$T_\theta = U^\dagger \text{diag} \left[\frac{\hbar^2}{2I} j(j+1) \right] U, \quad (5.20)$$

where the transformation matrix U is defined in Eq. (5.15).

5.3 Results and Discussion

5.3.1 Computational Details

We apply the diagonalization procedure to the three different models and obtain the corresponding ground vibrational states and zero point energies. Coordinate grids used to compute the initial states are summarized in Table 5.1, together with the computed zero point energies.

Table 5.1 – Coordinate grids used to compute the ground vibrational state for one-, two-, and three-dimensional systems, together with computed zero point energies (ZPEs).

	N_R	$[R_{\min}, R_{\max}]$		N_r	$[r_{\min}, r_{\max}]$		N_θ	$[\theta_{\min}, \theta_{\max}]$	ZPE
		$[a_0]$			$[a_0]$			$[\text{rad}]$	$[E_h]$
1D	512	[2, 24]							0.0012
2D	100	[2, 6.296875]	64		[-2, 2]				0.0043
3D	68	[3, 5.5]	22		[-0.5, 1.7]	24		[0, π]	0.0080

Then, we perform exact quantum calculations by using the second-order split-operator algorithm from -120 to 120 fs. Time and grid parameters are given in Table 5.2. We use an explicit laser pulse with parameters listed in Table 5.3. Note that in order to have a fair comparison between our different models, we shift the one- and two-dimensional ground electronic states in such a way that the lowest vibrational energy levels have the same absolute value as the three-dimensional ones.

Table 5.2 – Time and grid parameters used to perform the exact quantum dynamics of the one-, two-, and three-dimensional systems.

	N_{steps}	Δt [\hbar/E_h]	N_R	$[R_{\min}, R_{\max}]$ [a_0]	N_r	$[r_{\min}, r_{\max}]$ [a_0]	N_θ	$[\theta_{\min}, \theta_{\max}]$ [rad]
1D	10000	1	512	[2, 24]				
2D	5000	2	512	[2, 24]	64	[-2, 2]		
3D	5000	2	600	[1.5, 24]	40	[-2, 2]	24	[0, π]

Table 5.3 – Parameters of the laser pulse.

E_0 [$E_h^2/ea_0\hbar$]	$\vec{\epsilon}$	t_m [fs]	ω_{pulse} [nm]	Δt_{pulse} [fs]	φ_{pulse}
2.1	(1,0,0)	0	267	30	0

5.3.2 Population Dynamics

We compute for the three different models with and without nonadiabatic couplings (NACs/NoNACs) the exact propagation under the influence of the electric laser pulse. We depict the corresponding population dynamics in Fig. 5.2. We observe that the one-dimensional model has a depopulation of 25% and that the extra degrees of freedom decelerate the population transfer, until 20% for the three-dimensional model. Moreover, when using nonadiabatic couplings, which are only non-zero in the three-dimensional case, there are some differences, especially the population of a new state, the 1Q_1 excited state.

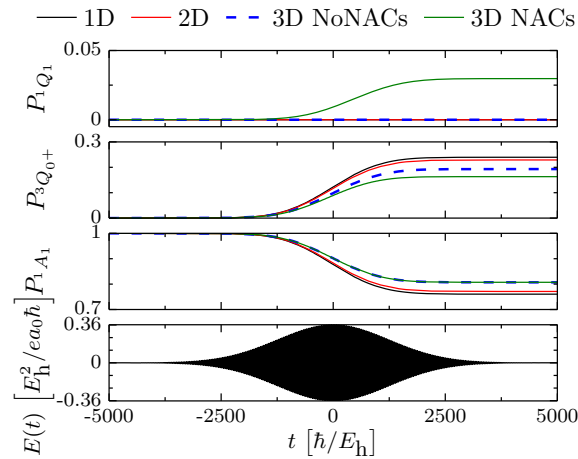


Figure 5.2 – Populations dynamics of iodomethane following the excitation by a pump pulse for the one-, two-, and three-dimensional systems with and without nonadiabatic couplings.

5.3.3 Radial Distribution Function of Several Jacobi Coordinates

We compute the radial distribution functions of dissociative R and stretching r coordinates for the three-dimensional model in presence of nonadiabatic couplings, as given by Eq. (5.4), and depict them in Fig. 5.3, at several times of the dynamics. In both cases, as the initial state is the ground vibrational state of the electronic ground state, the radial distribution function on the ground surface does not move but simply decreases in amplitude. This is due to the interaction of ground and excited $^3Q_{0+}$ states via electromagnetic field, which transfers part of the wavepacket to the excited surface. As for the excited states, we observe a spreading of the wavepacket while it moves on the surfaces. Indeed, in the case of the dissociative coordinate, the wavepacket slides toward large internuclear distance R , which means that iodomethane is being dissociated. As for the stretching mode r , the wavepacket moves toward a zero value of the bond length. Radial distribution functions of the excited states indicate that the dissociation of CH_3I has taken place and that we are left with two fragments: the iodine atom and a planar CH_3 .

We also compute the radial distribution function of the Jacobi angle θ . We observe, for the excited states, a spreading around $\theta = 0$.

5.3.4 Expectation Value of Several Jacobi Coordinates

We compute the expectation value of dissociative bond length R , stretching coordinate r , and Jacobi angle θ for the three different models in absence and in presence of nonadiabatic couplings. We present the results in panels (a), (b), and (c) of Fig. 5.4, respectively. As for panel (a), we observe that in the ground state, the bond length almost remains constant. Small oscillations indicate that the wavefunction is no longer an eigenstate of the full Hamiltonian. As for the excited states, the expectation value of the bond length increases with time indicating that the molecule is being dissociated. The average performed over all states (top panel) is the same, on one hand, for one- and two-dimensional models and, on the other hand, for three-dimensional model with and without nonadiabatic couplings. Therefore, we say that only the action of the angular coordinate θ changes slightly the photodissociation time scale. As for panel (b), we do the same observations for the ground state, i.e., there are small oscillations around the mean value. As for the excited states, the expectation value of r goes to zero, which tells us that the CH_3 fragment becomes planar during the photodissociation. The average over all states (top panel) is slightly different between two- and three-dimensional models, which brings us to the same conclusion as in (a). Finally, as for panel (c), we observe that the ground state expectation value stays constant but that excited states ones increase. The reason for the latter is the broadening of the excited wavepackets which makes more probability for θ to have larger values. This is also reflected in the expectation value over all states (top panel).

We conclude that neither the stretching coordinate nor the nonadiabatic couplings affect the dissociation time scale. It is rather the action of the angular coordinate that slightly changes this time scale.

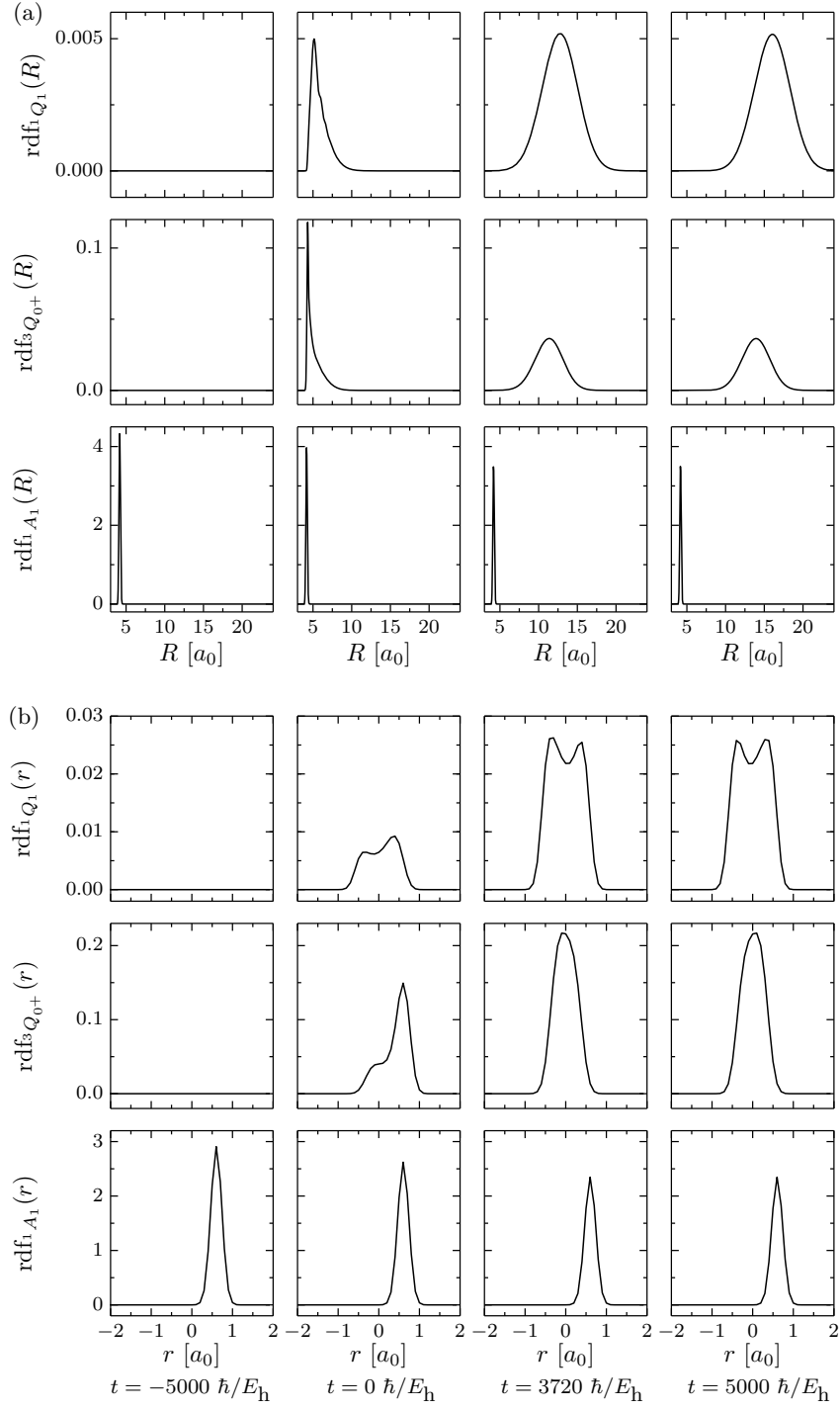


Figure 5.3 – Radial distribution of (a) the dissociative bond length R and (b) the stretching r coordinates at several times of the dynamics for the three-dimensional system in presence of nonadiabatic couplings.

Chapter 5. Photodissociation of Iodomethane Following the Pump-Pulse Excitation to the A Band: Nonadiabatic Quantum Dynamical Study

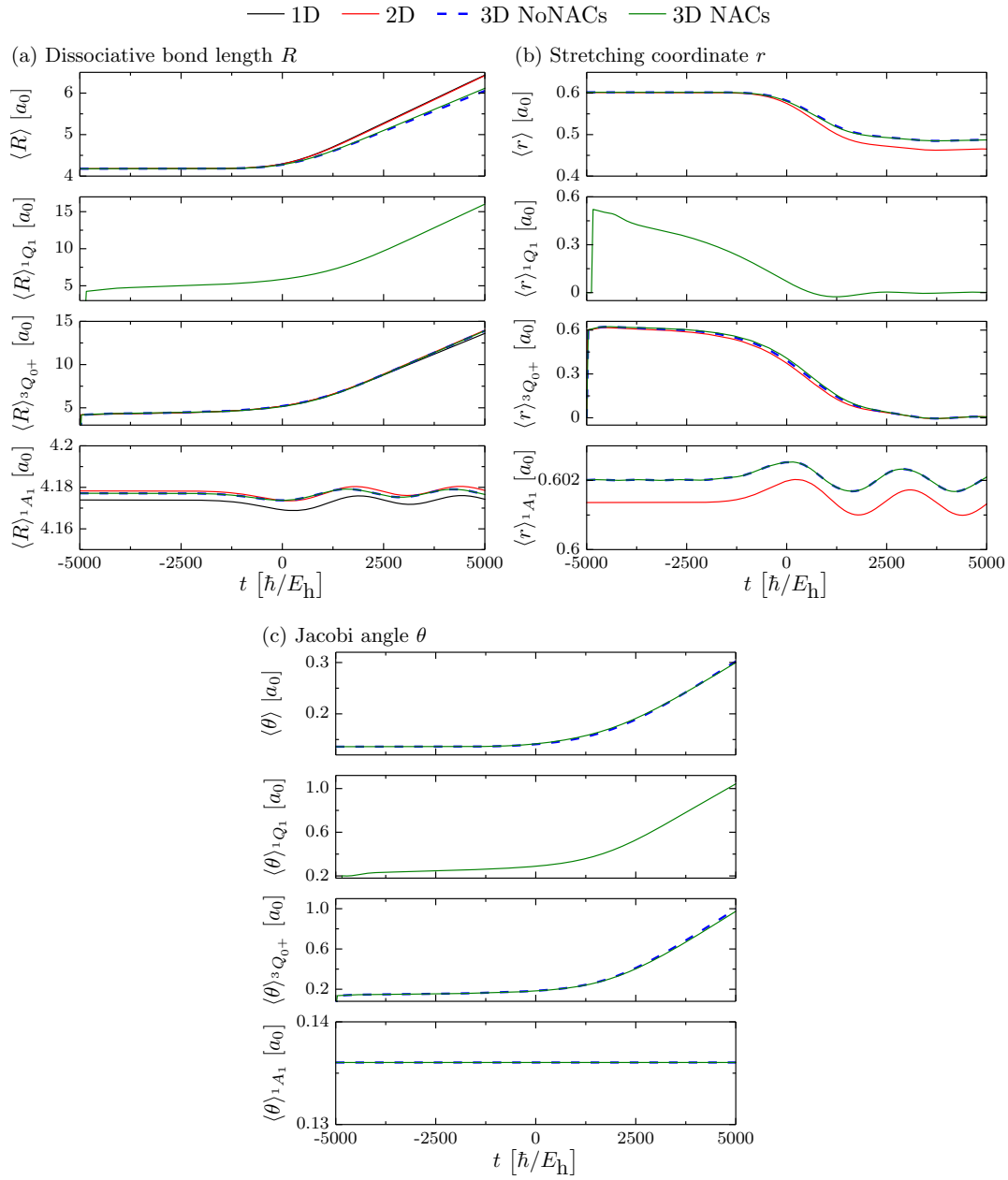


Figure 5.4 – (a) Dissociative bond length R , (b) stretching coordinate r , and (c) Jacobi angle θ in the ground (1A_1) and two excited ($^3Q_{0+}$ and 1Q_1) states as a function of time for the one-, two-, and three-dimensional systems with and without nonadiabatic couplings.

6 On-the-fly Ab Initio Semiclassical Evaluation of Absorption Spectra of Polyatomic Molecules beyond the Condon Approximation

Neither the high-order split-operator/Magnus integrator, nor any of the physical approximations that have been defined in the previous chapters can overcome the exponential scaling of the computational cost with dimensionality; full quantum calculations are limited to approximately ten degrees of freedom. Beyond this, one must seek an affordable balance between computational efficiency and physical accuracy and we can employ, for example, semiclassical methods that are based on classical trajectories. A good example is the on-the-fly ab initio thawed Gaussian approximation, a semiclassical algorithm that requires only local knowledge of the potential. It is suited only for short-time dynamics but, due to the ultrafast character of the dynamics, this is of less importance. We implement the thawed Gaussian approximation by using geometric integrators. The numerical integration of the classical equations of motion is carried out using a symplectic algorithm, and the norm of the wavefunction is exactly preserved. In addition, the thawed Gaussian approximation goes beyond the global harmonic approximation and captures, at least partially, the anharmonicity of the studied system. In this chapter, we focus on the computation of absorption cross sections within the Herzberg-Teller approximation, which extends the Condon approximation by allowing a linear dependence of the transition dipole moment on nuclear coordinates. To do so, we implement a generalization of the on-the-fly ab initio thawed Gaussian approximation and test it by calculating the $\tilde{A}^2B_1 \leftarrow \tilde{X}^2A_1$ absorption spectrum of phenyl radical and $1^1B_{2u} \leftarrow 1^1A_{1g}$ absorption spectrum of benzene, for which the Franck-Condon approximation fails completely. The new approach improves older absorption cross sections computed within the Franck-Condon approximation and also gives much better results than those obtained via global harmonic approximations. The results of this chapter can be found in Ref. [153].

6.1 Theory

6.1.1 Generalized Thawed Gaussian Approximation

In this chapter, we assume a single electronic state and the following Hamiltonian

$$\hat{H}_0 = \hat{T} + \hat{V}_0. \quad (6.1)$$

It is composed of the nuclear kinetic energy operator \hat{T} and the molecular potential energy operator \hat{V}_0 .

Heller's thawed Gaussian approximation [111–113] is based on the fact that the time evolution of a Gaussian wavepacket in at most quadratic potential does not perturb its functional form. Within the thawed Gaussian approximation, a part of the anharmonicity of the potential is taken into account by guiding the center of a Gaussian wavepacket that uses a classical trajectory, whereas a time-dependent local harmonic approximation of the full potential

$$V_{\text{eff}}(q, t) = V_0|_{q_t} + (\text{grad}_q V_0|_{q_t})^T \cdot (q - q_t) + \frac{1}{2}(q - q_t)^T \cdot \text{Hess}_q V_0|_{q_t} \cdot (q - q_t), \quad (6.2)$$

is used to propagate the width. In the previous equation, $V_0|_{q_t}$, $\text{grad}_q V_0|_{q_t}$, and $\text{Hess}_q V_0|_{q_t}$ denote the potential energy, gradient, and Hessian evaluated at the center of the Gaussian. The evolving wavepacket is assumed in the form

$$\psi(q, t) = \langle q | \psi(t) \rangle = \langle q | \hat{U}(t) | \psi(0) \rangle \quad (6.3)$$

$$= N_0 \exp \left\{ -(q - q_t)^T \cdot A_t \cdot (q - q_t) + \frac{i}{\hbar} \left[p_t^T \cdot (q - q_t) + \gamma_t \right] \right\}, \quad (6.4)$$

where $\hat{U}(t) = e^{-i\hat{H}_0 t/\hbar}$ is the time evolution operator of the Hamiltonian, N_0 is a time-independent normalization constant, (q_t, p_t) is the phase-space coordinate of the center of the Gaussian wavepacket, A_t is a complex symmetric width matrix, and γ_t is a complex number for which its real part gives an overall phase factor and its imaginary part ensures the normalization of the Gaussian wavepacket for all time $t \geq 0$. Heller's equations of motion read [111–113]

$$\dot{q}_t = \frac{\partial H_0}{\partial p_t} = M^{-1} \cdot p_t \quad (6.5)$$

$$\dot{p}_t = -\frac{\partial H_0}{\partial q_t} = -\text{grad}_q V_0|_{q_t} \quad (6.6)$$

$$\dot{A}_t = -2i\hbar A_t \cdot M^{-1} \cdot A_t + \frac{i}{2\hbar} \text{Hess}_q V_0|_{q_t} \quad (6.7)$$

$$\dot{\gamma}_t = L_t - \hbar^2 \text{Tr} \left[M^{-1} \cdot A_t \right], \quad (6.8)$$

where H_0 is the Hamiltonian for a given electronic state, M is the mass matrix, and L denotes the Lagrangian dual to H_0 . Numerical integration of classical equations of motion is carried out in a symplectic fashion [114]. It is straightforward to obtain numerical

solutions q_t and p_t of the classical equations of motion. However, numerical solutions of the width and the phase of the wavepacket become complicated. In order to propagate the width matrix A_t of the Gaussian, we use what Lee and Heller proposed in Ref. [113]. The idea is to introduce two matrices P_t and Z_t such that

$$A_t = \frac{1}{2i\hbar} P_t \cdot Z_t^{-1} \quad (6.9)$$

$$\dot{Z}_t = M^{-1} \cdot P_t. \quad (6.10)$$

The unique solutions are

$$\begin{pmatrix} P_t \\ Z_t \end{pmatrix} = \begin{bmatrix} \left(\frac{\partial p_t}{\partial p_0} \right)_{q_0} & \left(\frac{\partial p_t}{\partial q_0} \right)_{p_0} \\ \left(\frac{\partial q_t}{\partial p_0} \right)_{q_0} & \left(\frac{\partial q_t}{\partial q_0} \right)_{p_0} \end{bmatrix} \begin{pmatrix} P_0 \\ Z_0 \end{pmatrix}, \quad (6.11)$$

with initial condition $Z_0 = 1$ and $P_0 = 2i\hbar A_0$.

The complex phase is given by

$$\gamma_t = S_t + \frac{i\hbar}{2} \ln(\det Z_t) + \gamma_0, \quad (6.12)$$

where S_t is the classical action and we assume $\gamma_0 = 0$. As Z_t is a complex matrix, in order to make γ_t continuous, the proper branch of the natural logarithm has to be taken.

We discuss the propagation of an initial state being a polynomial multiplied by a Gaussian, which is a straightforward extension of the thawed Gaussian approximation. As mentioned in Ref. [113], for a polynomial $P^{(n)}$ of order n in $(\hat{q} - q_0)$ and the initial Gaussian state $\langle q | \psi(0) \rangle = \psi(q, 0)$, the following condition holds:

$$\Psi^{(n)}(q, 0) = \langle q | P^{(n)}(\hat{q} - q_0) | \psi(0) \rangle = P^{(n)} \left(\frac{\hbar}{i} \frac{\partial}{\partial p_0} \right) \psi(q, 0). \quad (6.13)$$

Applying the time evolution operator to the previous equation yields

$$\Psi^{(n)}(q, t) = \langle q | \hat{U}(t) | \Psi^{(n)}(0) \rangle = \langle q | \hat{U}(t) P^{(n)}(\hat{q} - q_0) | \psi(0) \rangle = P^{(n)} \left(\frac{\hbar}{i} \frac{\partial}{\partial p_0} \right) \psi(q, t), \quad (6.14)$$

where, in the last step, we use the fact that within local harmonic approximation

$$\left[P^{(n)} \left(\frac{\hbar}{i} \frac{\partial}{\partial p_0} \right), \hat{U}(t) \right] = 0. \quad (6.15)$$

Therefore, in order to generate $\Psi^{(n)}(q, t)$, all the necessary information is already available from the propagation of the Gaussian wavepacket $\psi(q, 0)$ that uses the usual thawed Gaussian approximation. Note that Eq. (6.15) is valid due to the local harmonic approximation of the potential energy surface. The extended thawed Gaussian approximation can be used for propagating vibrationally excited states of a harmonic potential, for Gaussian wavepackets that follow excitation beyond Condon approximation, i.e., when a Taylor

Chapter 6. On-the-fly Ab Initio Semiclassical Evaluation of Absorption Spectra of Polyatomic Molecules beyond the Condon Approximation

expansion of the transition dipole moment is needed, and even for a combination of those two cases.

In this chapter, we focus on the calculation of absorption spectra by using the Herzberg-Teller approximation [154], which is a perfect application of this extension. Indeed, in such case, the initial state is given by the product of a first-order polynomial (the transition dipole moment in the Herzberg-Teller approximation) and a Gaussian wavepacket. Keeping a general notation and defining $P^{(1)}(q - q_0) = a + b^T \cdot (q - q_0)$, the evolved initial wavepacket $\Psi^{(1)}(q, t)$ reads

$$\Psi^{(1)}(q, t) = \left[a + \frac{\hbar}{i} b^T \cdot \frac{\partial}{\partial p_0} \right] \psi(q, t) = \left[a + b_t^T \cdot (q - q_t) \right] \psi(q, t), \quad (6.16)$$

$$b_t^T = b^T \cdot \left[-2i\hbar \left(\frac{\partial q_t}{\partial p_0} \right)^T \cdot A_t + \left(\frac{\partial p_t}{\partial p_0} \right)^T \right]. \quad (6.17)$$

6.1.2 On-the-fly Ab Initio Thawed Gaussian Approximation within Herzberg-Teller Approximation

As thawed Gaussian approximation requires propagating only a single trajectory, it proves to be very useful in implementation with on-the-fly ab initio dynamics [114, 115]. Instead of computing energy, gradient, and Hessian present in Eq. (6.2) from an analytical potential energy surface, these quantities are now provided by ab initio electronic structure calculations. However, ab initio packages typically perform calculations by using Cartesian coordinates. Therefore, the geometry, gradient, and Hessian must be transformed to the coordinate system q that fits into our framework [115]. An appropriate choice of coordinates for propagating the Gaussian wavepacket are the vibrational normal modes.

Assuming a system composed of N atoms and ξ_{ref} being the vector that contains the $3N$ Cartesian reference structure geometry, we transform a general Cartesian configuration ξ into the $3N$ normal modes q about ξ_{ref} by using

$$q = O^T \cdot m^{1/2} \cdot (\xi - \xi_{\text{ref}}), \quad (6.18)$$

where m is the $3N \times 3N$ diagonal mass matrix and O is the $3N \times 3N$ orthogonal matrix diagonalizing the mass-scaled Cartesian Hessian $m^{-1/2} \cdot \text{Hess}_\xi V_0|_{\xi_{\text{ref}}} \cdot m^{-1/2}$ evaluated at ξ_{ref} . However, six degrees of freedom (three translations and three rotations) with zero frequencies are still present in q . In order to remove them [114, 115], first, translational degrees of freedom are suppressed. To do so, we shift the configuration ξ to the center of mass frame ξ' by shifting each atom a using $\xi'_a := \xi_a - \xi_{\text{COM}}$, where ξ_{COM} is the position of the center of mass in Cartesian coordinates. Note that we assume the center of mass of ξ_{ref} to be already at the origin. Then, we minimize the rovibrational couplings by rotating each ξ_a to the Eckart frame [155]: $\xi''_a := r \cdot \xi'_a$. We obtain the 3×3 rotation matrix r by minimizing the distance in mass-scaled coordinates between ξ'' and ξ_{ref} [156–158]. Finally, we apply Eq. (6.18) to ξ'' using the $3N \times (3N - 6)$ submatrix L which drops the translational

and rotational degrees of freedom contained in O . The geometry, gradient, and Hessian transformations from Cartesian ξ to $3N - 6$ vibrational normal mode coordinates q read

$$q = L^T \cdot m^{1/2} \cdot [R \cdot \xi' - \xi_{\text{ref}}] \quad (6.19)$$

$$\text{grad}_q V_0 = \text{grad}_\xi V_0 \cdot R^T \cdot m^{-1/2} \cdot L \quad (6.20)$$

$$\text{Hess}_q V_0 = L^T \cdot m^{-1/2} \cdot R \cdot \text{Hess}_\xi V_0 \cdot R^T \cdot m^{-1/2} \cdot L, \quad (6.21)$$

where R is a $3N \times 3N$ block diagonal matrix composed of N matrices r .

We can also use an ab initio electronic structure code to compute the transition dipole moment. In the Herzberg-Teller approximation, it reads

$$\vec{\mu}_{eg}(q) := \vec{\mu}_{eg}(q_0) + \left(\text{grad}_q \vec{\mu}_{eg} |_{q_0} \right)^T \cdot (q - q_0). \quad (6.22)$$

Although ab initio calculations of excited state properties enable us to obtain the zeroth-order term, the first-order one is, in general, not included in standard packages. But, two different approaches are available to obtain it. The first one uses a finite difference scheme [159]. Note that the first-order terms of the transition dipole moment must be transformed from Cartesian to normal mode coordinates and we achieve this by using Eq. (6.20). The second one is based on the following identity [160]

$$\partial_j \vec{\mu}_{eg} |_{q_{j_l}} = - \sum_k \langle e | \partial_j k \rangle |_{q_{j_l}} \vec{\mu}_{kg}(q_{j_l}), \quad (6.23)$$

where ∂_j denotes the partial derivative, with respect to normal mode q_j , and is evaluated at position q_{j_l} .

6.1.3 Global Harmonic Approximation

When computing electronic spectra, the crude but popular global harmonic approximation is frequently used. In such case, the potential energy surface of interest is approximated globally by using ab initio data computed either (1) at the equilibrium geometry of that state [161]: adiabatic harmonic approximation or (2) at the equilibrium geometry of the state from which energy is absorbed/emitted [162]: vertical harmonic approximation. Even though efficient and exact algorithms exist to treat even large molecules [162–164], we use the thawed Gaussian approximation algorithm in order to evaluate the global harmonic spectra because it, too, is exact in a global quadratic potential energy surface.

The multidimensional harmonic oscillator of the potential energy surface of interest reads

$$V_{\text{harm}}(q) = \frac{1}{2} (q - d)^T \cdot K \cdot (q - d) + V_{\text{min}}, \quad (6.24)$$

where K , d , and V_{min} denote its force matrix, displacement, and minimum energy, respec-

Chapter 6. On-the-fly Ab Initio Semiclassical Evaluation of Absorption Spectra of Polyatomic Molecules beyond the Condon Approximation

tively, which are given by

$$K = \text{Hess}_q V_0|_{q_j} \quad (6.25)$$

$$d = - \left(\text{Hess}_q V_0|_{q_j} \right)^{-1} \cdot \text{grad}_q V_0|_{q_j} + q_j \quad (6.26)$$

$$V_{\min} = V_0|_{q_j} - \frac{1}{2} (d - q_j)^T \cdot \text{Hess}_q V_0|_{q_j} \cdot (d - q_j). \quad (6.27)$$

Energy $V_0|_{q_j}$, gradient $\text{grad}_q V_0|_{q_j}$, and Hessian $\text{Hess}_q V_0|_{q_j}$, are the results of ab initio calculations computed at the Cartesian geometry ξ_j and transformed to normal mode coordinates q_j using Eq. (6.19).

6.2 Computational Details

We perform all ab initio calculations using GAUSSIAN09 [165] electronic structure package. We use density functional theory and time-dependent density functional theory with the B3LYP functional and the 6-31+G(d,p) basis set for ground and excited states, respectively. We use an in-house code for running on-the-fly ab initio classical dynamics to compute the trajectories for both phenyl radical and benzene with a time step of 8 a.u. (≈ 0.2 fs). We then compute Hessians at every fourth step of the trajectory. We use 3000 and 10^4 steps to run the on-the-fly ab initio trajectories in the case of phenyl radical and benzene, respectively.

We compute the gradient of the transition dipole moment using the first-order finite difference scheme with a displacement step of 10^{-2} and 10^{-4} Å for phenyl radical and benzene, respectively. We choose the initial Gaussian wavepacket to be the ground vibrational state of the harmonic fit to the ground electronic state.

We shift and scale the resulting absorption cross sections according to the highest peak of the experimental spectra. In addition, we damp the spectra by a Gaussian broadening with half-width at half-maximum of 100 cm^{-1} for phenyl radical and by a cosine squared function [$\Gamma(t) = \cos^2(\frac{\pi t}{2T})$, where T is the total time for which the correlation function is computed] for benzene. Note that the cosine squared function is exactly zero at time $t = T$, and it preserves most of the autocorrelation function for $t < T$.

6.3 Results and Discussion

We present the calculated absorption spectra for both phenyl radical and benzene in the following section. The results include a comparison between Franck-Condon and Franck-Condon Herzberg-Teller spectra computed using the on-the-fly ab initio thawed Gaussian approximation, adiabatic-harmonic and vertical-harmonic approaches. We compare each calculated spectrum to the experimental one.

6.3.1 Absorption Spectrum of Phenyl Radical

The work of Porter and Ward [166] presents early spectroscopic data of phenyl radical. They describe the double-headed progression present in the spectrum and interpret the transitions in terms of two different vibrational frequencies. In this thesis, we use as a reference the latest, to our knowledge, absorption spectrum of phenyl radical, reported by Radziszewski [167].

The calculation of the absorption spectrum $\tilde{A}^2B_1 \leftarrow \tilde{X}^2A_1$ of phenyl radical depends on the dimensionality of the model, the inclusion of the Herzberg-Teller contribution, and the inclusion of anharmonicity. As for previous theoretical studies, Kim et al. [168] use a limited-dimensionality harmonic model and analytical calculations of the Franck-Condon factors within the Condon approximation but did not include mode-mixing in the excited state, i.e., the Duschinsky effect [169], to compute the absorption cross section. Biczysko et al. [170] achieved a much better agreement with experiment by using the Herzberg-Teller approximation in a full-dimensional global harmonic model which accounts for the Duschinsky effect. A further improvement was presented by replacing the calculated harmonic frequencies with scaled anharmonic frequencies, which partially includes anharmonicity [170, 171]. Our full dimensionality model enables us to include all these effects, in particular mode-mixing, Herzberg-Teller contribution, and anharmonicity; and it provides means to evaluate their importance.

In order to evaluate the influence of different effects on the absorption spectrum, we compare the experimental spectrum [167] to the simulated spectra by using the global harmonic approaches (with Franck-Condon and Franck-Condon Herzberg-Teller approximations) [see Fig. 6.1 panels (b) and (c)]. While the vertical harmonic completely fails to reproduce the experimental spectrum, the adiabatic harmonic is able to reproduce the main features of the spectrum. This is in contrast to previous findings where a better agreement with the experiment was obtained by using the vertical harmonic approximation [114, 115]. Here, the failure lies in the incorrect description of the frequencies and the displacements of the two most displaced modes ν_{18} and ν_{24} by the vertical Hessian. Indeed, when using the adiabatic Hessian, the frequencies of these two modes notably differ, which leads to the double-headed progression observed in the experiment. The vertical Hessian overestimates the frequency that corresponds to the mode ν_{18} and underestimates the one of ν_{24} , which results in a situation where one of the frequencies is approximately (within the resolution of the spectrum) double of the other. Consequently, the spectrum shows a single progression that is closer to the lower frequency, and the higher frequency peaks are hidden in this progression. These interesting observations are described by the missing mode effect [172]. When the resolution of the spectrum is not good enough, it is possible to obtain a progression whose spacings do not correspond to any of the frequencies of the system. We refer the reader to Appendix G.1 for ground and excited state optimized geometries and frequencies of phenyl radical.

As for the Franck-Condon and Franck-Condon Herzberg-Teller spectra computed with the

Chapter 6. On-the-fly Ab Initio Semiclassical Evaluation of Absorption Spectra of Polyatomic Molecules beyond the Condon Approximation

on-the-fly ab initio thawed Gaussian approximation [see Fig. 6.1 panel (a)], the problem of guessing which excited state Hessian to use—vertical or adiabatic—is overcome. Although the spectra resemble the adiabatic harmonic ones, the intensities and positions of the peaks are improved, especially in the higher frequency region. In comparison with the methodology used in Ref. [171] (global harmonic approximation and scaled anharmonic frequencies), the results are similar in terms of the positions of the peaks, but the intensities are better described by the on-the-fly ab initio approach.

To measure the importance of going beyond the Condon approximation, we compare Franck-Condon and Franck-Condon Herzberg-Teller spectra (See Fig. 6.1). The absorption spectra are mostly determined by the symmetry-allowed Franck-Condon transition, whereas the Herzberg-Teller contribution only slightly broadens the peaks. Although the Herzberg-Teller contribution is stressed in the literature as being large and significant [170, 171], our results are in contrast to those findings. Indeed, including anharmonicity effects through the use of the on-the-fly ab initio scheme is more important than the Herzberg-Teller contribution.

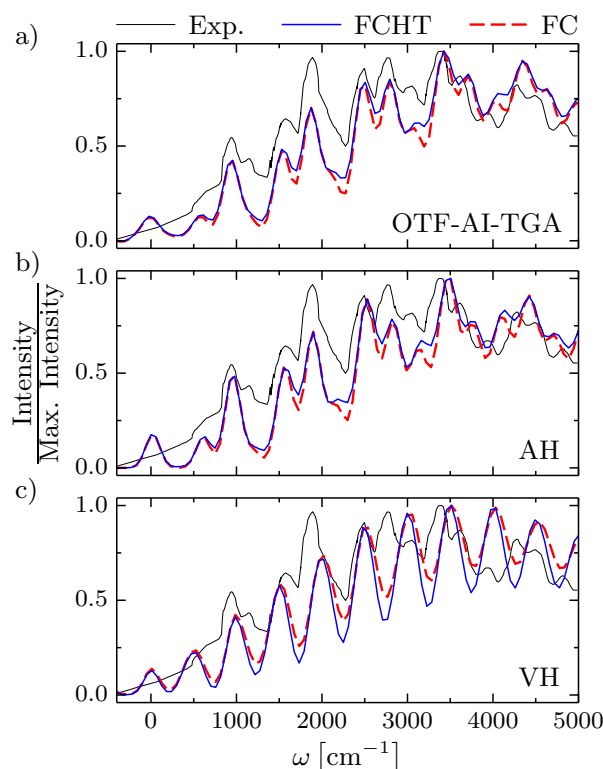


Figure 6.1 – Comparison between the experimental, Franck-Condon (FC), and Franck-Condon Herzberg-Teller (FCHT) spectra calculated by (a) on-the-fly ab initio thawed Gaussian approximation (OTF-AI-TGA), (b) adiabatic harmonic (AH) approximation, and (c) vertical harmonic (VH) approximation.

6.3.2 Absorption Spectrum of Benzene

As for benzene, both ground 1^1A_{1g} and excited 1^1B_{2u} states geometries belong to D_{6h} point group, and group theory predicts that the $1^1B_{2u} \leftarrow 1^1A_{1g}$ transition is symmetry-forbidden. Therefore, no spectrum can be obtained by the usual Franck-Condon approach. However, we can imagine simulating a “Franck-Condon” spectrum by blindly setting the transition dipole moment to unity. Whereas we cannot obtain absolute values of the absorption cross sections, we can compare this spectrum to the Franck-Condon Herzberg-Teller one, which enables us to evaluate the importance of the Herzberg-Teller contribution. In addition, the electronic transition is vibronically allowed as it exists non-zero x and y components of the gradient of the transition dipole moment, which originates from nonadiabatic couplings between 1^1B_{2u} and bright 1^1E_{1u} states [173].

The symmetry-forbidden $1^1B_{2u} \leftarrow 1^1A_{1g}$ transition of benzene constitutes the key example of the Herzberg-Teller spectrum because of its simple and straightforward interpretation [40, 174–176]. Herzberg [174] discusses the main progression in terms of a totally symmetric ring-breathing vibration. The work of Li et al. [173] presents the effect of including the undisplaced distorted modes using the global harmonic model without Duschinsky rotation, which enables us to reproduce the shape of the experimental absorption cross section. However, the relative intensities of the main progression peaks do not agree completely with the experimental data. In addition, Li et al. give a nice discussion on the computation of the first-order correction to the transition dipole moment by using the theoretical approach based on Eq. (6.23).

We depict the comparison between experimental and “Franck-Condon” and Franck-Condon Herzberg-Teller absorption spectra calculated by on-the-fly ab initio thawed Gaussian approximation, adiabatic harmonic approximation, and vertical harmonic approximation in panel (a), (b), and (c) of Fig. 6.2, respectively. We refer the reader to Appendix G.2 for ground and excited states optimized geometries and frequencies of benzene.

In contrast with phenyl radical, the absorption spectrum of benzene is considered not to be significantly affected by anharmonicity or mode-mixing [173]. Previous assignments of the peaks based on the global harmonic model identify three modes that contribute to the formation of a strong progression [173]: two degenerate ones, undisplaced and Herzberg-Teller actives (ν_{27} and ν_{28}) and a displaced totally symmetric one that gives rise to the main progression (ν_{20}). According to Table G.4, only modes ν_1 (totally symmetric stretches known as the beat mode, i.e., symmetric C–H stretch) and ν_{20} (breathing mode, i.e., ring stretch) could contribute to the phase-space dynamics, these modes are the only two displaced modes in the excited state. But, due to the much larger relative displacement of ν_{20} , it turns out that it is the only significant mode and that all the others do not show any classical dynamics. In addition, the absorption spectrum contains a number of hot bands. In this thesis, we do not attempt to simulate the hot bands, rather we focus on a precise computation of the main progression.

Chapter 6. On-the-fly Ab Initio Semiclassical Evaluation of Absorption Spectra of Polyatomic Molecules beyond the Condon Approximation

When we compare the two global harmonic approaches, we observe that the adiabatic harmonic approach reproduces the experimental spectrum better than the vertical one. The spectrum obtained from the vertical approach shows a number of peaks that are not observed in the experimental absorption cross section, which is due to the fact that the frequencies of the undisplaced modes ν_{25} , ν_{29} , and ν_{30} are significantly lower than the frequencies of the same modes computed with the adiabatic harmonic model, thus making those three modes more distorted.

Large distortions of the low-frequency peaks correspond to $2\nu \leftarrow 0$ ($\nu = 1, 2, \dots$). Indeed, within global harmonic approximation and for undisplaced distorted modes, when starting from the ground vibrational state (even character) of the electronic ground state, only transitions to even vibrational states of excited electronic state are allowed, i.e., transition to odd vibrational wavefunctions in the excited state gives rise to zero overlap [177, 178]. The final vertical harmonic spectrum is a convolution between the main progression and the spectrum of these three distorted modes. The spectrum shows the peaks of the main progression, followed by additional bands that are not present in the experimental spectrum.

As for the on-the-fly approach, the classical dynamics, i.e., the dynamics of the center of the wavepacket in phase space (position and momentum), is determined by the on-the-fly ab initio computation of the gradient of the potential, whereas in the case of global harmonic methods, it depends solely on the Hessian and the displacement of the excited state potential. However, even if the differences in the classical dynamics can have a strong effect on the resulting spectrum, both in terms of positions and intensities of the peaks, in the case of benzene, they are negligible and do not influence it. Therefore, the differences in the spectra can only be explained by considering the width matrix that is obtained through the calculation of Hessian.

The vertical and adiabatic approaches use a single Hessian to propagate the wavepacket, whereas the on-the-fly scheme enables the Hessian to change along the trajectory. If we focus on the ν_{20} mode, it means that with the on-the-fly ab initio scheme, the stiffness of this mode along the trajectory varies in time, i.e., the frequency of that mode (ω_{20}) is time-dependent. It turns out that the computed vertical and adiabatic frequencies correspond approximately to maximum and average values of the time-dependent on-the-fly frequency (see Fig. 6.3).

The phase-space classical dynamics is not affected by the time-dependence of the frequency of ν_{20} (the anharmonicity does not play a role), hence the spacings between the peaks are given by the average value of ω_{20} . This is why adiabatic harmonic and on-the-fly ab initio schemes give similar values of the spacing between the peaks. Nevertheless, these spacings do not match exactly with experimental data. This error can be assigned to the ab initio method, implying that the use of a better density functional or basis set could correct it. In this work, we recognise the importance of using a more appropriate ab initio method, but do not pursue the goal of finding it.

In addition, we observe that the intensities of the peaks from the adiabatic harmonic and

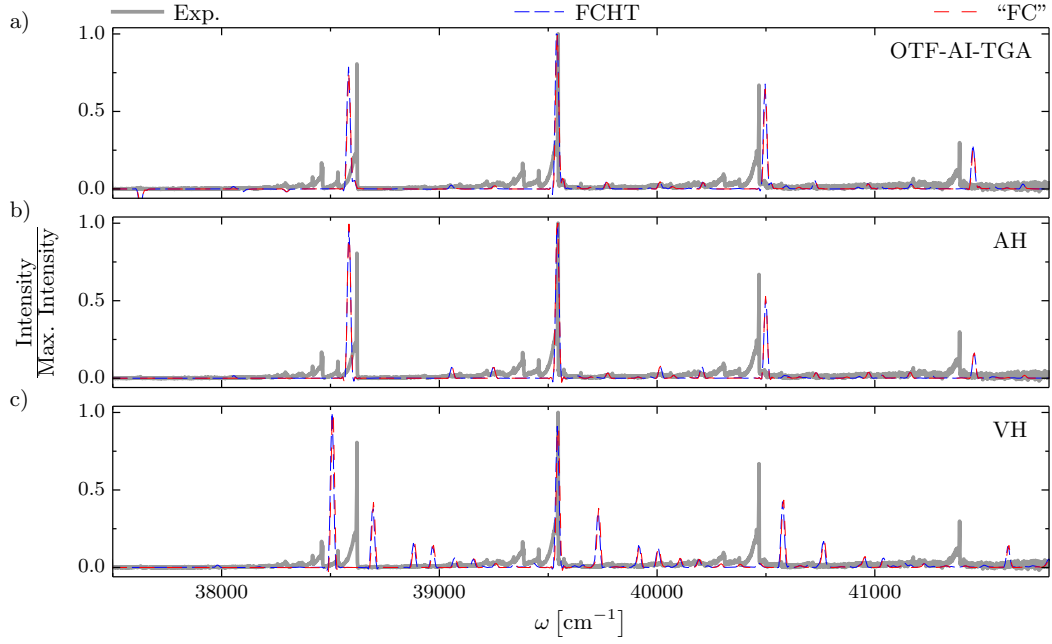


Figure 6.2 – Comparison between the experimental, “Franck-Condon” (“FC”), and Franck-Condon Herzberg-Teller (FCHT) spectra calculated by (a) on-the-fly ab initio thawed Gaussian approximation (OTF-AI-TGA), (b) adiabatic harmonic (AH) approximation, and (c) vertical harmonic (VH) approximation.

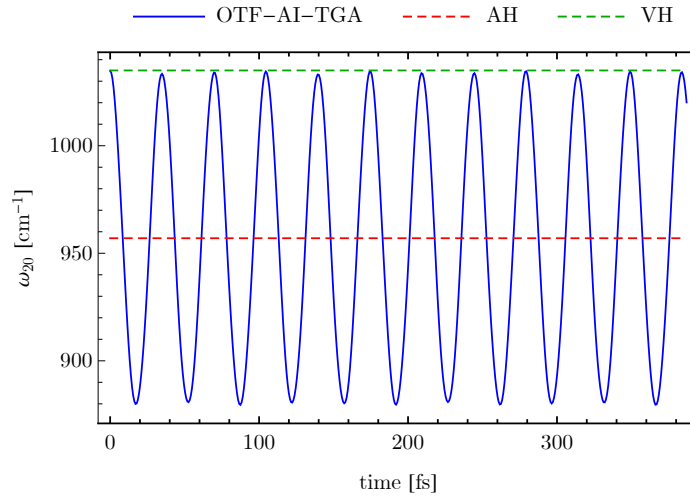


Figure 6.3 – Time-dependence of the frequency of the mode ν_{20} in the excited electronic state for the on-the-fly ab initio thawed Gaussian approximation (OTF-AI-TGA), and the adiabatic (AH) and vertical (VH) global harmonic approximations.

Chapter 6. On-the-fly Ab Initio Semiclassical Evaluation of Absorption Spectra of Polyatomic Molecules beyond the Condon Approximation

on-the-fly schemes differ and are due to differences in the phase of the correlation function (in time domain). Although the time between recurrences is mostly determined by classical dynamics (similar for global harmonic and on-the-fly methods), the width of a recurrence is given by the width of the wavepacket when it returns to the Franck-Condon region. The relative intensities cannot be described by a simple global harmonic approach but require a method that can treat anharmonicity. The agreement with the experimental spectrum proves that running an on-the-fly trajectory with computing Hessians along the trajectory gives a reliable wavepacket propagation and accounts for fine details in the correlation function.

Finally, we observe that when both the “Franck-Condon” and Franck-Condon Herzberg-Teller spectra are normalized and shifted according to the highest peak, there is no significant difference between them. However, if the correct vertical excitation energy could be obtained (using the experimental value or a very accurate electronic structure), the “Franck-Condon” approach would not yield correct results. Moreover, it is not able to reproduce the absolute values of the absorption cross sections.

As for the Franck-Condon Herzberg-Teller approach, it provides an estimate of the absolute absorption cross sections (see Fig. 6.4). The values strongly depend on the magnitude of the gradient of the transition dipole moment that is not very accurate when computed via finite-difference. Nevertheless, results agree within one order of magnitude and show the importance of going beyond the Condon approximation. As expected, as the zeroth-order transition dipole moment is nil, the Franck-Condon spectrum does not have any features.

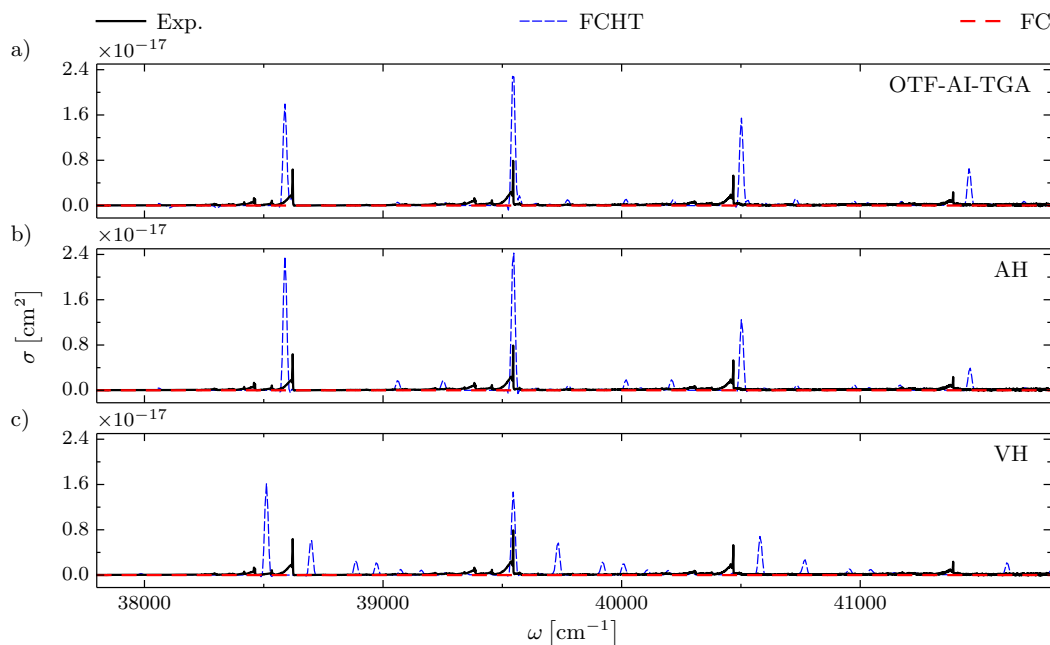


Figure 6.4 – Comparison between the experimental, Franck-Condon (FC), and Franck-Condon Herzberg-Teller (FCHT) spectra calculated by (a) on-the-fly ab initio thawed Gaussian approximation (OTF-AI-TGA), (b) adiabatic harmonic (AH) approximation, and (c) vertical harmonic (VH) approximation.

7 Conclusion and Outlook

In this thesis, we have implemented geometric integrators for the exact nonadiabatic quantum dynamics of a molecule that interacts with a time-dependent electromagnetic field, and we have derived and implemented such geometric integrators for the time-dependent perturbation theory, the Condon, rotating-wave, and ultrashort-pulse approximations, as well as every possible combination of these basic approximations. Due to the modular implementation, we were also able to observe the effect of each approximation independently. Moreover, we have derived dimensionless parameters, allowing us to predict the validity, or breakdown, of each basic approximation.

Using two- and three-state one-dimensional harmonic systems, we have shown that, under specific conditions, the approximations can be very powerful because of their accuracy compared to the exact propagation scheme. However, each approximation has its own limitations, yet, the validity of a given approximation can be predicted beforehand via its corresponding dimensionless parameter. In addition, we have applied several combinations of approximations to the more realistic three-dimensional three-state vibronic coupling model of pyrazine and have shown that it can lead to very accurate results assuming that the underlying approximations are in their regimes of validity.

The different methods have been implemented by using a combination of the split-operator algorithm and Magnus expansion. We have used a one-dimensional two-state harmonic system to show that these methods exactly preserve the geometric invariants, and achieve an arbitrary prescribed order of accuracy in the time step and an exponential convergence in the grid spacing. Despite the increased cost of a single numerical step, and thanks to the possibility of using a larger time step, the higher-order integrators can accelerate the calculations by several orders of magnitude over the standard second-order split-operator (if high numerical accuracy is sought).

We have also rigorously derived the widely used and surprisingly accurate δ -pulse approximation, including the right normalization factor. Furthermore, we have shown that it can be, in specific cases, important to go beyond this approximation. Indeed, in the case of the three-dimensional three-state model of pyrazine, this approximation qualitatively, but

not quantitatively, reproduces the overall nonadiabatic dynamics. However, as we have discussed, for most of the applications that involve computation of spectra, the well-known δ -pulse approximation is sufficient, even without taking into account its normalization factor.

We have also modified our geometric integrators of arbitrary order of accuracy so that they can treat Jacobi coordinates. Indeed, we have implemented a general split-operator algorithm with both discrete-variable and finite-basis representations that can deal with the problematic angular coordinate. Thereby, we have studied the effects of various degrees of freedom and of the nonadiabatic couplings on the photodissociation of iodomethane induced by a femtosecond pump pulse.

We conclude that under the influence of a laser pulse, two- and three-dimensional calculations, compared to one-dimensional one, decelerate the population transfer. Moreover, nonadiabatic couplings lead to the population of another excited state. We have observed that neither the stretching coordinate nor the nonadiabatic couplings affect the dissociation time scale. It is rather the action of the angular coordinate that slightly changes this time scale.

Finally, in order to study higher-dimensional systems, we have used the semiclassical thawed Gaussian approximation. We have employed a Herzberg-Teller extension to the on-the-fly ab initio thawed Gaussian approximation to simulate the absorption spectra of phenyl radical and benzene, in which the absorption is electronically forbidden but vibronically allowed. This achieves considerable improvements, compared to the usual global harmonic approaches, and we have gained further insight into the origins of the spectral features.

The results obtained for the absorption spectrum of phenyl radical are in contrast to the previously published works [170, 171], which asserted the significance of the Herzberg-Teller contribution. Indeed, we have found that including anharmonicity effects through the use of the on-the-fly ab initio scheme is more important than the Herzberg-Teller contribution.

Although the on-the-fly ab initio thawed Gaussian approximation method was previously described in the context of low-resolution spectra calculations, here we have reported a simulation of a much more resolved absorption spectrum of benzene with surprising accuracy.

From the point of view of theoretical spectroscopy, it is clear that the on-the-fly ab initio approach is more computationally involved, compared to the global harmonic methods. However, this approach enables us to learn about the dynamics on the excited state potential energy surface beyond the global harmonic approximation.

To summarize, we have focused on the development of geometric integrators with high numerical accuracy for the exact treatment as well as for several approximations of the molecule-field interaction. It enables us to completely remove any possible source of error

that is coming from the numerical algorithms and to specifically focus on the accuracy of the physical approximations themselves.

A possible extension of the work presented in this thesis would be combining our code with the use of sparse grids, which has already proven to be useful for solving the time-dependent Schrödinger equation [179, 180], in order to extend the number of degrees of freedom that can be treated quantum mechanically and thus slightly lower the exponential wall of quantum dynamics. In addition, one could extend the presented formulas for dynamics to expressions for experimental observables such as linear or even time-resolved spectra for each of the basic approximations and every possible combination. Therefore, a direct comparison with the experimental spectra would be possible. With these functionalities in place, our general code may become a useful practical benchmark tool both for theorists and experimentalists.

A Derivation of the Interaction Potential within the Electric-Dipole Approximation

The Hamiltonian of a molecule is defined as

$$\hat{H} = \hat{T}_n + \hat{T}_e + \hat{V}, \quad (\text{A.1})$$

where \hat{T}_n is the kinetic energy operator for nuclei, \hat{V} is the Coulomb potential, and

$$\hat{T}_e = \sum_{j=1}^{N_e} \frac{\hat{\vec{p}}_j^2}{2m_e} \quad (\text{A.2})$$

is the kinetic energy operator for N_e electrons with mass m_e . In this appendix, we use hats for nuclear as well as electronic operators and the arrow refers to three-dimensional vectors.

In order to take into account the interaction with electromagnetic field, Hamiltonian and electronic momentum are modified according to Lorentz force as

$$\hat{H} \rightarrow \hat{H} + e\Phi', \quad (\text{A.3})$$

$$\hat{\vec{p}} \rightarrow \hat{\vec{p}} - e\vec{A}'(\hat{\vec{q}}, t), \quad (\text{A.4})$$

where e , \vec{A}' , and Φ' are the electron charge, the vector potential, and the scalar potential, respectively. Due to the fact that masses of nuclei are much larger than the ones of electrons, their interactions with the electric field are much smaller than the ones of the electrons and can thus be neglected, i.e., in a molecule undergoing electronic excitation, there is no need to modify the kinetic energy of the nuclei but only the one of electrons.

Therefore, the Hamiltonian becomes, assuming a single electron for simplicity,

$$\hat{H} = \hat{T}_n + \frac{1}{2m_e} \left[\hat{\vec{p}} - e\vec{A}'(\hat{\vec{q}}, t) \right]^2 + \hat{V} + e\Phi', \quad (\text{A.5})$$

Derivation of the Interaction Potential within the Electric-Dipole Approximation

where the second term of the right hand side can be rewritten as

$$\hat{T}_e + \frac{1}{2m_e} \left[-e \hat{\vec{p}} \cdot \vec{A}'(\hat{\vec{q}}, t) - e \vec{A}'(\hat{\vec{q}}, t) \cdot \hat{\vec{p}} + e^2 \vec{A}'^2(\hat{\vec{q}}, t) \right]. \quad (\text{A.6})$$

Let us now define the gauge transformation

$$\begin{aligned} \Phi' &= \Phi - \dot{\Gamma}(t), \\ \vec{A}'(t) &= \vec{A}(t) + \vec{\nabla}\Gamma(t). \end{aligned}$$

In addition, assuming the following form of $\vec{A}(\hat{\vec{q}}, t)$

$$\vec{A}(\hat{\vec{q}}, t) = -\vec{\epsilon} A_0 e^{i\vec{k} \cdot \hat{\vec{q}}} \sin(\omega_{\text{pulse}} t)$$

and using the long-wavelength approximation, i.e., $\lambda = 2\pi/|\vec{k}| \gg r$, where r denotes the characteristic length of the molecule, the exponential term can be Taylor expanded and truncated to zeroth-order, $\exp(\pm i\vec{k} \cdot \hat{\vec{q}}) = 1 \pm i\vec{k} \cdot \hat{\vec{q}} + \dots \approx 1$, which is known as the dipole approximation. Then, we have

$$\vec{A}(t) = -\vec{\epsilon} A_0 \sin(\omega_{\text{pulse}} t), \quad (\text{A.7})$$

which is no longer a function of positions. Moreover, the Hamiltonian becomes

$$\hat{H} = \hat{T}_n + \hat{T}_e - \frac{e}{2m_e} \left[\hat{\vec{p}} \cdot (\vec{A} + \vec{\nabla}\Gamma) + (\vec{A} + \vec{\nabla}\Gamma) \cdot \hat{\vec{p}} \right] + \frac{e^2}{2m_e} (\vec{A} + \vec{\nabla}\Gamma)^2 + \hat{V} + e (\Phi - \dot{\Gamma}).$$

Choosing

$$\begin{aligned} \Gamma(\hat{\vec{q}}, t) &= -\vec{A}(t) \cdot \hat{\vec{q}}, \\ \vec{\nabla}\Gamma &= -\vec{A}(t), \end{aligned}$$

and using the gauge invariance of the electric field, i.e., $\vec{E}(t) = -\vec{\nabla}\Phi - \dot{\vec{A}}(t) = -\vec{\nabla}\Phi' - \dot{\vec{A}}'(t)$, and the Coulomb gauge

$$\begin{aligned} \vec{\nabla} \cdot \vec{A} &= 0, \\ \Phi &= 0, \end{aligned}$$

which leads to $\vec{\nabla}\Phi = 0$, enables us to obtain the length-gauge Hamiltonian

$$\hat{H} = \hat{T}_n + \hat{T}_e + \hat{V} - \vec{\mu} \cdot \vec{E}(t), \quad (\text{A.8})$$

where the dipole moment $\vec{\mu} = e\hat{\vec{q}}$ has been introduced and the electric field is defined as $\vec{E}(t) = \vec{\epsilon} E_0 \cos(\omega_{\text{pulse}} t)$ with $E_0 = \omega_{\text{pulse}} A_0$. Therefore, we recover the interaction potential given by Eq. (1.13). Note that this derivation applies for finite-length electromagnetic field as well.

B Systematic Analysis of the Basic Approximations

B.1 A Two-State Undisplaced Harmonic System with Linear Transition-Dipole Couplings

We consider the same two-state one-dimensional undisplaced harmonic oscillator with linear transition-dipole couplings as in Sec. 2.3.1 and represented in Fig. B.2 (a), but we now set $\mu'_{12}(Q_0) = 0.5$ and $E_0 = 100$ n.u. We compute the error of the wavefunction at initial and final time using the exact propagation scheme as a function of the number of grid points. The grid with lowest resolution is composed of 16 points from -5 to 5 n.u. We increase the number of points until we reach $N_0 = 65536$ points (our reference grid). Fig. B.1 depicts convergence with respect to grid density. 4096 grid points enables us to reach machine precision which justify our grid choice in the main text.

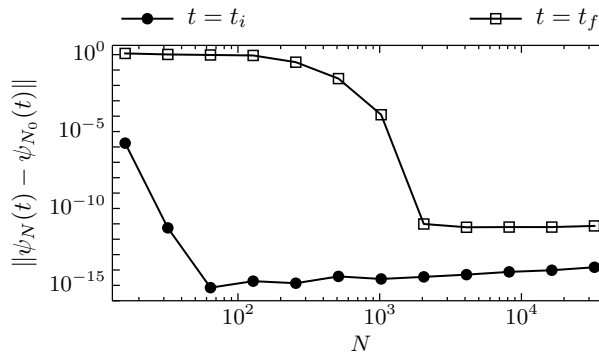


Figure B.1 – Convergence with respect to grid density for the exact quantum calculation applied to a one-dimensional two-state undisplaced harmonic system.

We make a systematic study of the basic approximations. To do so, we ensure that all the basic approximations are breaking down and we make all of them to work one at a time by the change of a single parameter. We give the corresponding dimensionless

Systematic Analysis of the Basic Approximations

parameters in Table B.1. We depict the laser pulse shapes and population dynamics for each of the basic approximations on Fig. B.2 (b)-(f) when approximations work on the left side and when they break down on the right side. We observe a break down of the ultrashort-pulse approximation [right panel of (f)] because the Condon approximation is not valid simultaneously with the ultrashort-pulse approximation. But, when we decrease the term $\mu'_{12}(Q_0)$ to 0.01 n.u. [left panel of (f)], the underlying Condon approximation is valid which makes also valid the ultrashort-pulse approximation.

Table B.1 – Dimensionless parameters (in natural units) for the one-dimensional two-state undisplaced harmonic system such that each of the basic approximations either breaks down or works.

	$\epsilon_c = \mu'_{12}(Q_0) $	ϵ_r	$\epsilon_p = E_0 \Delta t_{\text{pulse}}$	ϵ_u
failure	0.5	3 ($E_0 = 100$ n.u.)	25	0 [$\mu'_{12}(Q_0) = 0.5$ n.u.]
working	0.01	$3 \cdot 10^{-2}$ ($E_0 = 1$ n.u.)	0.025	0 [$\mu'_{12}(Q_0) = 0.01$ n.u.]

B.1. A Two-State Undisplaced Harmonic System with Linear Transition-Dipole Couplings

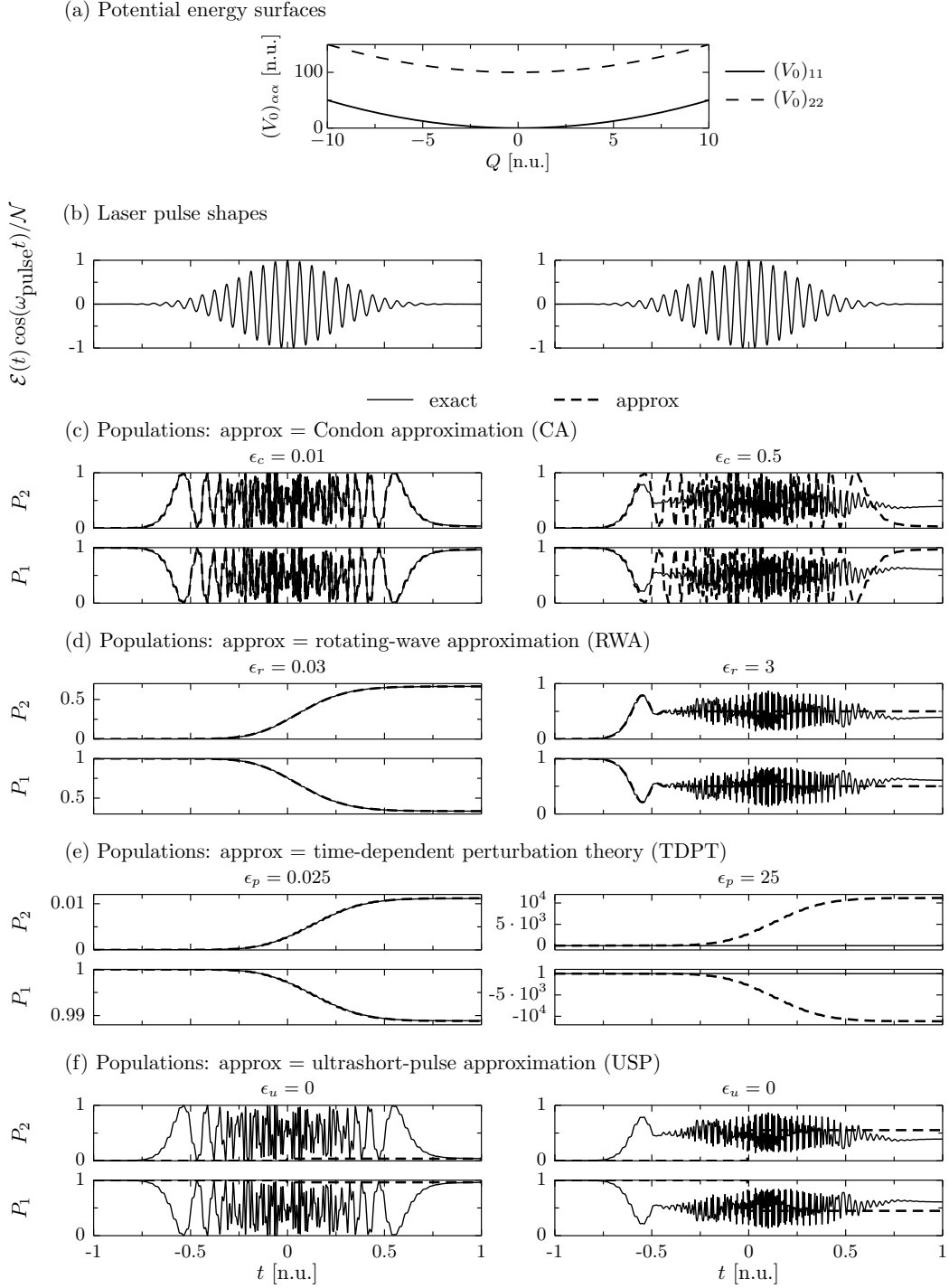


Figure B.2 – Several examples of population dynamics for the four basic approximations (c)-(f) together with the laser pulse shapes (b) applied to a one-dimensional two-state undisplaced harmonic system (a). All the right panels have the same exact result and show the discrepancy between approximate and exact quantum calculations. A single parameter has been changed in each of the left panels which causes the agreement of the corresponding approximation with respect to its exact counterpart.

B.2 A Two-State Displaced Harmonic System with Linear Transition-Dipole Couplings

We consider a two-state one-dimensional displaced harmonic oscillator with linear transition-dipole couplings [see Fig. B.4 (a)]. First, we set $\Delta Q_{21} = 4$, $\mu'_{12}(Q_0) = 0.3$, $\Delta t_{\text{pulse}} = 0.1875$, and $E_0 = 75$ n.u. Fig. B.3 depicts convergence with respect to grid density. Grid with lowest resolution is composed of 64 points from -5 to 13 n.u.

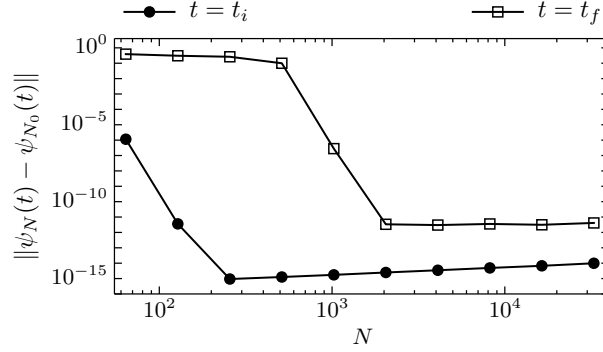


Figure B.3 – Convergence with respect to grid density for the exact quantum calculation applied to a one-dimensional two-state displaced harmonic system.

We make a systematic study of the basic approximations. To do so, we ensure that all the basic approximations are working (See Fig. B.4) by setting $\Delta Q_{21} = 1$, $\mu'_{12}(Q_0) = 0.1$, and $E_0 = 0.075$ n.u. and breaking down (See Fig. B.5) by setting $\Delta Q_{21} = 4$, $\mu'_{12}(Q_0) = 0.3$, and $E_0 = 75$ n.u. We give the corresponding dimensionless parameters in Tables B.2 and B.3, respectively.

Table B.2 – Dimensionless parameters (in natural units) for the one-dimensional two-state displaced harmonic system such that each of the basic approximations either works or breaks down.

	$\epsilon_c = \mu'_{12}(Q_0) $	ϵ_r	$\epsilon_p = E_0 \Delta t_{\text{pulse}}$	ϵ_u
working	0.1	$3 \cdot 10^{-3}$ ($E_0 = 0.075$ n.u.)	0.014	0.3 ($\Delta Q_{21} = 1$ n.u.)
failure	1	2 ($E_0 = 50$ n.u.)	0.14	1.1 ($\Delta Q_{21} = 4$ n.u.)

B.2. A Two-State Displaced Harmonic System with Linear Transition-Dipole Couplings

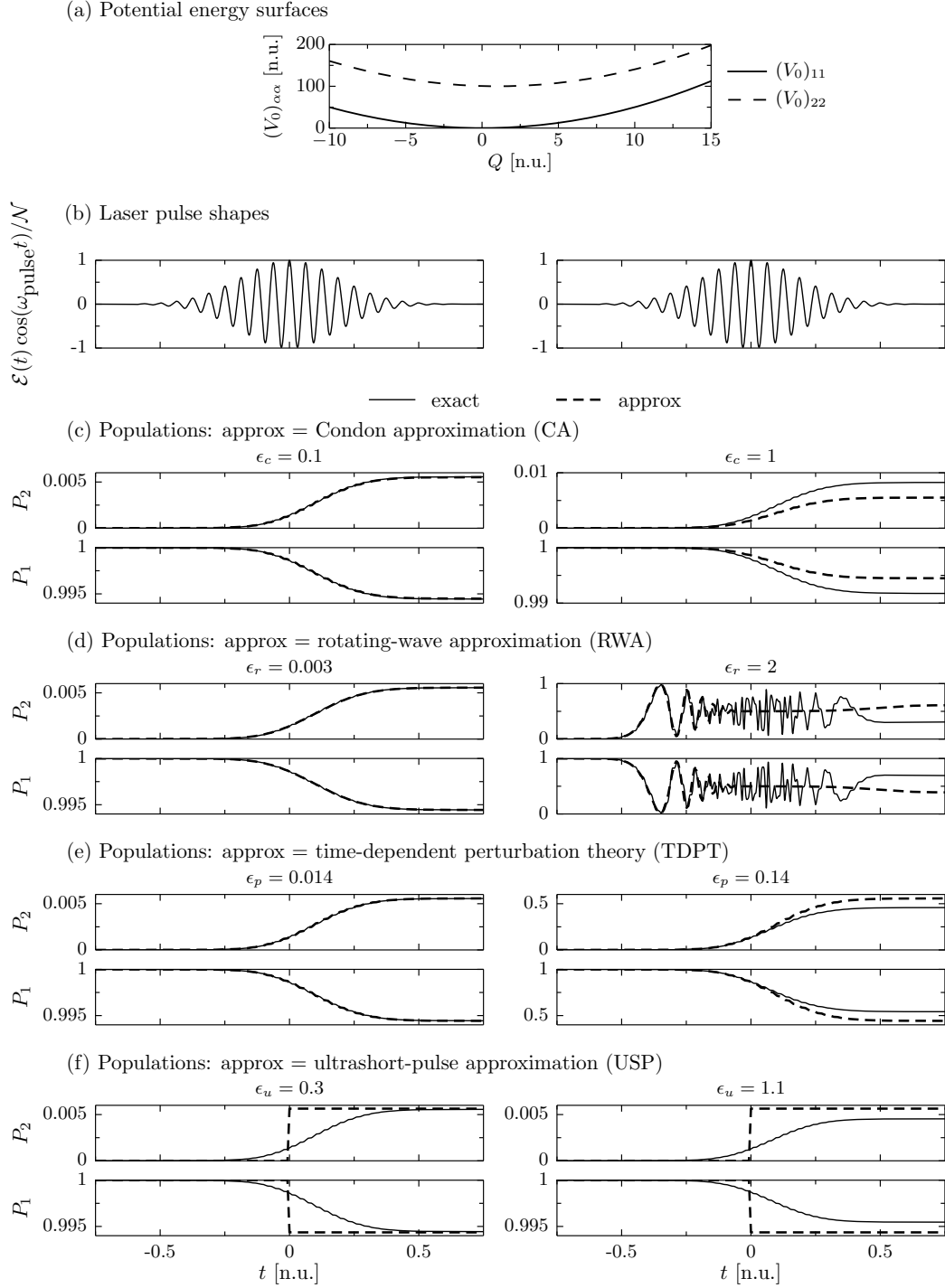


Figure B.4 – Several examples of population dynamics for the four basic approximations (c)-(f) together with the laser pulse shapes (b) applied to a one-dimensional two-state displaced harmonic system (a). The left panels show the agreement between approximate and exact quantum calculations. A single parameter has been changed in each of the right panels which causes the breakdown of the corresponding approximation with respect to its exact counterpart.

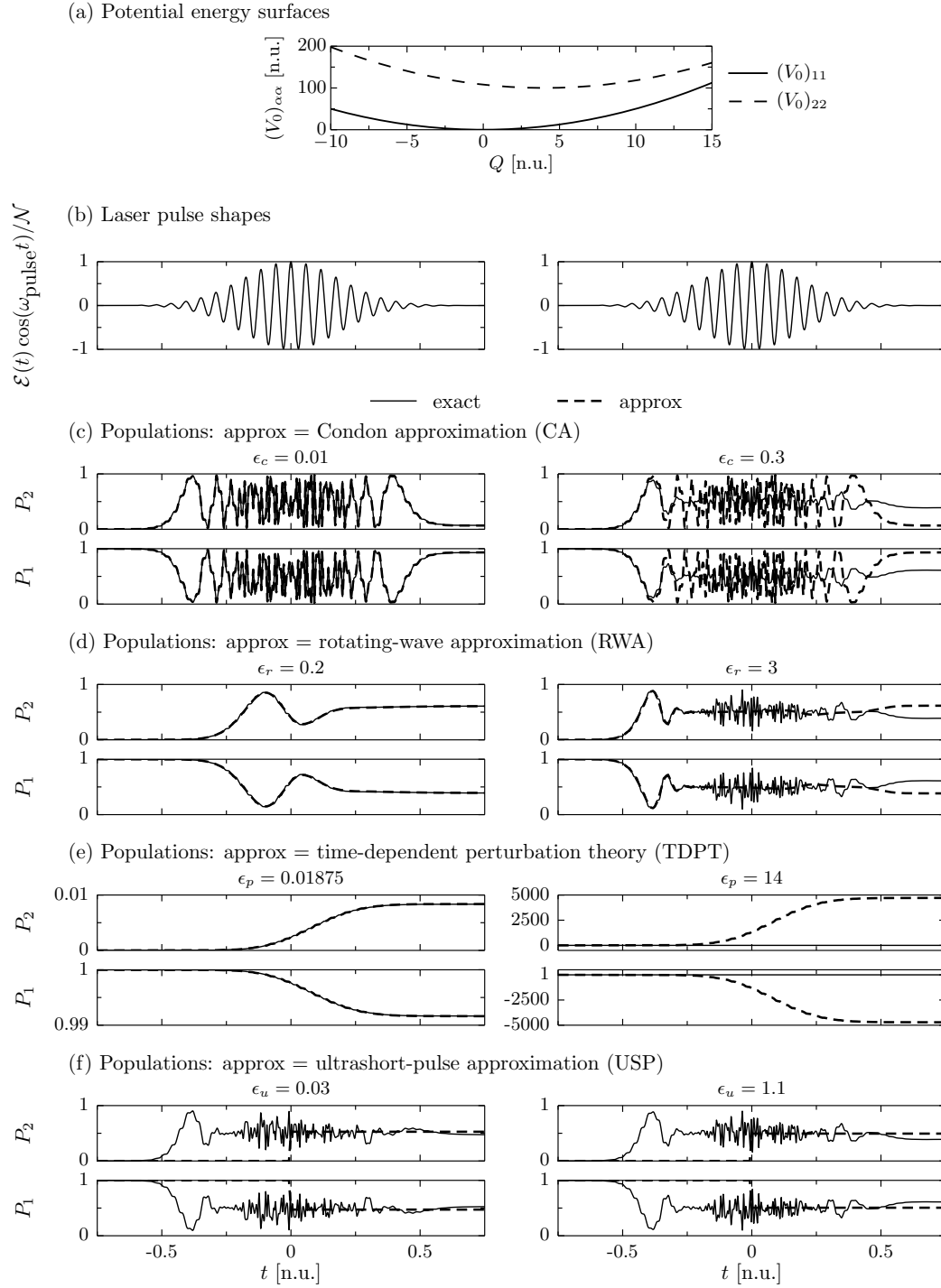


Figure B.5 – Several examples of population dynamics following the excitation of a one-dimensional two-state displaced harmonic system for the case where all the basic approximations break down. See Fig. B.2 for more details.

B.3. A Two-State Displaced Harmonic System with Different Force Constants and Linear Transition-Dipole Couplings

Table B.3 – Dimensionless parameters (in natural units) for the one-dimensional two-state displaced harmonic system such that each of the basic approximations either breaks down or works.

	$\epsilon_c = \mu'_{12}(Q_0) $	ϵ_r	$\epsilon_p = E_0 \Delta t_{\text{pulse}}$	ϵ_u
failure	0.3	3 ($E_0 = 75$ n.u.)	14	1.1 ($\Delta Q_{21} = 4$ n.u.)
working	0.01	$2 \cdot 10^{-1}$ ($E_0 = 5$ n.u.)	0.01875	0.03 ($\Delta Q_{21} = 0.1$ n.u.)

B.3 A Two-State Displaced Harmonic System with Different Force Constants and Linear Transition-Dipole Couplings

We consider a two-state one-dimensional displaced harmonic oscillator with different force constants and linear transition-dipole couplings [see Fig. B.8 (a)]. First, we set $\Delta Q_{21} = 4$, $k_2 = 2k$, $\mu'_{12}(Q_0) = 0.3$, $\Delta t_{\text{pulse}} = 0.1875$, and $E_0 = 50$ n.u. Fig. B.6 depicts convergence with respect to grid density. Grid with lowest resolution is composed of 64 points from -5 to 13 n.u.

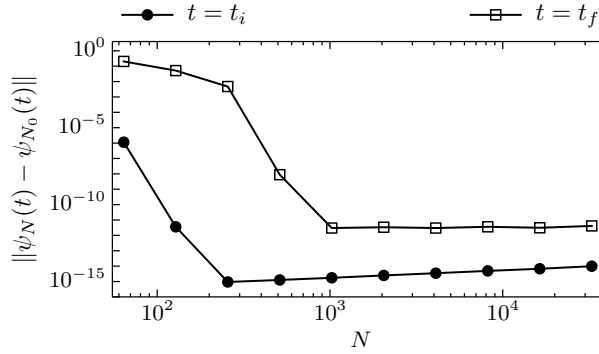


Figure B.6 – Convergence with respect to grid density for the exact quantum calculation applied to a one-dimensional two-state displaced harmonic system with different force constants.

We make a systematic study of the basic approximations. To do so, we ensure that all the basic approximations are working (See Fig. B.7) by setting $\Delta Q_{21} = 1$, $k_2 = 1.1k$, $\mu'_{12}(Q_0) = 0.1$, and $E_0 = 0.075$ n.u. and breaking down (See Fig. B.8) by setting $\Delta Q_{21} = 4$, $k_2 = 2k$, $\mu'_{12}(Q_0) = 0.3$, and $E_0 = 50$ n.u. We give the corresponding dimensionless parameters in Tables B.4 and B.5, respectively.

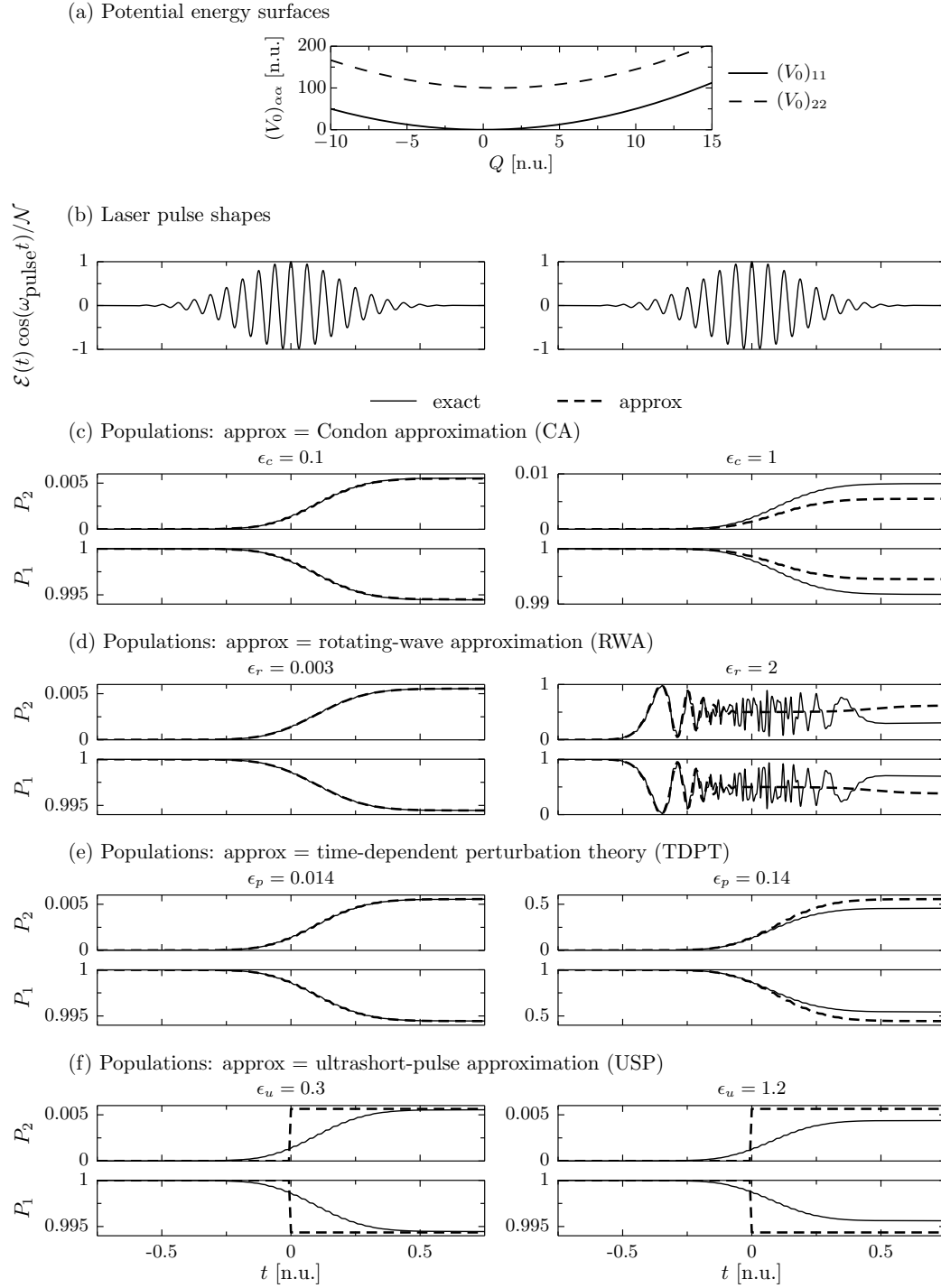


Figure B.7 – Several examples of population dynamics following the excitation of a one-dimensional two-state displaced harmonic system with different force constants for the case where all the basic approximations work. See Fig. B.4 for more details.

B.3. A Two-State Displaced Harmonic System with Different Force Constants and Linear Transition-Dipole Couplings

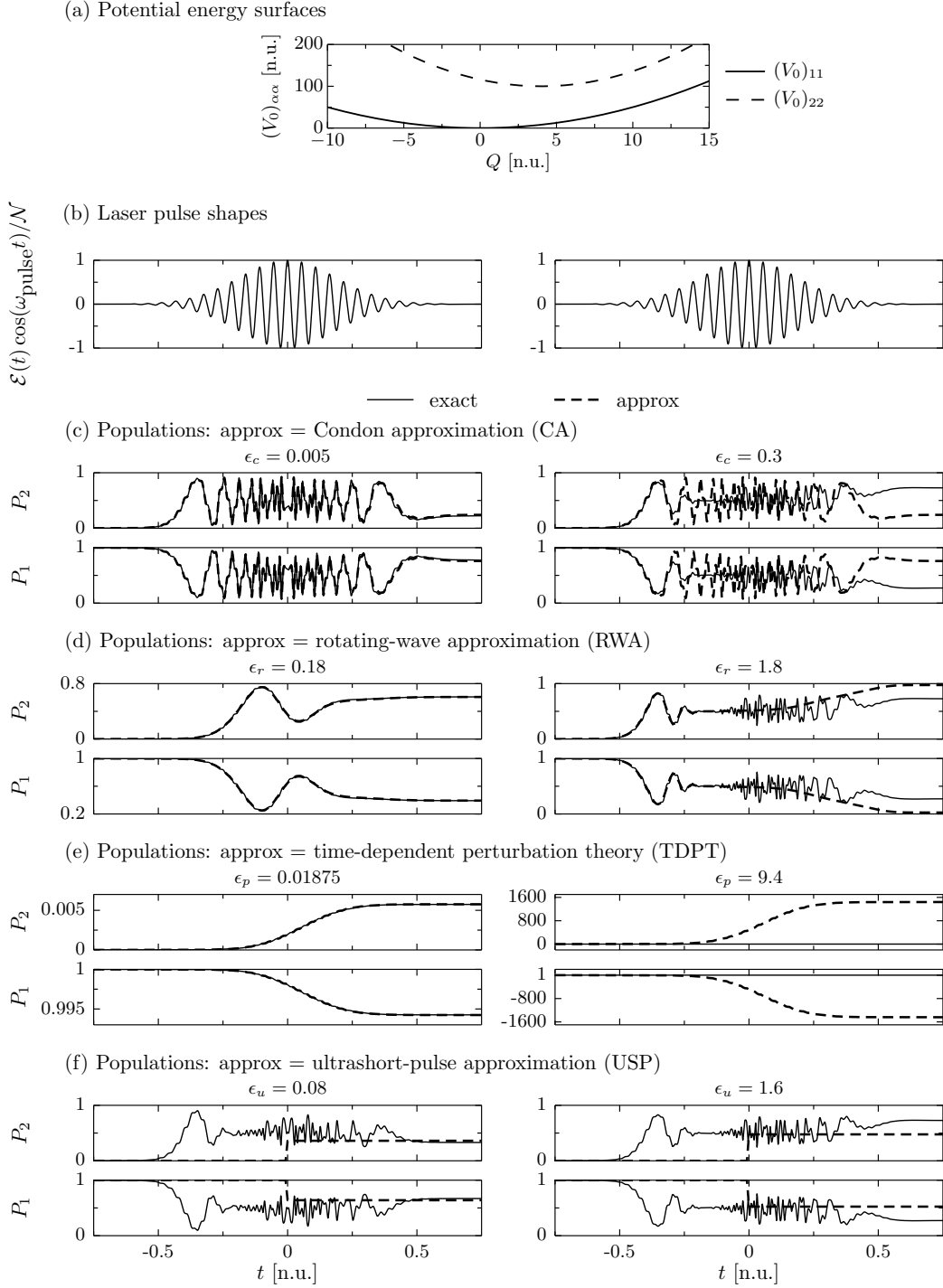


Figure B.8 – Several examples of population dynamics following the excitation of a one-dimensional two-state displaced harmonic system with different force constants for the case where all the basic approximations break down. See Fig. B.2 for more details.

Systematic Analysis of the Basic Approximations

Table B.4 – Dimensionless parameters (in natural units) for the one-dimensional two-state displaced harmonic system with different force constants such that each of the basic approximations either works or breaks down.

	$\epsilon_c = \mu'_{12}(Q_0) $	ϵ_r	$\epsilon_p = E_0 \Delta t_{\text{pulse}}$	ϵ_u
working	0.1	$3 \cdot 10^{-3}$ ($E_0 = 0.075$ n.u.)	0.014	($\Delta Q_{21} = 1$ n.u.)
failure	1	2 ($E_0 = 50$ n.u.)	0.14	1.2 ($\Delta Q_{21} = 4$ n.u.)

Table B.5 – Dimensionless parameters (in natural units) for the one-dimensional two-state displaced harmonic system with different force constants such that each of the basic approximations either breaks down or works.

	$\epsilon_c = \mu'_{12}(Q_0) $	ϵ_r	$\epsilon_p = E_0 \Delta t_{\text{pulse}}$	ϵ_u
failure	0.3	1.8 ($E_0 = 50$ n.u.)	9.4	1.6 ($\Delta Q_{21} = 4$ n.u.)
working	0.005	0.18 ($E_0 = 5$ n.u.)	0.01875	0.08 ($\Delta Q_{21} = 0.2$ n.u.)

B.4 A Three-State Harmonic System with Linear Vibronic and Transition-Dipole Couplings

We consider the three-state one-dimensional displaced harmonic oscillator with different force constants, linear transition-dipole and vibronic couplings as defined in Sec. 2.3.2 and represented in Fig. B.10 (a), but slightly modified such that $\Delta Q_{12} = 4$, $k_2 = 2k$, $\mu'_{12}(Q_0) = 0.3$, and $E_0 = 50$ n.u. Fig. B.9 depicts convergence with respect to grid density. Grid with lower resolution is composed of 128 points from -5 to 22 n.u.

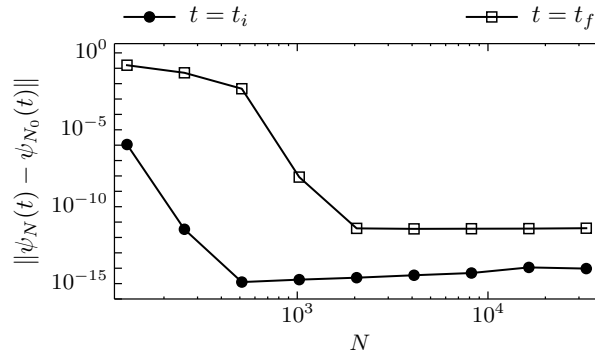


Figure B.9 – Convergence with respect to grid density for the exact quantum calculation applied to a one-dimensional three-state displaced harmonic system with different force constants.

We make a systematic study of the basic approximations. To do so, we ensure that all

B.4. A Three-State Harmonic System with Linear Vibronic and Transition-Dipole Couplings

Table B.6 – Dimensionless parameters (in natural units) for the one-dimensional three-state displaced harmonic system with different force constants such that each of the basic approximations either breaks down or work.

	$\epsilon_c = \mu'_{12}(Q_0) $	ϵ_r	$\epsilon_p = E_0 \Delta t_{\text{pulse}}$	ϵ_u
failure	0.3	1.8 ($E_0 = 50$ n.u.)	9.4	1.6 ($\Delta Q_{21} = 4$ n.u.)
working	0.005	0.18 ($E_0 = 5$ n.u.)	0.01875	0.08 ($\Delta Q_{21} = 0.2$ n.u.)

the basic approximations are breaking down (See Fig. B.10). We give the corresponding dimensionless parameters in Table B.6.

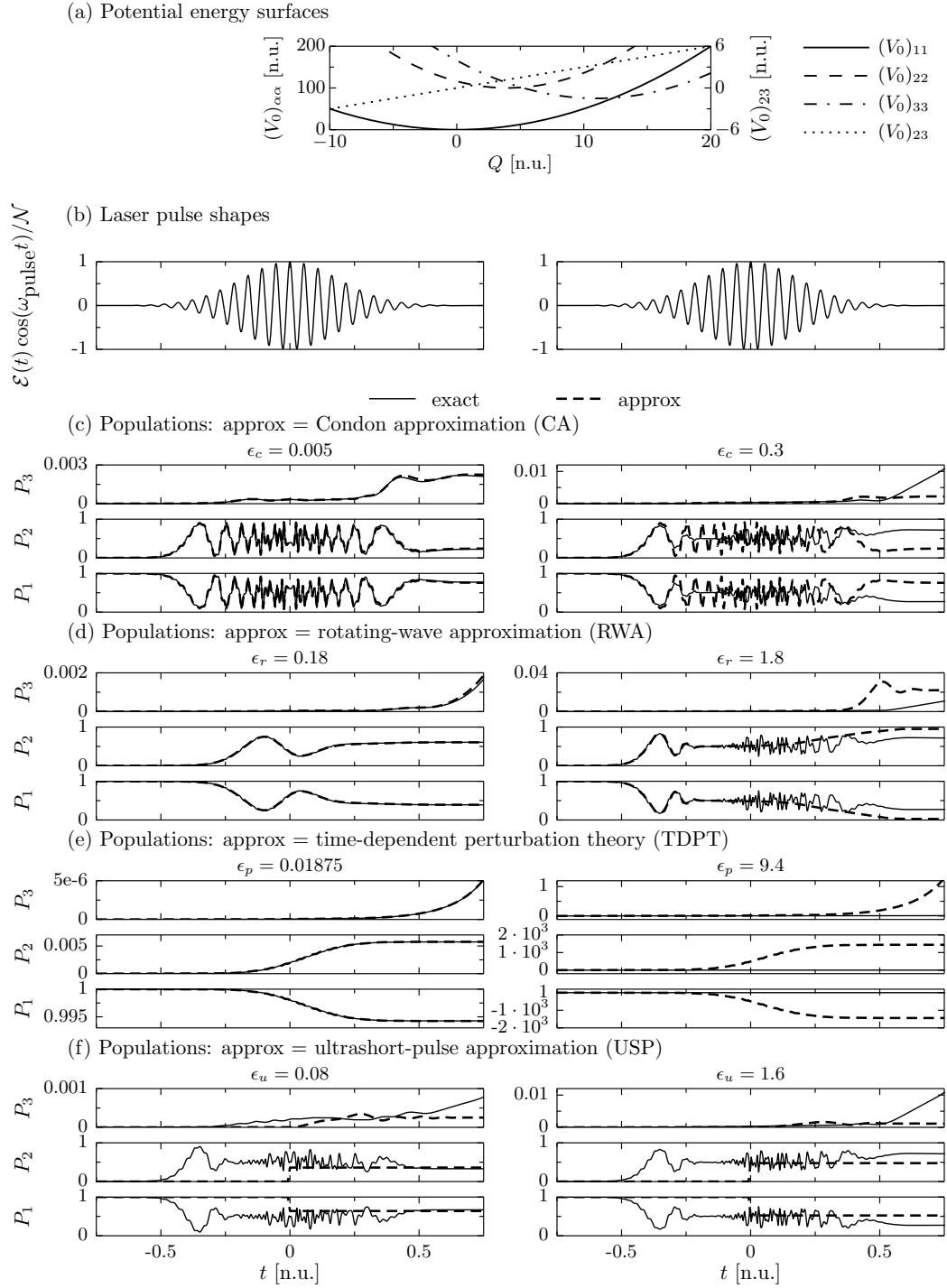


Figure B.10 – Several examples of population dynamics following the excitation of a one-dimensional three-state displaced harmonic system with different force constants for the case where all the basic approximations break down. See Fig. B.2 for more details.

C Procedure to Determine the CPU Cost and Speedup

We depict the error of an approximate method $\epsilon_{\text{approx}} = \|\psi_{\Delta t}^{\text{approx}}(t) - \psi_0^{\text{exact}}(t)\|$ with respect to the fully converged exact result for final time on Fig. C.1.

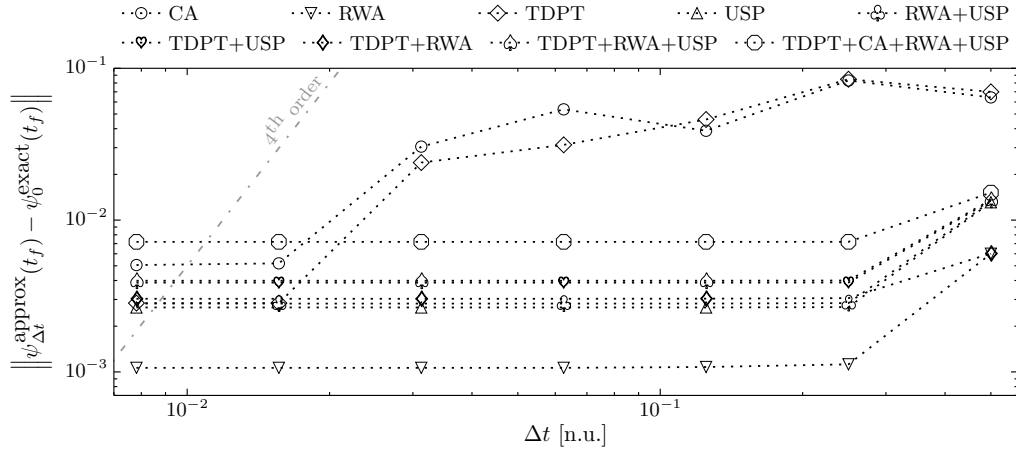


Figure C.1 – Error of various approximations compared to the fully converged exact quantum calculation as a function of the time step Δt using a fourth-order split-operator algorithm.

We assume the requested error for approximate and exact propagations to be

$$\begin{aligned}\epsilon_{\text{approx}}^{\text{req}} &= \alpha \epsilon_{\text{approx}} = \|\psi_{\Delta t}^{\text{approx}}(t) - \psi_0^{\text{approx}}(t)\|, \\ \epsilon_{\text{exact}}^{\text{req}} &= \alpha \epsilon_{\text{best approx}} = \|\psi_{\Delta t}^{\text{exact}}(t) - \psi_0^{\text{exact}}(t)\|,\end{aligned}$$

where $\alpha = 10^{-2}$ is a predefined condition. As for the ultrashort-pulse approximation (and the combinations with Condon and rotating-wave approximations) and for the time-dependent perturbation theory together with the ultrashort-pulse approximation (and the combinations with Condon and rotating-wave approximations), we have two type of errors: (1) coming from the split-operator (SO) algorithm, and (2) coming from the Magnus

Procedure to Determine the CPU Cost and Speedup

expansion (ME) or the numerical integration (NI). We make the two following assumptions:

$$(\alpha\epsilon_{\text{approx}})^2 = \sigma_{\text{SO}}^2 + \sigma_{\text{ME/NI}}^2 \text{ and } (\alpha\epsilon_{\text{approx}})^2 = 2\sigma_{\text{SO}}^2,$$

which means that the errors are taken to be independent and equal. Therefore, the requested error for the split-operator or Magnus expansion/numerical integration reads

$$\sigma_{\text{SO}} = \sigma_{\text{ME/NI}} = \frac{\alpha\epsilon_{\text{approx}}}{\sqrt{2}}.$$

We obtain the time steps Δt_{req} and $\Delta t_{\text{ME/NI,req}}$ needed to obtain the requested error for the split-operator and Magnus expansion/numerical integration, respectively, by reading from Figs. C.2 and C.3.

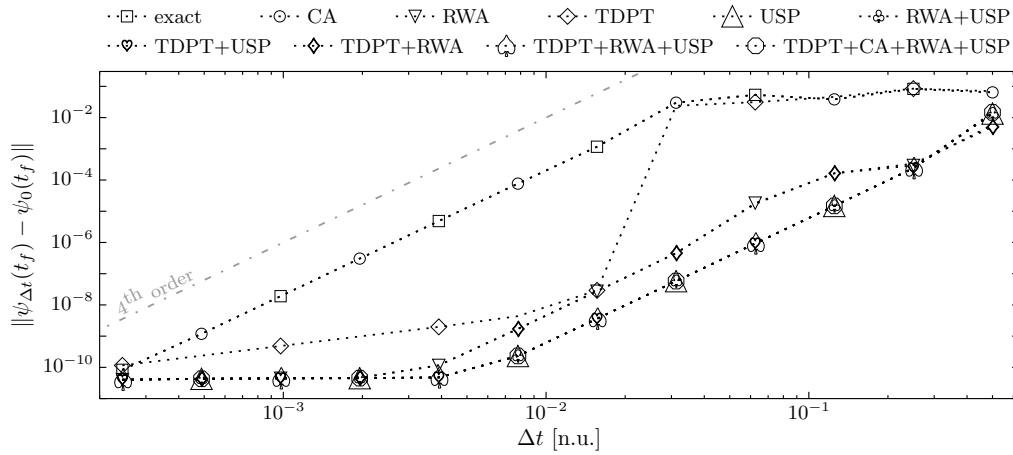


Figure C.2 – Error of various approximations as a function of the time step Δt using a fourth-order split-operator algorithm.

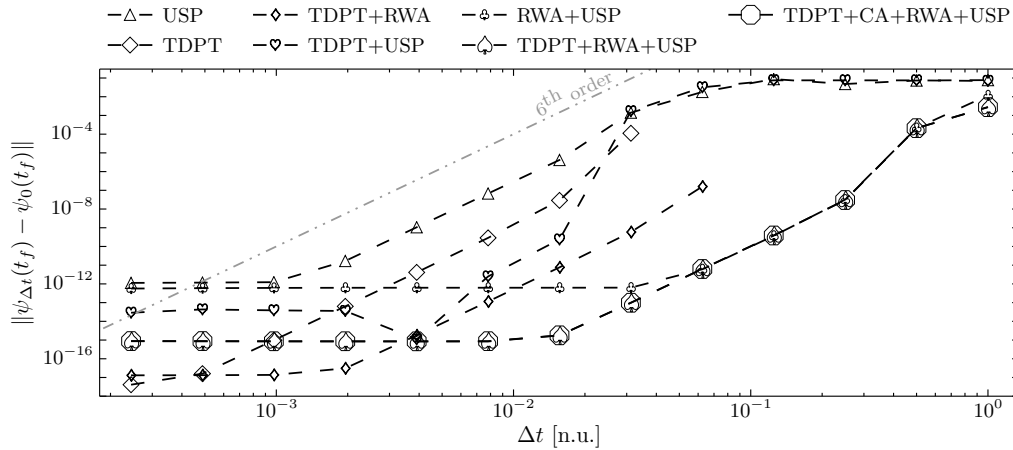


Figure C.3 – Error of various approximations as a function of the time step Δt using either a sixth-order commutator-free Magnus expansion algorithm or a sixth-order numerical integration scheme.

Then, as the total time of the simulation is known, we adjust the requested time steps Δt_{req} and $\Delta t_{\text{ME/NI,req}}$ to Δt and $\Delta t_{\text{ME/NI}}$ to make sure that the number of steps N is an integer.

Procedure to Determine the CPU Cost and Speedup

Note that N_{req} is not necessarily the same as N nor an integer. Finally, we perform the simulation with Δt and $\Delta t_{\text{ME/NI}}$ and we compute the achieved error as $\|\psi_{\Delta t}(t) - \psi_0(t)\|$ in order to see that the error is close to the requested one (see Table C.1 for errors computed at final time). Note that the achieved error can be different from the requested one because the time step that is used slightly differs from the requested one, due to the fact that an integer number of steps is required.

Table C.1 – Requested and achieved errors for several approximate methods.

method	$\ \psi_{\Delta t}(t_f) - \psi_0(t_f)\ _{\text{req}}$ $\times 10^{-5}$	$\ \psi_{\Delta t}(t_f) - \psi_0(t_f)\ _{\text{ach}}$ $\times 10^{-5}$
exact	1.1	1.0
CA	5.1	6.5
RWA	1.1	1.2
TDPT	2.8	1.3
USP	1.9	1.5
RWA+USP	2.0	1.5
TDPT+USP	2.8	3.1
RWA+TDPT	3.0	1.7
RWA+TDPT+USP	2.8	3.1
RWA+TDPT+USP+CA	5.1	3.1

The achieved CPU time and requested CPU time, obtained by tracking the time needed to perform the dynamics, read

$$\begin{aligned}\text{CPU time} &= N\beta, \\ \text{CPU time req.} &= N_{\text{req}}\beta,\end{aligned}$$

respectively, where β represents the time needed to perform a single step and depends on the order of the split-operator method. As the achieved CPU time is known, we easily obtain the requested CPU time as

$$\text{CPU time req.} = \text{CPU time} \frac{N_{\text{req}}}{N}.$$

Note that the previously described procedure is approximate for ultrashort-pulse approximation and for the combination of time-dependent perturbation theory and ultrashort-pulse approximation (and the combinations with Condon and rotating-wave approximations) because we assume that

$$\frac{\Delta t_{\text{req}}}{\Delta t_{\text{ME/NI, req}}} = \frac{\Delta t}{\Delta t_{\text{ME/NI}}},$$

which ensures that the time spends in the Magnus expansion or numerical integration is the same when we use the requested or achieved time step to perform the simulation.

Procedure to Determine the CPU Cost and Speedup

Obviously, it is not necessarily the case. Finally, the requested speedup reads

$$\text{speedup req.} = \frac{\text{CPU time req. exact}}{\text{CPU time req. approx.}}.$$

D Further Analysis of the Pump-Probe Experiment in Pyrazine

D.1 Rigorous Choices of Grid Density, Algorithms, and Time Steps

Fig. D.1 depicts convergence with respect to grid density. Grid with lowest resolution is composed of 4 points from -2 to $2 a_0$. in each dimension. The number of points in each dimension is increased until we reach $N_0 = 256$ points (our reference grid). We perform the quantum dynamics using the exact propagation scheme for $800 \hbar/E_h$ (fourth-order split-operator method with $\Delta t = 1 \hbar/E_h$, FWHM = 2 fs, and $E_0 = 0.5 E_h^2/ea_0\hbar$). We obtain the machine precision when we use 64 points from -8 to $8 a_0$ in each dimension.

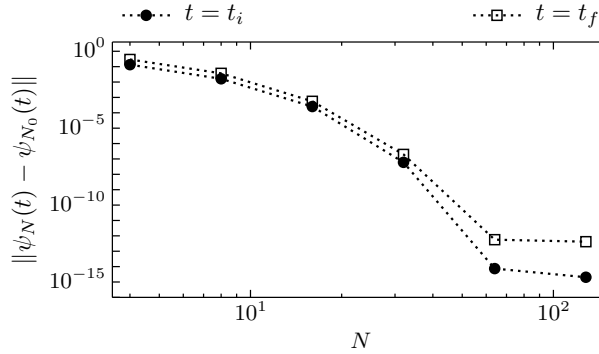


Figure D.1 – Convergence with respect to grid density for the exact quantum calculation applied to a three-dimensional three-state vibronic coupling model of pyrazine.

In order to obtain the best suited algorithms and time steps, we compute the error of the wavefunction as depicted in Fig. D.2. The benchmark wavefunction ψ_0 is propagated with a very small time step of $2^{-7} \hbar/E_h$. We use the sixth-order commutator-free Magnus expansion for the ultrashort-pulse approximation with a time step of $2^{-7} \hbar/E_h$. As for the time-independent Hamiltonian, we set the initial wavefunction to the second excited state

in order to ensure some nuclear dynamics. As for the time-dependent Hamiltonian, we use a single laser pulse of finite length with the following properties: $\Delta t_{\text{pulse}} = 100$, $t_m = 0$, $\varphi_{\text{pulse}} = 0$, $\omega_{\text{pulse}} = 0.179704$, and $E_0 = 0.5 E_h^2/ea_0\hbar$.

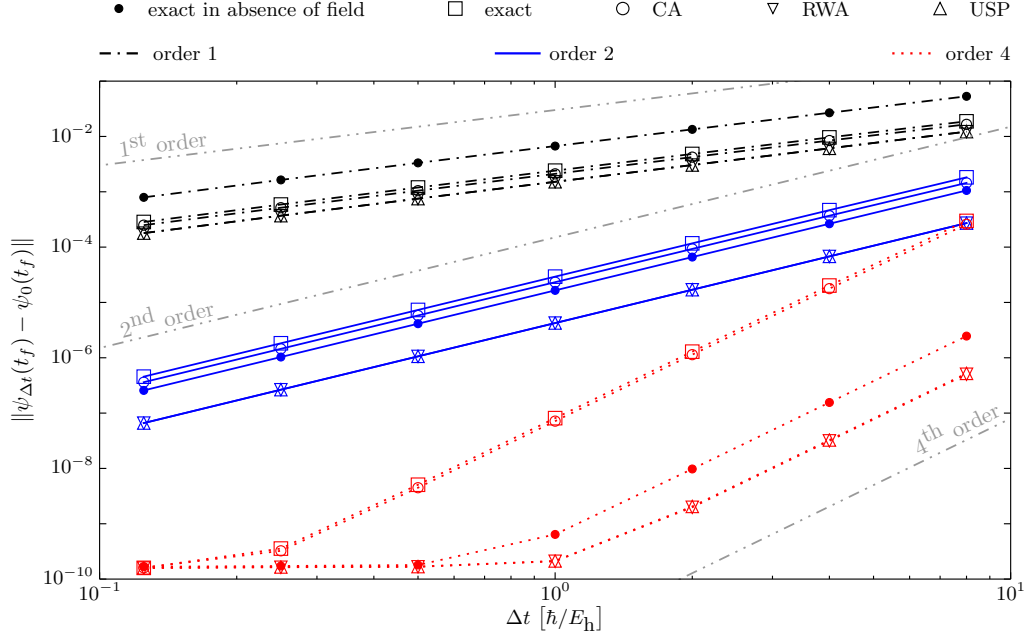


Figure D.2 – Error of various approximations as a function of the time step Δt using second- and fourth-order split-operator algorithms.

We fix the target error to 10^{-7} . Therefore, from Fig. D.2, we observe that the fourth-order splitting enables us to use the electronic and nuclear time steps of 1 and 4 \hbar/E_h , respectively. We do the same analysis for the Magnus expansion (see Fig. D.3) where we fix the split-operator nuclear time step to 4 \hbar/E_h . As for the same target error, we observe that for the ultrashort-pulse approximation, the largest time step is achieved when we use the sixth-order commutator-free Magnus expansion ($\Delta t = 8 \hbar/E_h$), and for the combination of rotating-wave and ultrashort-pulse approximations, the largest time step is achieved when we use the fourth-order commutator-free Magnus expansion ($\Delta t = 32 \hbar/E_h$).

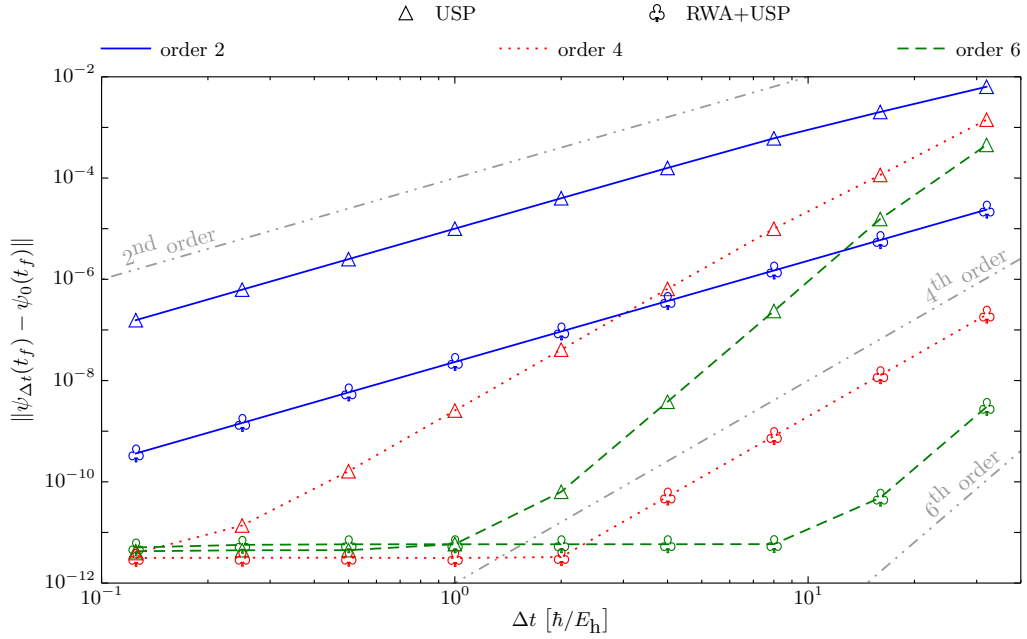


Figure D.3 – Error of various approximations as a function of the time step Δt using second-order Magnus expansion and fourth- and sixth-order commutator-free Magnus expansions.

D.2 Error Analysis of Several Propagation Methods

We perform the comparison of the accuracy of the Condon and rotating-wave approximations and its combination with respect to the exact propagation scheme, and of the Condon and ultrashort-pulse approximations, rotating-wave and ultrashort-pulse approximations, and Condon, rotating-wave, and ultrashort-pulse approximations with respect to the ultrashort-pulse approximation. To do so, we compute, as a function of time, the error of the difference between the exact/ultrashort-pulse approximation wavefunction and the wavefunction computed with an approximate method. We show the results in Fig. D.4. We observe, as depicted in the population dynamics of Fig. 2.7 from Sec. 2.3.3, that the use of the Condon, rotating-wave, or Condon and rotating-wave approximations gives a very good agreement with respect to the exact counterpart. Similarly, the combinations of Condon and ultrashort-pulse approximations, rotating-wave and ultrashort-pulse approximations, and Condon, rotating-wave, and ultrashort-pulse approximations are in good agreement with the ultrashort-pulse approximation. However, the comparison of the exact method and the ultrashort-pulse approximation leads to an error of 1.5 at final time which means that those two approaches differ significantly.

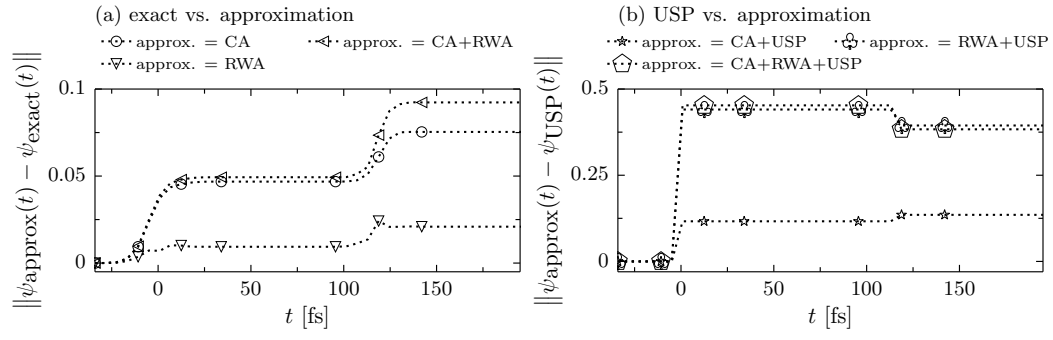


Figure D.4 – Error of various approximations compared to (a) the exact quantum calculation and (b) the ultrashort-pulse approximation as a function of time.

E Convergence of the Second-Order Split-Operator Algorithm

In order to demonstrate the effect of the choice of the set of c coefficients on the convergence of the second-order split-operator algorithm, we use the following splitting of the split-operator algorithm

$$\hat{\mathbf{U}}_{\hat{\mathbf{T}}+\hat{\mathbf{V}}(t)}^{\text{SO } 2^{\text{nd}}}(\Delta t) = \hat{\mathbf{U}}_{\hat{\mathbf{V}}(t+c_2\Delta t)}(\Delta t/2)\hat{\mathbf{U}}_{\hat{\mathbf{T}}}(\Delta t)\hat{\mathbf{U}}_{\hat{\mathbf{V}}(t+c_1\Delta t)}(\Delta t/2) \quad (\text{E.1})$$

and apply it to the one-dimensional displaced harmonic oscillator coupled via an explicit laser field as defined in Sec. 3.5.1. We depict in Fig. E.1 the error of the wavefunction at final time of the simulation as a function of the time step Δt .

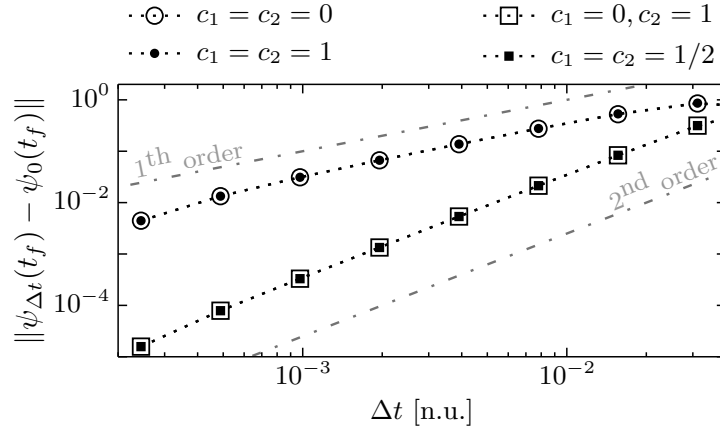


Figure E.1 – Error of the exact quantum calculation as a function of the time step Δt using a second-order split-operator method and different time-evaluation of the time-dependent interaction potential.

Eq. (3.6) suggests that in order to have the correct second-order of convergence, the c coefficients must be given by 0 and 1, which is confirmed by the figure. In addition, when we use $c_1 = c_2 = 1/2$, even if the general formula (3.6) is not respected, we also obtain a convergence of second-order. The most probable reason of this behaviour is that the

Convergence of the Second-Order Split-Operator Algorithm

interaction potential is evaluated twice in the middle of the time interval, which makes the propagator to still be symmetric and time-reversible. However, if we perform both evaluations by using the same boundary but no longer in the middle of the time interval, i.e., $c_1 = c_2 = 0$ (evaluation at time t) or $c_1 = c_2 = 1$ (evaluation at time $t + \Delta t$), then, the convergence of the algorithm decreases to first-order.

F Further Analysis of the Ultrashort- and δ -Pulse Approximations

F.1 Rigorous Choice of Grid Density

We investigate the convergence with respect to grid density for the exact propagation scheme of the three-state three-dimensional vibronic coupling model of pyrazine with and without vibronic couplings and we depict the results in Fig. F.1. To do so, we compute the error of the wavefunction at initial and final time as a function of the number of grid points. The dynamics is performed using a fourth-order split-operator method with $\Delta t = 1 \hbar/E_h$, FWHM = 2 fs, and $E_0 = 0.5 E_h/ea_0$. ψ_{N_0} represents the benchmark wavefunction that is assumed to be fully converged and propagated using a grid composed of 256 points per dimension equally spaced between -16 and 16 a_0 . (Note that to test the grid size, we start with 4 equally spaced points per dimension between -2 and 2 a_0 and increase the number of points by a factor of two while increasing Q_{\min} and Q_{\max} by the square root of two.) It reflects our actual choice of the grid given in Sec. 4.2.

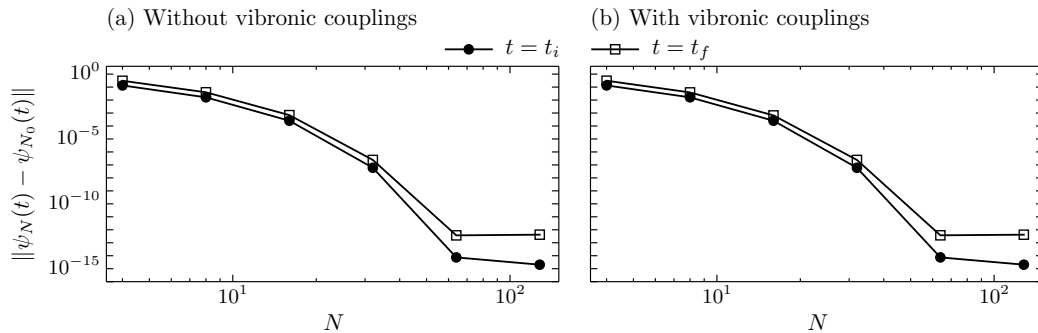


Figure F.1 – Convergence with respect to grid density for the exact quantum calculation applied to a three-dimensional three-state vibronic coupling model of pyrazine without vibronic couplings (a) and with vibronic couplings (b).

F.2 Rigorous Choices of the Split-Operator Algorithm and the Nuclear and Electronic Time Steps

We investigate the order of convergence with respect to the time step Δt by computing the error of the final wavefunction for first-, second-, and fourth-order split-operator algorithm. We propagate three different kind of Hamiltonians: (1) time-independent Hamiltonian without nonadiabatic couplings, (2) time-independent Hamiltonian with nonadiabatic couplings, and (3) time-dependent Hamiltonian with vibronic couplings. We depict the results in Fig. F.2. ψ_0 represents the benchmark wavefunction that is assumed to be fully converged and propagated with a very small time step of $2^{-4} \hbar/E_h$ for $1400 \hbar/E_h$. As for the time-independent Hamiltonian, initially, we vertically transfer the wavefunction to the excited state and let it evolves. It ensures that there is some nuclear dynamics during the propagation. Indeed, the initial state is no longer a vibrational eigenstate of the given electronic state. As for the time-dependent Hamiltonian, we use a single laser pulse of finite length with $\Delta t_{\text{pulse}} = 175 \hbar/E_h$ and $E_0 = 0.5 E_h/ea_0$ (the only parameters that differ from the ones given in Sec. 4.2).

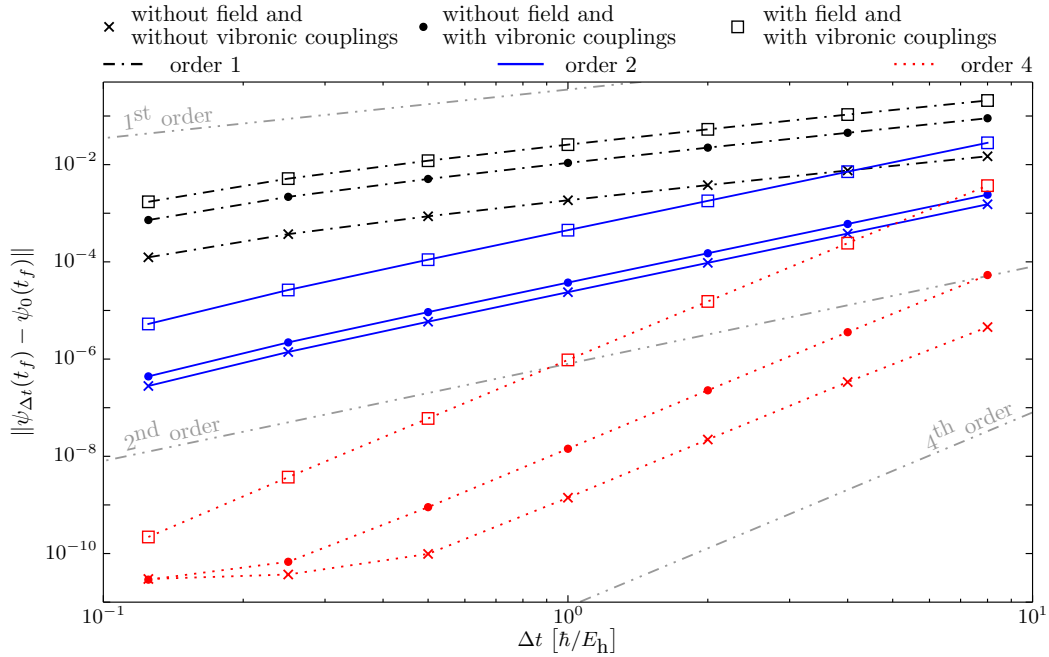


Figure F.2 – Error of various approximations as a function of the time step Δt using first-, second-, and fourth-order split-operator algorithms.

As for the calculations in the main text, we fix the error to 10^{-6} . Therefore, the algorithm of choice for propagating the wavefunction is the fourth-order split-operator algorithm: the one that allows the biggest time steps. Without vibronic couplings, we use a nuclear time step of $4 \hbar/E_h$. When the couplings are switched on, we propagate the time-independent Hamiltonian with a time step of $2 \hbar/E_h$, whereas we use an electronic time step of $1 \hbar/E_h$ for the propagation of the time-dependent Hamiltonian.

G Optimized Geometries and Vibrational Frequencies for Ground and Excited States of Phenyl Radical and Benzene

G.1 Phenyl Radical

We give the Cartesian equilibrium geometries of ground \tilde{X}^2A_1 and excited \tilde{A}^2B_1 states of phenyl radical in Table G.1. Table G.2 gives the symmetry of phenyl radical normal modes together with the corresponding ground and excited state frequencies. As for the latter, we show both results from adiabatic harmonic and vertical harmonic models. In addition, we present the displacements δ between the ground state minimum and the excited state global harmonic potentials. We transform them from mass-scaled normal mode coordinates to atomic units using the fact that $1 \text{ a.u.} \simeq 0.012 \sqrt{\text{a.m.u.}} \text{ \AA}$, where a.m.u. is the atomic mass unit. Moreover, we also give the dimensionless relative displacements $\Delta = A_0^{1/2} \cdot \delta$. They take into account the fact that a displacement of a low-frequency mode does not have such effect on the resulting spectrum compared to the same displacement of a high-frequency mode.

Optimized Geometries and Vibrational Frequencies for Ground and Excited States of Phenyl Radical and Benzene

Table G.1 – Optimized cartesian geometries (in Å) of ground \tilde{X}^2A_1 and excited \tilde{A}^2B_1 states of phenyl radical.

	\tilde{X}^2A_1			\tilde{A}^2B_1		
	x	y	z	x	y	z
C	0.000	1.227	0.772	0.000	1.213	0.734
C	0.000	1.214	-0.632	0.000	1.228	-0.644
C	0.000	0.000	-1.324	0.000	0.000	-1.343
C	0.000	-1.214	-0.632	0.000	-1.228	-0.644
C	0.000	-1.227	0.772	0.000	-1.213	0.734
C	0.000	0.000	1.398	0.000	0.000	1.549
H	0.000	2.163	1.324	0.000	2.169	1.258
H	0.000	-2.154	-1.178	0.000	-2.160	-1.204
H	0.000	-2.163	1.324	0.000	-2.169	1.258
H	0.000	2.154	-1.178	0.000	2.160	-1.204
H	0.000	0.000	-2.410	0.000	0.000	-2.430

Table G.2 – Symmetry of phenyl radical normal modes together with the corresponding ground \tilde{X}^2A_1 and first excited \tilde{A}^2B_1 states frequencies in cm^{-1} [using adiabatic harmonic (AH) and vertical harmonic (VH) models], displacements δ in a.u., and dimensionless relative displacements $\Delta = A_0^{1/2} \cdot \delta$.

Mode	Symmetry	\tilde{X}^2A_1	\tilde{A}^2B_1 (AH)			\tilde{A}^2B_1 (VH)		
		ω	ω	δ	Δ	ω	δ	Δ
		[cm^{-1}]	[cm^{-1}]	[a.u.]		[cm^{-1}]	[a.u.]	
1	A ₁	3193	3187	-0.06	-0.0054	3195	0.01	0.0007
2	B ₂	3184	3168	0	0	3166	0	0
3	A ₁	3181	3162	-0.14	-0.0122	3167	-0.04	-0.0032
4	B ₂	3168	3140	0	0	3155	0	0
5	A ₁	3161	3139	0.03	0.0025	3150	-0.02	-0.0017
6	B ₂	1631	1522	0	0	1548	0	0
7	A ₁	1573	1633	12.92	0.7732	1571	13.96	0.8357
8	A ₁	1468	1443	-9.41	-0.5442	1447	-10.39	-0.6007
9	B ₂	1460	1395	0	0	1494	0	0
10	B ₂	1336	1351	0	0	1364	0	0
11	B ₂	1303	1243	0	0	1273	0	0
12	A ₁	1172	1214	-3.39	-0.1749	1192	-3.36	-0.1890
13	B ₂	1171	1119	0	0	1090	0	0
14	B ₂	1069	1049	0	0	1037	0	0
15	A ₁	1047	1018	-11.51	-0.5623	1071	-9.87	-0.4820
16	A ₁	1015	1000	7.79	0.3745	1023	4.65	0.2237
17	B ₁	997	1027	0	0	1014	0	0
18	A ₁	981	924	30.81	1.4563	950	33.80	1.5977
19	A ₂	970	998	0	0	971	0	0
20	B ₁	895	968	0	0	934	0	0
21	A ₂	815	788	0	0	800	0	0
22	B ₁	721	768	0	0	696	0	0
23	B ₁	671	685	0	0	673	0	0
24	A ₁	614	590	-28.08	-1.0498	541	-39.27	-1.4682
25	B ₂	593	528	0	0	419	0	0
26	B ₁	425	355	0	0	223	0	0
27	A ₂	401	301	0	0	212	0	0

G.2 Benzene

We give the bond length equilibrium geometries of ground 1^1A_{1g} and excited 1^1B_{2u} states of benzene in Table G.3. Table G.4 gives the symmetry of benzene normal modes together with the corresponding ground and excited state frequencies (using adiabatic harmonic and vertical harmonic models). In addition, we present the displacements δ between the ground state minimum and the excited state global harmonic potentials and dimensionless relative displacements Δ .

Table G.3 – Optimized bond lengths (in Å) of ground 1^1A_{1g} and excited 1^1B_{2u} states of benzene.

	1^1A_{1g}	1^1B_{2u}
R_{C-C}	1.398	1.430
R_{C-H}	1.086	1.085

Table G.4 – Symmetry of benzene normal modes together with the corresponding ground 1^1A_{1g} and first excited 1^1B_{2u} states frequencies in cm^{-1} [using adiabatic harmonic (AH) and vertical harmonic (VH) models], displacements δ in a.u., and dimensionless relative displacements Δ .

Mode	Symmetry	1^1A_{1g}		1^1B_{2u} (AH)		1^1B_{2u} (VH)		
		ω	ω	δ	Δ	ω	δ	Δ
		[cm $^{-1}$]	[cm $^{-1}$]	[a.u.]		[cm $^{-1}$]	[a.u.]	
1	A $_{1g}$	3207	3232	0.90	0.077	3212	0.87	0.074
2	E $_{1u}$	3197	3221	0	0	3199	0	0
3	E $_{1u}$	3197	3221	0	0	3199	0	0
4	E $_{2g}$	3182	3207	0	0	3183	0	0
5	E $_{2g}$	3182	3207	0	0	3183	0	0
6	B $_{1u}$	3172	3201	0	0	3177	0	0
7	E $_{2g}$	1642	1571	0	0	1678	0	0
8	E $_{2g}$	1642	1571	0	0	1678	0	0
9	E $_{1u}$	1515	1449	0	0	1497	0	0
10	E $_{1u}$	1515	1449	0	0	1497	0	0
11	A $_{2g}$	1378	1361	0	0	1385	0	0
12	B $_{2u}$	1353	1474	0	0	1620	0	0
13	E $_{2g}$	1198	1179	0	0	1215	0	0
14	E $_{2g}$	1198	1179	0	0	1215	0	0
15	B $_{2u}$	1176	1175	0	0	1201	0	0
16	E $_{1u}$	1061	970	0	0	1029	0	0
17	E $_{1u}$	1061	970	0	0	1029	0	0
18	B $_{1u}$	1017	999	0	0	1006	0	0
19	B $_{2g}$	1013	782	0	0	791	0	0
20	A $_{1g}$	1013	957	-21.28	-1.022	1035	-19.69	-0.946
21	E $_{2u}$	983	746	0	0	755	0	0
22	E $_{2u}$	983	746	0	0	755	0	0
23	E $_{1g}$	863	594	0	0	603	0	0
24	E $_{1g}$	863	594	0	0	603	0	0
25	B $_{2g}$	712	332	0	0	231	0	0
26	A $_{2u}$	689	555	0	0	577	0	0
27	E $_{2g}$	619	529	0	0	526	0	0
28	E $_{2g}$	619	529	0	0	526	0	0
29	E $_{2u}$	412	236	0	0	94	0	0
30	E $_{2u}$	412	236	0	0	94	0	0



Bibliography

- [1] E. Teller, J. Phys. Chem. **41**, 109 (1937).
- [2] J. von Neumann and E. Wigner, Physik. Z. **30**, 467 (1929).
- [3] W. Domcke and D. R. Yarkony, Annu. Rev. Phys. Chem. **63**, 325 (2012).
- [4] M. A. Robb, M. Garavelli, M. Olivucci, and F. Bernardi, Rev. Comput. Chem. **15**, 87 (2000).
- [5] W. Domcke, D. R. Yarkony, and H. Köppel, *Conical Intersections: Electronic Structure, Dynamics and Spectroscopy* (Adv. Ser. Phys. Chem. 15. Singapore: World Sci., 2004).
- [6] A. H. Zewail, J. Phys. Chem. **97**, 12427 (1993).
- [7] A. H. Zewail, Science **242**, 1645 (1988).
- [8] L. R. Khundkar and A. H. Zewail, Annu. Rev. Phys. Chem. **41**, 15 (1990).
- [9] M. Dantus, M. J. Rosker, and A. H. Zewail, J. Chem. Phys. **89**, 6128 (1988).
- [10] T. S. Rose, M. J. Rosker, and A. H. Zewail, J. Chem. Phys. **88**, 6672 (1988).
- [11] A. H. Zewail, *Femtochemistry: Ultrafast Dynamics of the Chemical Bond* (World Sci., 1994).
- [12] M. J. Rosker, M. Dantus, and A. M. Zewail, J. Chem. Phys. **89**, 6113 (1988).
- [13] A. Mokhtari, A. Chebira, and J. Chesnoy, J. Opt. Soc. Am. B **7**, 1551 (1989).
- [14] W. B. Bosma, Y. J. Yan, and S. Mukamel, J. Chem. Phys. **93**, 3863 (1990).
- [15] Y. J. Yan and S. Mukamel, Phys. Rev. A **41**, 6485 (1990).
- [16] M. Seel and W. Domcke, J. Chem. Phys. **95**, 7806 (1991).
- [17] M. F. Gelin, D. Egorova, and W. Domcke, J. Chem. Phys. **123**, 164112 (2005).

- [18] M. F. Gelin, D. Egorova, and W. Domcke, *Acc. Chem. Res.* **42**, 1290 (2009).
- [19] M. F. Gelin, D. Egorova, and W. Domcke, *J. Phys. Chem. B* **115**, 5648 (2011).
- [20] M. F. Gelin, D. Egorova, and W. Domcke, *J. Phys. Chem. Lett.* **2**, 114 (2011).
- [21] D. P. Craig and T. Thirunamachandran, *Molecular Quantum Electrodynamics* (Dover Publications, 1998).
- [22] M. Rama Krishna and R. Coalson, *Chem. Phys.* **120**, 327 (1988).
- [23] S. O. Williams and D. G. Imre, *J. Phys. Chem.* **92**, 6636 (1988).
- [24] W. Domcke and H. Köppel, *Chem. Phys. Lett.* **140**, 133 (1987).
- [25] G. Stock and W. Domcke, *Chem. Phys.* **124**, 227 (1988).
- [26] G. Stock, R. Schneider, and W. Domcke, *J. Chem. Phys.* **90**, 7184 (1989).
- [27] S.-Y. Lee, W. T. Pollard, and R. A. Mathies, *Chem. Phys. Lett.* **163**, 11 (1989).
- [28] G. Stock and W. Domcke, *J. Opt. Soc. Am. B* **7**, 1970 (1990).
- [29] W. T. Pollard, S.-Y. Lee, and R. A. Mathies, *J. Chem. Phys.* **92**, 4012 (1990).
- [30] J. Rauch and G. Mourou, *Proc. Amer. Math. Soc.* **134**, 851 (2006).
- [31] G. Stock and W. Domcke, *Phys. Rev. A* **45**, 3032 (1992).
- [32] F. Bloch and A. Siegert, *Phys. Rev.* **57**, 522 (1940).
- [33] M. P. Silverman and F. M. Pipkin, *J. Phys. B* **5**, 1844 (1972).
- [34] K. B. Whaley and J. C. Light, *Phys. Rev. A* **29**, 1188 (1984).
- [35] P. W. Miloni and J. P. Eberly, *Laser Physics* (John Wiley & Sons, 2010).
- [36] M. Quack, *J. Chem. Phys.* **69**, 1282 (1978).
- [37] M. Quack, *Chem. Phys. Lett.* **65**, 140 (1979).
- [38] M. Quack and E. Sutcliffe, *J. Chem. Phys.* **83**, 3805 (1985).
- [39] R. Marquardt and M. Quack, *J. Chem. Phys.* **90**, 6320 (1989).
- [40] M. Quack and F. Merkt, *Handbook of High-resolution Spectroscopy* (John Wiley & Sons, 2011).
- [41] J. Franck, *Trans. Faraday Soc.* **21**, 536 (1925).
- [42] E. U. Condon, *Phys. Rev.* **28**, 1182 (1926).
- [43] E. U. Condon, *Proc. Nat. Acad. Sci.* **13**, 462 (1927).
- [44] E. U. Condon, *Phys. Rev.* **32**, 858 (1928).

-
- [45] D. J. Tannor, R. Kosloff, and S. A. Rice, *J. Chem. Phys.* **85**, 5805 (1986).
- [46] D. J. Tannor, *Introduction to quantum mechanics, a time-dependent perspective* (University Science Books, 2007).
- [47] R. Kosloff, *J. Phys. Chem.* **92**, 2087 (1988).
- [48] R. Kosloff, *Annu. Rev. Phys. Chem.* **45**, 145 (1994).
- [49] H.-O. Kreiss and J. Oliger, *Tellus* **24**, 199 (1972).
- [50] C. Leforestier, R. H. Bisseling, C. Cerjan, M. D. Feit, R. Friesner, A. Guldberg, A. Hammerich, G. Jolicard, W. Karrlein, H.-D. Meyer, N. Lipkin, O. Roncero, and R. Kosloff, *J. Comp. Phys.* **94**, 59 (1991).
- [51] C. J. Williams, J. Qian, and D. J. Tannor, *J. Chem. Phys.* **95**, 1721 (1991).
- [52] N. Makri, *Annu. Rev. Phys. Chem.* **50**, 167 (1999).
- [53] K. Kormann, S. Holmgren, and H. O. Karlsson, *J. Chem. Phys.* **128**, 184101 (2008).
- [54] H. Tal-Ezer and R. Kosloff, *J. Chem. Phys.* **81**, 3967 (1984).
- [55] U. Peskin, R. Kosloff, and N. Moiseyev, *J. Chem. Phys.* **100**, 8849 (1994).
- [56] G. Yao and R. E. Wyatt, *J. Chem. Phys.* **101**, 1904 (1994).
- [57] A. Askar and A. S. Cakmak, *J. Chem. Phys.* **68**, 2794 (1978).
- [58] D. Kosloff and R. Kosloff, *J. Comp. Phys.* **52**, 35 (1983).
- [59] R. Kosloff and D. Kosloff, *J. Chem. Phys.* **79**, 1823 (1983).
- [60] G. Stock, C. Woywod, and W. Domcke, *Chem. Phys. Lett.* **200**, 163 (1992).
- [61] L. Seidner and W. Domcke, *Chem. Phys.* **186**, 27 (1994).
- [62] A. Iserles, H. Z. Munthe-Kaas, S. P. Nørsett, and A. Zanna, *Acta Numerica* **9**, 215 (2000).
- [63] R. I. McLachlan and G. R. W. Quispel, *J. of Phys. A: Math. and Gen.* **39**, 5251 (2006).
- [64] M. D. Feit, J. A. J. Fleck, and A. Steiger, *J. Comp. Phys.* **47**, 412 (1982).
- [65] M. D. Feit and J. A. J. Fleck, *J. Chem. Phys.* **78**, 301 (1983).
- [66] H. De Raedt, *Comp. Phys. Rep.* **7**, 1 (1987).
- [67] H. Yoshida, *Phys. Lett. A* **150**, 262 (1990).
- [68] A. D. Bandrauk and H. Shen, *Chem. Phys. Lett.* **176**, 428 (1991).
- [69] M. Wehrle, M. Sulc, and J. Vaníček, *Chimia* **65**, 334 (2011).

- [70] S. A. Chin and C. R. Chen, *J. Chem. Phys.* **117**, 1409 (2002).
- [71] W. Magnus, *Comm. Pure Appl. Math.* **7**, 649 (1954).
- [72] P. Pechukas and J. C. Light, *J. Chem. Phys.* **44**, 3897 (1966).
- [73] W. R. Salzman, *J. Chem. Phys.* **85**, 4605 (1986).
- [74] S. Blanes, F. Casas, and J. Ros, *BIT* **40**, 434 (2000).
- [75] M. Hochbruck and C. Lubich, *SIAM J. Num. Analysis* **41**, 945 (2003).
- [76] S. Blanes and P. C. Moan, *App. Numer. Math.* **56**, 1519 (2006).
- [77] S. Blanes, F. Casas, J. A. Oteo, and J. Ros, *Phys. Rep.* **470**, 151 (2009).
- [78] S. A. Chin and C. R. Chen, *J. Chem. Phys.* **114**, 7338 (2001).
- [79] S. A. Chin, *Phys. Rev. E* **77**, 066401 (2001).
- [80] F. Mouhat, S. Bonella, and C. Pierleoni, *Commun. Math. Phys.* **111**, 3651 (2013).
- [81] J. V. V. Kasper and G. C. Pimentel, *Appl. Phys. Lett.* **5**, 231 (1964).
- [82] A. Tehlar and H.-J. Wörner, *Mol. Phys.* **111**, 2057 (2013).
- [83] P. M. Kraus, Y. Arasaki, J. B. Bertrand, S. Patchkovskii, P. B. Corkum, D. M. Villeneuve, K. Takatsuka, and H. J. Wörner, *Phys. Rev. A* **85**, 043409 (2012).
- [84] A. Rupenyan, P. M. Kraus, J. Schneider, and H. J. Wörner, *Phys. Rev. A* **87**, 031401 (2013).
- [85] H.-J. Wörner, J. B. Bertrand, P. Corkum, and D. M. Villeneuve, *Phys. Rev. Lett.* **105**, 103002 (2010).
- [86] H.-J. Wörner, J. B. Bertrand, D. V. Kartashov, P. Corkum, and D. M. Villeneuve, *Nature* **466**, 604 (2010).
- [87] H.-J. Wörner, J. B. Bertrand, B. Fabre, J. Highet, H. Ruf, A. Dubrouil, S. Patchkovskii, M. Spanner, Y. Mairesse, V. Blanchet, E. Mével, E. Constant, P. B. Corkum, and D. M. Villeneuve, *Science* **208**, 208 (2011).
- [88] P. M. Kraus, A. Rupenyan, and H. J. Wörner, *Phys. Rev. Lett.* **109**, 233903 (2012).
- [89] P. M. Kraus and H.-J. Wörner, *Chem. Phys.* **414**, 32 (2013).
- [90] J. Itatani, J. Levesque, D. Zeidler, H. Niikura, H. Pepin, J. C. Kieffer, P. B. Corkum, and D. M. Villeneuve, *Nature* **432**, 867 (2004).
- [91] N. L. Wagner, A. Wüest, I. P. Christov, T. Popmintchev, X. Zhou, M. M. Murnane, and H. C. Kapteyn, *Proc. Natl Acad. Sci. USA* **103**, 13279 (2006).
- [92] W. Li, X. Zhou, R. Lock, S. Patchkovskii, A. Stolow, H. C. Kapteyn, and M. M. Murnane, *Science* **322**, 1207 (2008).

-
- [93] V.-H. Le, A.-T. Le, R.-H. Xie, and C. D. Lin, Phys. Rev. A **76**, 013414 (2007).
- [94] H.-D. Meyer, U. Manthe, and L. S. Cederbaum, Chem. Phys. Lett. **165**, 73 (1990).
- [95] M. H. Beck, A. Jäckle, G. A. Worth, and H.-D. Meyer, Phys. Rep. **324**, 1 (2000).
- [96] I. Burghardt, H.-D. Meyer, and L. S. Cederbaum, J. Chem. Phys. **111**, 2927 (1999).
- [97] I. Burghardt, K. Giri, and G. A. Worth, J. Chem. Phys. **129**, 174104 (2008).
- [98] T. Martínez, M. Ben-Nun, and R. D. Levine, J. Chem. Phys. **100**, 7884 (1996).
- [99] T. Martínez, M. Ben-Nun, and G. Ashkenazi, J. Chem. Phys. **104**, 2847 (1996).
- [100] M. Ben-Nun and T. Martínez, Adv. Chem. Phys. **121**, 439 (2002).
- [101] L. S. Cederbaum, E. Gindensperger, and I. Burghardt, Phys. Rev. Lett. **94**, 113003 (2005).
- [102] E. Gindensperger, I. Burghardt, and L. S. Cederbaum, J. Chem. Phys. **124**, 144103 (2006).
- [103] S. Mukamel, *Principles of Nonlinear Optical Spectroscopy* (Oxford University Press, 1995).
- [104] S. Mukamel, J. Chem. Phys. **77**, 173 (1982).
- [105] J. Vaníček and E. Heller, Phys. Rev. E **68**, 056208 (2003).
- [106] J. Vaníček, Phys. Rev. E **70**, 055201 (2004).
- [107] J. Vaníček, Phys. Rev. E **73**, 046204 (2006).
- [108] T. Zimmermann and J. Vaníček, J. Chem. Phys. **132**, 241101 (2010).
- [109] T. Zimmermann and J. Vaníček, J. Chem. Phys. **136**, 094106 (2012).
- [110] T. Zimmermann and J. Vaníček, J. Chem. Phys. **137**, 22A516 (2012).
- [111] E. J. Heller, J. Chem. Phys. **62**, 1544 (1975).
- [112] E. J. Heller, Acc. Chem. Res. **14**, 368 (1981).
- [113] S.-Y. Lee and E. J. Heller, J. Chem. Phys. **76**, 3035 (1982).
- [114] M. Wehrle, M. Sulc, and J. Vaníček, J. Chem. Phys. **140**, 244114 (2014).
- [115] M. Wehrle, S. Oberli, and J. Vaníček, J. Phys. Chem. A **119**, 5685 (2015).
- [116] G. C. Schatz and M. A. Ratner, *Quantum Mechanics in Chemistry* (Dover Publications, 2002).
- [117] F. J. Dyson, Phys. Rev. **75**, 486 (1949).
- [118] J. W. Cooley and J. W. Tukey, Math. Comp. **19**, 297 (1965).

- [119] C. Temperton, J. Comp. Phys. **52**, 1 (1983).
- [120] T. Zimmermann and J. Vaníček, J. Chem. Phys. **141**, 134102 (2014).
- [121] A. Patoz and J. Vaníček, “Geometric integrators for the nonadiabatic dynamics induced by the interaction with the electromagnetic field: 1. approximations for the molecule-field interaction,” (In preparation).
- [122] F. Schwabl, *Quantum Mechanics* (Springer, 1992).
- [123] G. Boole and J. F. Moulton, *A Treatise on the Calculus of Finite Differences* (Dover Publications, 1960).
- [124] R. Schneider and W. Domcke, Chem. Phys. Lett. **150**, 235 (1988).
- [125] C. Woywod, W. Domcke, A. L. Sobolewski, and H.-J. Werner, J. Chem. Phys. **100**, 1400 (1994).
- [126] G. Stock, C. Woywod, W. Domcke, T. Swinney, and B. S. Hudson, J. Chem. Phys. **103**, 6851 (1995).
- [127] A. Patoz and J. Vaníček, “Geometric integrators for the nonadiabatic dynamics induced by the interaction with the electromagnetic field: 2. split-operator and magnus integrators of arbitrary order,” (In preparation).
- [128] D. Frenkel and B. Smit, *Understanding Molecular Simulation, From Algorithm to Applications* (Academic press, 2002).
- [129] C. Lubich, *From Quantum to Classical Molecular Dynamics: Reduced Models and Numerical Analysis* (European Math. Soc., 2008).
- [130] A. Patoz and J. Vaníček, “Geometric integrators for the nonadiabatic dynamics induced by the interaction with the electromagnetic field: 3. ultrashort-pulse approximations,” (In preparation).
- [131] G. Stock and W. Domcke, J. Phys. Chem. **97**, 12466 (1993).
- [132] M. P. Bircher, E. Liberatore, N. J. Browning, S. Brickel, C. Hofmann, A. Patoz, O. T. Unke, T. Zimmermann, M. Chergui, P. Hamm, U. Keller, M. Meuwly, H.-J. Wörner, J. Vaníček, and U. Roethlisberger, “Nonadiabatic effects in electronic and nuclear dynamics,” (Submitted).
- [133] A. Patoz, A. Tehlar, J. Vaníček, and H.-J. Wörner, “Photodissociation of iodomethane following the pump-pulse excitation to the A band: Nonadiabatic quantum dynamical study,” (In preparation).
- [134] H. Guo, J. Chem. Phys. **96**, 6629 (1992).
- [135] M. Shapiro, J. Phys. Chem. **90**, 3644 (1986).
- [136] M. Shapiro and R. Bersohn, J. Chem. Phys. **73**, 3810 (1980).

-
- [137] H. Guo and G. C. Schatz, *J. Chem. Phys.* **93**, 393 (1990).
- [138] H. Guo, K. Q. Lao, G. C. Schatz, and A. D. Hammerich, *J. Chem. Phys.* **94**, 6562 (1991).
- [139] E. J. Heller, *J. Chem. Phys.* **68**, 3891 (1978).
- [140] I. Powis and J. F. Black, *J. Phys. Chem.* **93**, 2461 (1989).
- [141] R. Ogorzalek Loo, H.-P. Haerri, G. E. Hall, and P. L. Houston, *J. Chem. Phys.* **90**, 4222 (1989).
- [142] J. F. Black and I. Powis, *J. Chem. Phys.* **89**, 3986 (1988).
- [143] J. F. Black and I. Powis, *Chem. Phys.* **125**, 375 (1988).
- [144] C. R. Evenhuis and U. Manthe, *J. Phys. Chem. A* **115**, 5992 (2011).
- [145] T. Gerdtts and U. Manthe, *J. Chem. Phys.* **107**, 6584 (1997).
- [146] D. M. Medvedev, L. B. Harding, and S. K. Gray, *Mol. Phys.* **104**, 73 (2006).
- [147] Y. Amatatsu, S. Yabushita, and K. Morokuma, *J. Chem. Phys.* **104**, 9783 (1996).
- [148] D. Xie, H. Guo, Y. Amatatsu, and R. Kosloff, *J. Phys. Chem. A* **104**, 1009 (2000).
- [149] G. Barinovs, N. Marković, and G. Nyman, *J. Chem. Phys.* **111**, 6705 (1999).
- [150] J. V. Lill, G. A. Parker, and J. C. Light, *J. of Phys. A: Math. and Gen.* **89**, 483 (1982).
- [151] J. C. Light, I. P. Hamilton, and J. V. Lill, *J. Chem. Phys.* **82**, 1400 (1985).
- [152] D. T. Colbert and W. H. Miller, *J. Chem. Phys.* **96**, 1983 (1991).
- [153] A. Patoz, T. Begušić, and J. Vaniček, “On-the-fly ab initio semiclassical evaluation of absorption spectra of polyatomic molecules beyond the condon approximation,” (Submitted).
- [154] G. Herzberg and E. Teller, *Z. Phys. Chem. B* **21**, 410 (1933).
- [155] C. Eckart, *Phys. Rev.* **47**, 552 (1935).
- [156] J. T. Hougen and J. K. G. Watson, *Can. J. Phys.* **43**, 298 (1965).
- [157] I. Ozkan, *J. Mol. Spectros.* **139**, 147 (1990).
- [158] K. N. Kudin and A. Y. Dymarsky, *J. Chem. Phys.* **122**, 224105 (2005).
- [159] V. Barone, J. Bloino, M. Biczysko, and F. Santoro, *J. Chem. Theory Comput.* **5**, 540 (2009).
- [160] T. Azumi and K. Matsuzaki, *Photochem. Photobiol.* **25**, 315 (1977).

Bibliography

- [161] F. J. Avila Ferrer and F. Santoro, *Phys. Chem. Chem. Phys.* **14**, 13549 (2012).
- [162] M. Biczysko, J. Bloino, F. Santoro, and V. Barone, *Computational Strategies for Spectroscopy* (John Wiley & Sons, 2011).
- [163] S. Mukamel, S. Abe, and R. Islampour, *J. Phys. Chem.* **89**, 201 (1985).
- [164] R. Borelli and A. Peluso, *Can. J. Chem.* **91**, 495 (2013).
- [165] M. J. Frisch, G. W. Trucks, H. B. Schlegel, G. E. Scuseria, M. A. Robb, J. R. Cheeseman, G. Scalmani, V. Barone, B. Mennucci, G. A. Petersson, H. Nakatsuji, M. Caricato, X. Li, H. P. Hratchian, A. F. Izmaylov, J. Bloino, G. Zheng, J. L. Sonnenberg, M. Hada, M. Ehara, K. Toyota, R. Fukuda, J. Hasegawa, M. Ishida, T. Nakajima, Y. Honda, O. Kitao, H. Nakai, T. Vreven, J. A. Montgomery, Jr., J. E. Peralta, F. Ogliaro, M. Bearpark, J. J. Heyd, E. Brothers, K. N. Kudin, V. N. Staroverov, R. Kobayashi, J. Normand, K. Raghavachari, A. Rendell, J. C. Burant, S. S. Iyengar, J. Tomasi, M. Cossi, N. Rega, J. M. Millam, M. Klene, J. E. Knox, J. B. Cross, V. Bakken, C. Adamo, J. Jaramillo, R. Gomperts, R. E. Stratmann, O. Yazyev, A. J. Austin, R. Cammi, C. Pomelli, J. W. Ochterski, R. L. Martin, K. Morokuma, V. G. Zakrzewski, G. A. Voth, P. Salvador, J. J. Dannenberg, S. Dapprich, A. D. Daniels, O. Farkas, J. B. Foresman, J. V. Ortiz, J. Cioslowski, and D. J. Fox, "Gaussian 09 Revision D.01," Gaussian Inc. Wallingford CT 2009.
- [166] G. Porter and B. Ward, *Proc. R. Soc. Lond. A* **287**, 457 (1965).
- [167] J. G. Radziszewski, *Chem. Phys. Lett.* **301**, 565 (1999).
- [168] G. S. Kim, A. M. Mebel, and S. H. Lin, *Chem. Phys. Lett.* **361**, 421 (2002).
- [169] F. Duschinsky, *Acta Physicochimica U.R.S.S.* **7**, 551 (1937).
- [170] M. Biczysko, J. Bloino, and F. Barone, *Chem. Phys. Lett.* **471**, 143 (2002).
- [171] A. Baiardi, J. Bloino, and F. Barone, *J. Chem. Theory Comput.* **9**, 4097 (2013).
- [172] L. Tutt, D. Tannor, J. Schindler, E. J. Heller, and J. I. Zink, *J. Phys. C* **87**, 3017 (1983).
- [173] J. Li, C.-K. Lin, X. Y. Li, C. Y. Zhu, and S. H. Lin, *Phys. Chem. Chem. Phys.* **12**, 14967 (2010).
- [174] G. Herzberg, *Molecular Spectra and Molecular Structure: III. Electronic Spectra of Polyatomic Molecules* (D. Van Nostrand Company, 1966).
- [175] J. Hollas, *Modern Spectroscopy* (John Wiley & Sons, 2004).
- [176] P. F. Bernath, *Spectra of atoms and molecules* (Oxford University Press, 2005).
- [177] M. Wehrli, *Helv. Phys. Acta* **11**, 339 (1938).
- [178] H. Sponer, G. Nordheim, L. Sklar, and E. Teller, *J. Chem. Phys.* **7**, 207 (1939).

- [179] V. Gradinaru, Computing **80**, 1 (2007).
- [180] V. Gradinaru, SIAM J. Num. Analysis **46**, 103 (2007).

Personal Details

Name M. Aurélien Patoz
Address Avenue de Lonay 1
1110 Morges, Switzerland
Telephone +41 79 535 07 16
E-mail aurelien.patoz@wanadoo.fr
Nationality French
Date of birth 3rd of October 1990



Educational Qualifications

Ph.D. student in the Laboratory of Theoretical Physical Chemistry <i>EPFL, Switzerland</i>	present
Master of Science MSc in molecular and biological chemistry <i>EPFL, Switzerland</i>	2013
Minor in physics <i>EPFL, Switzerland</i>	2013
Bachelor of Science BSc in chemistry and chemical engineering <i>EPFL, Switzerland</i>	2011

Publications

Nonadiabatic Effects in Electronic and Nuclear Dynamics

M. P. Bircher, E. Liberatore, N. J. Browning, S. Brickel, C. Hofmann, A. Patoz, O. T. Unke, T. Zimmermann, M. Chergui, P. Hamm, U. Keller, M. Meuwly, H.-J. Wörner, J. Vaníček, and U. Roethlisberger
Submitted

On-the-fly Ab Initio Semiclassical Evaluation of Absorption Spectra of Polyatomic Molecules beyond the Condon Approximation

A. Patoz, T. Begušić, and J. Vaníček
Submitted

Ab Initio Semiclassical Evaluation of Herzberg-Teller Spectra: Including More Anharmonicity with a Three Thawed Gaussian Approximation

T. Begušić, A. Patoz, and J. Vaníček
In preparation

Geometric Integrators for the Nonadiabatic Dynamics Induced by the Interaction with the Electromagnetic Field: I. Approximations for the Molecule-Field Interaction

A. Patoz and J. Vaniček

In preparation

Geometric Integrators for the Nonadiabatic Dynamics Induced by the Interaction with the Electromagnetic Field: II. Split-Operator and Magnus Integrators of Arbitrary Order

A. Patoz and J. Vaniček

In preparation

Geometric Integrators for the Nonadiabatic Dynamics Induced by the Interaction with the Electromagnetic Field: III. Ultrashort-Pulse Approximations

A. Patoz and J. Vaniček

In preparation

Photodissociation of Iodomethane Following the Pump-Pulse Excitation to the A Band: Nonadiabatic Quantum Dynamical Study

A. Patoz, A. Tehlar, J. Vaniček, and H.-J. Wörner

In preparation

Prizes and Grants

Student grant	2014
----------------------	------

International Science at FELs Conference, PSI, Switzerland

Runners-up best poster award in computational chemistry	2013
--	------

Fall Meeting of the Swiss Chemical Society, EPFL, Switzerland

Oral Presentations

Geometric Integrators of Arbitrary Order of Accuracy for Molecular Quantum Dynamics in Electromagnetic Fields	2016
--	------

High Dimensional Quantum Dynamics, Rostock, Germany

Geometric Integrators of Arbitrary Order of Accuracy for Molecular Quantum Dynamics in Electromagnetic Fields	2016
--	------

Different Routes to Quantum Molecular Dynamics, CECAM, Switzerland

Implementation of Exact and Approximate Methods for Nonadiabatic Molecular Quantum Dynamics Induced by the Interaction with the Electromagnetic Field	2014
--	------

Fall Meeting of the Swiss Chemical Society, ETHZ, Switzerland

Skills

<i>Languages</i>	French (mother tongue), English (C1)
<i>Softwares</i>	L ^A T _E X, MATHEMATICA, Microsoft office
<i>Programming languages</i>	FORTRAN, PYTHON, BASH

Interests

SPORTS (trail running, cross-country skiing, nordic skiing, mountain biking, snowboarding)

MUSIC

TRAVELLING

FOREIGN CULTURES

